Insight to the Liquid-Vapor Phase-Change Processes Using Molecular Dynamics Method

By

Jinhuan Pu

submitted to Queen Mary University of London

in partial fulfillment of the requirements for the Degree of

Doctor of Philosophy

in the

School of Engineering and Materials Science

2021

Declaration

I, Jinhuan Pu, confirm that the research included within this thesis is my own work or that where it has been carried out in collaboration with, or supported by others, that this is duly acknowledged below, and my contribution indicated. Previously published material is also acknowledged below.

I attest that I have exercised reasonable care to ensure that the work is original and does not to the best of my knowledge break any UK law, infringe any third-party copyright or other Intellectual Property Right, or contain any confidential material.

I accept that the College has the right to use plagiarism detection software to check the electronic version of the thesis.

I confirm that this thesis has not been previously submitted for the award of a degree by this or any other university.

Signature: Jinhuan Pu

Date: 26/08/2021

Acknowledgements

I would like to first thank my supervisor, Prof. Huasheng Wang, for his patience, continuous encouragement, persistent support, and insightful suggestions during my journey of PhD. His enthusiasm and rigor for research inspire me a lot. I still remember the time we discuss together and revise my papers word for word in his office. Besides my research, he also cares about my future. He always tries his best to provide me good opportunities and sincerest suggestions.

I take this opportunity to sincerely thank Prof. Wen Wang for his encouragement and discussions about my research. He is a good role model for my career and his responsibility, wisdom and patience inspire me. I want to give my thanks to Prof. John W. Rose. His enthusiasm for research deeply influences me. I also want to express my thanks to Dr. Hasan Shaheed and Prof. Xi Jiang for their supports. I would also like to give my appreciation to the lab technicians in SEMS for their constant support in assembling the experiment rig for me.

I greatly appreciate to Prof. Jie Sun at Xi'an Jiaotong University for his patient guidance and continuous encouragement. Every time I have a meeting with him, I obtain a lot of motivation and when I feel unconfident and bewildered, he always gives me tremendous support and suggestions. I owe my sincere gratitude to Prof. Guihua Tang at Xi'an Jiaotong University, who was my supervisor when I studied for my master. He provided the opportunity for me to enter the world of scientific research. He always gives me the sincerest and crucial suggestions about my career and research.

I am also thankful for my friends and colleagues' supports during these years. Life is up and down but you always accompany me and bring happiness into my life. Particularly, I would

like to thank my best friend in London, Sara. We both have experienced the tough times since the Covid-19, but the good thing is we have each other's accompany. We always say the positive thing about Covid-19 is that it makes us become best friend. I wish my friends and colleagues all the best in their future.

Finally, I want to express my appreciation to my family. They always give me unconditional support no matter what decision I have made and the only thing they care about me is if I am happy. Their love encourages me to live through the difficulties in my life. I gratefully dedicate this thesis to them.

Abstract

In this thesis, condensation process has been first addressed. The dependences of formation and transition of condensation mode on surface wettability (β) and temperature difference (ΔT) is explored. Five formation mechanisms and two transition mechanisms are revealed. Meanwhile, the dependence of nano-confined surface condensation on tangentially external force field (f_e) is considered. The dynamic behaviours of nano-confined surface condensation are analysed. The heat transfer analysis shows that f_e indirectly influences the interfacial thermal resistance by direct influence on condensation. Results also show that as f_e increases or β decreases, the dissipated heats increase and gradually take over the total transferred heat, which finally reduces or suppresses the occurrence of condensation. Furthermore, the growth and self-jumping of single droplet on the nanostructured surfaces are systematically investigated. The MD simulation has proved the effectiveness of self-jumping of single-nanodroplet driven by Laplace pressure. The results show that increasing the surface wettability and size of the pinning site promotes the droplet growth but blocks the droplet self-jumping.

Secondly, this thesis has focused on the liquid-to-vapor process. How to maintain and enhance nanofilm evaporation on nanopillar surfaces are systematically investigated. The results show that the smaller pitch between nanopillars and larger diameter of nanopillars can enhance evaporation but also raise the possibility of boiling, whereas the smaller height of nanopillars can enhance evaporation and suppress boiling. The nanofilm thickness should be maintained beyond a threshold to avoid the suppression effect of disjoining pressure on evaporation. Additionally, the generation and evolution of nanobubbles on nanoparticles (GNPs) are studied. The results demonstrates that the superhydrophobic GNP is favourable

for fast and energy-saving nanobubble generation. Increasing heating intensity (Q) can promote the generation and growth of nanobubbles for a given β. The maximum radius of the nanobubble is found to be dependent on β and not Q.

List of Figures

List of Tables

Nomenclature

a	acceleration
A	area
a	lattice constant
A_i	size of hydrophilic pinning site
B	dispersion constant
D	diameter
E	accumulative energy transferred
E_K	macroscopic kinetic energy
E_Q	heat transferred from the fluid to the wall
f	random force
F	Fletcher factor
f_e	external force
F_i	force acting on particle
H	depth/height
l	length of simulation box
L_max	widest length of the droplet in the y-z plane
m	mass
$\dot{m}''$	evaporation mass flux
N	number of condensed molecules
N_ad	number of adsorbed molecules
n_c	number of surface clusters
n_max	maximum size cluster
P	pressure

P	pitch between the pillars
P_c	capillary pressure
P_d	disjoining pressure
Q	heat transfer rate
Q_c	latent and sensible heats originated from the cooling and condensation, or pure cooling, of the fluid
Q_f	dissipated heat generated due to the existence of the external force field
r	coordinate
R	radius
R	radius
r_c	cut-off distance
R_{th}	interfacial thermal resistance
t	time
T	temperature
T_m	melting point
U	internal energy
v	velocity
W	work done by external force
W	width
z_c	droplet centroid in the z direction
ΔG^*	free energy barrier
ΔT	temperature difference

Greek symbols

α	isothermal compressibility

β_t	surface wettability of the pinning site
β	coefficeint for surface free energy
γ	frictional coefficient
γ_{lv}	liquid-vapor surface tension
δ	nanofilm thickness
$\delta\tau$	time step
Δ	difference
$\Delta\mu$	chemical potential difference
ε	energy characteristic parameter
η	energy conversion efficiency
θ	contact angle
λ	scaling factor for velocity
ρ	density
σ	length characteristic parameter
τ_T	coupling parameter for Berendsen thermostat
φ	potential function

Acronyms

CFD	computational fluid dynamics
CN	coordination number
CNT	classical nucleation theory
DWC	dropwise condensation
DWC^n	dropwise condensation case resulting from nucleation
DWC^r	dropwise condensation case resulting from film rupture

EAM	embedded-atom method
FCC	face-centered cubic
FWC	filmwise condensation
FWC^a	filmwise condensation case resulting from adsorption-induced film
FWC^n	filmwise condensation case resulting from nucleation
GNP	gold-like nanoparticle
HVAC	heating, ventilating, and air conditioning
LAMMPS	large-scale atomic/molecular massively parallel simulator
LISs	lubricant-infused surfaces
L-J	Lennard Jones
LSPR	localized surface plasmon resonance
MD	molecular dynamics
NC	no-condensation
OVITO	Open Visualization Tool
RDs	relative deviations
SPR	surface plasmon resonance

Contents

1 Introduction

1.1 Background

Due to the utilization of latent heat instead of only sensible heat during phase-change processes (condensation, evaporation and boiling), phase-change heat transfer shows significant advance for the energy systems and extensively exist among them. In practical situations, the performance and costs of heating, ventilating, and air conditioning (HVAC) systems, which take up to about 20% of the total energy consumption in developed countries [1], are affected by the process of liquid-vapor phase change. In the worldwide, 85% of power generation plants and 50% of desalination plants are based on steam condensers [2]. With the growing demand in dissipating high heat flux in many devices, such as electronic chip with excess of 10 MW/m^2 local heat flux, the development of thermal management systems has shifted focus from single-phase liquid cooling schemes to phase-change cooling schemes [3]. To address tremendous challenges in energy sustainability, increasing efforts have been made on solar-thermal technology as the energy of solar radiation on the earth surface in 1 hour is higher than the global energy consumption in one year [4]. Solar evaporation has been considered as one of the most promising implementations of solar-thermal technology [5]. To enhance and control phase-change processes and satisfy the efficiency, performance, safety and reliability requirements for these energy systems, their fundamental understanding is of significant importance.

Additionally, owing to the recent advancements in nanoscale surface-coating and nanomachining technologies, liquid-vapor phase change at nanoscale has drawn increasing interest in the applications of energy systems. However, due to the limitation of the observation and measurement technique, it is challengeable to carry out experimental studies

at nanoscale. Molecular dynamics (MD) method, known with the deterministic and microscopic nature, provides an extremely valuable tool to elucidate the phenomena from molecular level and provide a fundamental understanding not accessible by experiments or CFD simulations. Thus, MD method is used in this thesis. Before proceeding to the specific works and contribution of this thesis, current understanding about phase-change processes is reviewed.

1.2 Surface wettability

Surface wettability plays important role in the phase-change performance and it can be characterized by the equilibrium contact angle (θ) of a liquid droplet deposited on the test surface [6], as shown in Figure 1.1. When the contact angle is smaller than 90°, the solid surface is considered as a hydrophilic surface. Superhydrophilic surface arises when the contact angle is less than 10°. By contrast, the hydrophobic surface has a contact angle larger than 90° and as the contact angle exceeds 150°, the surface is regarded as superhydrophobic surface. The surface wettability is commonly tailored by changing surface chemistry and structure. Decreasing the surface energy can increase the contact angle and decrease the surface wettability. The micro/nanostructures fabricated on hydrophobic surfaces can further increase the contact angle.

.

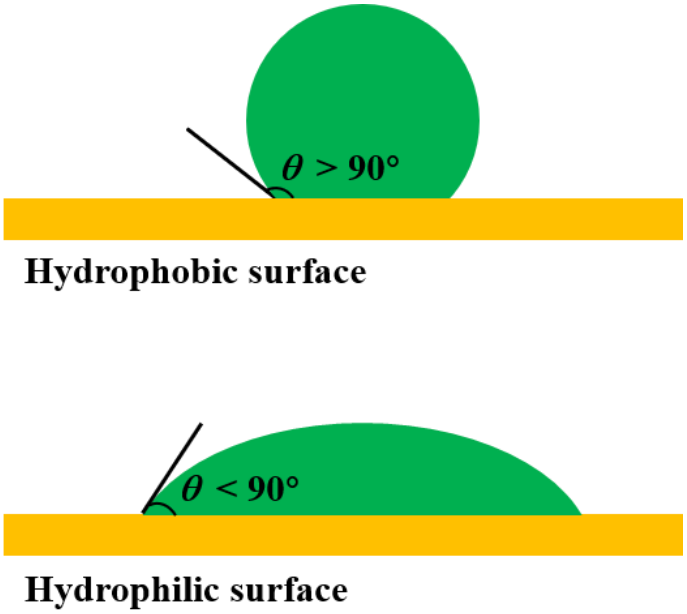

Figure 1.1: The schematics of different surface wettabilities. θ is the contact angle of droplet.

1.3 Surface condensation

Condensation is a phase-change process in which vapor changes to liquid and can be initiated by either cooling vapor to make its temperature below the saturation temperature or making the vapor pressure exceed its saturation pressure. When condensation occurs on the solid surface, it is called surface condensation. The surface condensation mode is conventionally categorized as either dropwise condensation (DWC) or filmwise condensation (FWC), as shown in Figure 1.2.

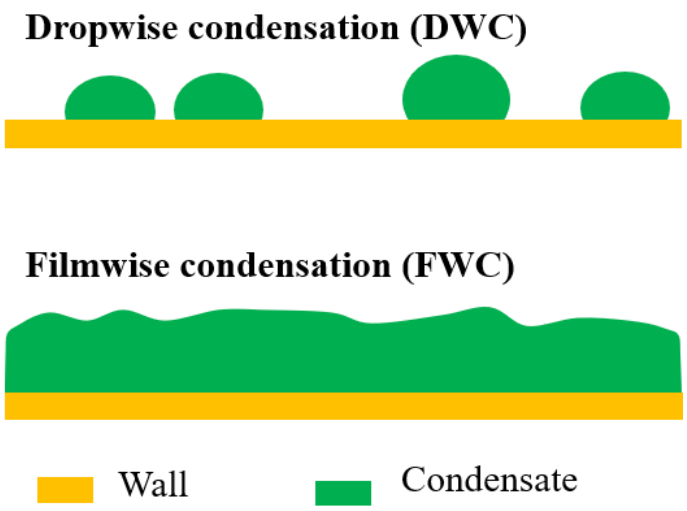

Figure 1.2: Schematics of dropwise and filmwise condensations.

Currently, condensers in energy systems commonly operate in the filmwise condensation mode. In the filmwise condensation mode, the condensate forms a continuous layer of liquid and fully covers on the condensing surface after the vapor condenses on the solid surface. Afterwards, the condensation process occurs at the liquid-vapor interface and the released heat by condensation must pass through the liquid film [7]. The formation of the liquid film generates a significant thermal resistance for the heat transfer process and deteriorates the heat transfer performance. The thicker the film develops, the higher the thermal resistance exists, and the worse the performance of heat transfer becomes. Some efforts have been paid to improve filmwise condensation heat transfer, in which developing novel surface features is the main efficient method. The fin geometry is found to be an efficient enhanced structure therefore different fins, such as integral fins [8][9], there-dimensional fins [10], and porous fins [11] et al., have been developed [12].

Dropwise condensation (DWC) was first discovered by Schmidt et al. in 1930 [13] and since then it has been given significant attention as its heat transfer coefficient is found to be an order of magnitude higher than that of filmwise condensation [14]. To achieve sustained

dropwise condensation, great efforts focus on surface modification [2], e.g. tailoring surface chemistry and energy [15]-[20] and changing surface geometry [21]-[27].

To produce dropwise condensation, hydrophobic and superhydrophobic surfaces are preferred. However, commonly used surfaces for condensation, such as aluminum (Al), copper (Cu), and stainless surfaces, are hydrophilic and easily appear filmwise condensation (FWC). Thus, different types of surface coatings, such as noble metals, rare earth oxides, surface alloys, polymer, have been used to function or promote the hydrophilic surfaces with a layer of low surface energy hydrophobic molecules to produce dropwise condensation (DWC) [2]. The copper substrate with silver coatings thicker than 150 nm were reported to achieve DWC by O'Neill et al. [28]. A maximum DWC sustaining time of 2400 h and a max enhancement of 550% in heat transfer coefficient were documented. A cerium-oxide (CeO) coating on Cu, Al, and steel with thickness less than 200 nm was developed by Shim et al. [29] and superhydrophobic surfaces with contact angle hysteresis less than 5° were obtained to achieve active dropwise condensation (DWC). The surfaces with the CeO coating can provide 5 times higher heat transfer coefficient compared with the silane-treated surfaces. Zhao et al. [30] have coated the Cu substrate with four kinds of surface alloys (Cu-Ar, Cu-N, Cu-He, and Cu-H) by using ion-implantation technology and steady dropwise condensation (DWC) was observed on the four coated surfaces. Their coating technology was found to provide 3 times higher of heat transfer coefficient compared with noble metals coating.

Superhydrophobic surfaces combing micro- or nanostructures or both have been proposed for enhancing and/or stabilizing dropwise condensation (DWC). Compared with plain hydrophobic surfaces, micro/nanostructured superhydrophobic surfaces can promote spontaneous droplet motion and removal [23]. Various micro/nanostructures (nanograss [31], nanowires [32][33], pillars of square and circular [34][35], nanoparticle self-assembly [36], triangular spikes [37], carbon nanotube forests [38] et al.) have been developed to control

droplet behaviours for enhancing heat transfer performance. The nanowired hydrophobic copper surface developed by Wen et al. [33] was reported to produce dropwise condensation with a 100% higher overall heat flux compared with that on the advanced hydrophobic surface. Inspired by the hard-shell-like structures of beetles, Hou et al. [39] proposed a hybrid surface, where the hydrophobic micropillars coat with hydrophilic top and are surrounded by superhydrophobic nanograss. The novel structured surface demonstrated higher density nucleation and droplet depinning characteristics. Compared with the conventional dropwise condensation on the flat hydrophobic silicon surface, a 63% enhancement of heat transfer coefficient was obtained on the hybrid structured surface. By mimicking lotus leaves, a two-tier texture with short carbon nanotubes deposited on micromachined pillars was manufactured by Chen et al. [40]. Continuous dropwise condensation was obtained on such micro/nanostructured surfaces and the structured surfaces even demonstrated superior ability in retaining superhydrophobicity during and after laboratory condensation.

Molecular dynamics (MD) simulation has been widely used to investigate the insights into the phenomena of fluid flow and heat transfer in nanoscale [41]-[46]. Attentions in MD simulations of surface condensation have been mainly paid to surface characteristics,[47][48] computational strategies,[49][50] formation free energy,[51] nanostructure,[25][52] cluster analysis,[53] external force field[54]-[56] and so on. In earlier studies,[57][58] the features during the onset, early and developed stages of surface condensation have been demonstrated. In the case of condensation in a slit pore, the rate of nucleation is higher than that in the homogenous vapor at the same vapor density and temperature, irrespective of the strength of attraction between the wall and vapor molecules [59]. The nucleation is more likely to initiate on the high energy particles that embedded in a low energy surface and clusters do not migrate around their original positions [60]. It has also been found that there

are two different types of formation of nanoscale droplet depending on the relative surface free energy, i.e., the formations with and without film-like condensate, which enriches the 'classical hypotheses' of the onset of dropwise condensation [57]. For the formation with film-like condensate case, a film-like condensate is formed firstly when the surface with relatively large wettability is cooled, then it contracts and ruptures into several nuclei and finally evolves into a large droplet. During condensation there exists a competition between the interfacial thermal resistance and condensate bulk thermal resistance [58]. At the onset of condensation, the interfacial thermal resistance takes over, while the condensate bulk thermal resistance gradually dominates with condensate thickness growing.

Despite the wide range of possibilities for dropwise condensation (DWC) enhancement provided by surface modification technologies (eg. micro/nanoscale fabrication, surface coatings), the industrial implementation of sustained dropwise condensation (DWC) remains challengeable as the durability and scalability of these modified surfaces cannot be guaranteed, which calls for further understanding in surface condensation. Additionally, at high subcooling temperatures or supersaturation pressures, the adhesion effect of droplets can overcome the surface tension effect and the droplets formation is faster than droplets removal, which results in flooding condensation and the transition of condensation mode from dropwise to filmwise. Thus, further investigation on how to avoid flooding condensation is imperative.

1.4 Droplet departure

Dropwise condensation (DWC) cycle starts from the nucleation of droplets, followed by droplets growth by either direct condensation or coalescence, and finally periodic departure from the surface. The droplet departure permits new nucleation sites on the surface and guarantees sustained dropwise condensation (DWC). In this cycle, droplet departure from

the surface has drawn much attention because it is vital to avoid surface flooding and to maintain efficient DWC [61]-[63]. In most condensing surfaces, droplet departure is commonly driven by gravitational force, which needs to overcome the contact line pinning force. Many efforts are paid to reduce the contact line pinning force and accelerate droplet departure, wherein lubricant-infused surfaces (LISs) have shown competitive advantages for both high- and low-surface-tension liquids [64]. Anand et al. [65] experimentally observed the remarkable mobility and the resultant sweeping effect of condensed drops on LISs and the moving speed of condensed droplets with size of 100 μm are several orders of magnitude higher than those on identically structured superhydrophobic surfaces. Smith et al. [66] showed that droplets on LISs have up to three different three-phase contact lines, which results in 12 different thermodynamic states. Guo et al. [67] revealed that the surface dynamic wettability of droplets on LISs during condensation process is dissimilar to their static wettability and the consistency between them is identified in their work. Ho et al. [68] studied the condensation of low surface tension fluids on LISs and developed a new model to predict the heat transfer coefficient with maximum deviation of 15% compared with experimental results. However, the performance of these surfaces highly depends on the existence of the lubricant and currently its depletion is inevitable, which will eventually cause LISs to lose their advantages.

Additionally, coalescence-induced droplet jumping is regarded as one of the efficient passive methods for achieving droplet departure, and lots of investigations have been carried out on its mechanistic understanding and application [69]-[79]. Boreyko et al. [69] first discovered the spontaneous droplet removal resulting from the coalescence-induced droplet jumping and reported a surprising jumping velocity at a speed as high as 1 m/s. Miljkovic et al. [70] experimentally demonstrated highly efficient jumping-droplet condensation heat transfer on silanized copper oxide surfaces with a 25% higher overall heat flux and 30% heat transfer

coefficient compared with conventional dropwise condensation (DWC) on cooper surfaces at low supersaturations. Liang et al. [72] first demonstrated that the coalescence-induced jumping can also happen for nanoscale droplets although there is large internal viscous dissipation using molecular dynamics method. Yan et al. [75] developed a visualization technique to systematically study the effects of droplet size, surface structure, pinning, and liquid property on coalescence-induced droplet jumping. Shi et al. [78] first used lattice Boltzmann method to study the whole process of jumping-droplet condensation from nucleation to departure and also took the large amount of noncondensable gas into account. They found that the diameter and maximum jumping height of coalesced droplet decrease with the increase of noncondensable gas fraction. Recently, Zhu et al. [79] developed a biphilic nanostructured surface to effectively improve the height of coalesced droplet jumping. Their results show a ~28% improvement of droplet jumping height on this surface compared with that on a superhydrophobic surface under atmospheric conditions. Additionally, they discovered that the droplet contact electrification on biphilic surfaces can achieve droplet jumping height ~137% higher than that under atmospheric conditions. However, limited by coalescence hydrodynamics, the energy conversion efficiency (η) for the coalescence-induced droplet jumping process was experimentally and numerically reported to be less than 6%, corresponding to a dimensionless jumping velocity of 0.2-0.3 [80][81]. Meanwhile, previous studies show that the jumping velocity (v_j) of a coalescing droplet decreases with the droplet size increasing ($v_j \sim R_j^{-0.5}$) [69], which leads to larger droplets jumping, induced by coalescence, difficult. Additionally, this jumping process needs at least two droplets but for size-mismatched droplets, the jumping of coalescing droplet may fail due to the marginal kinetic energy [75].

In recent years, with the fast development of surface-nanomachining and surface-coating technologies, surface-structured-induced Laplace pressure difference stored within the

droplet has been shown to trigger droplet departure or dewetting transition efficiently [82]-[87]. Lv et al. [82] reported an in situ spontaneous dewetting transition of condensed droplets on rigid superhydrophobic pillared surfaces with two-tier roughness driven by the Laplace pressure difference. They also developed a theoretical expression to predict the Laplace pressure of the droplet and a model to characterize the critical size of the droplet when transition happens. Aili et al. [83] manufactured superhydrophobic nanostructured microporous surfaces to manipulate the droplet growth and jumping. They observed forced self-jumping of stretched droplets in pores and revealed that the excess surface free energy stored in the stretched droplet surface benefits this jumping. Sharma et al. [84] shows that the condensed droplets can spontaneously eject from even irregular, re-entrant, and random macrotextures driven by the Laplace pressure difference. Recently, Yan et al. [87] demonstrated that the jumping of a single-droplet driven by the Laplace-pressure contrast within the droplet is a much efficient passive method for droplet departure and it can achieve an ultra-high η up to 50-60%, with a dimensionless jumping velocity of 0.95.

1.5 Capillary-fed evaporation device

Due to utilizing high latent heat of vaporization, evaporation has received particular interest in the last few decades [88]-[96], e.g., cooling electronics and photonics devices [97][98] and solar vapor generation [99]. Particularly, capillary-fed, thin-film evaporation device using wicks has drawn increasing attention because of its passively fluid replenishment ability and efficient heat transfer performance. In these evaporators, a porous wick structure is used to generate a capillary pressure to drive the liquid flow from a liquid reservoir as it evaporates. Different wick structures have been investigated, e.g. pyramidal, conical, cylindrical pillars and sintered particle wick [100]. Figure 1.3 shows a schematic of a capillary-fed evaporator using cylindrical pillars.

Many efforts have been driven to understand the governing physics and improve device performance [101]-[112]. Ravi et al. [102] fabricated different micropillar array wicks to assess the accuracy of various existing models for permeability and capillary pressure. An overall model for predicting the liquid mass flow rate was developed by combining two most accurate models. Adera et al. [104] carried out systematic experiments to characterize the capillary-fed thin-film evaporation from micropillar wicks and developed a semi-analytical model to determine the capillary-limited dry-out heat flux and wall temperature with ±20% accuracy. Antao et al. [107] used a transient laser interferometry technique to investigate the evolution of the liquid meniscus in micropillar arrays during evaporation. They found that there are two stages during the dynamics evaporation and the receding contact angle is independent of the structure geometry and the rate of evaporation. Zhang et al. [111] used a custom micro-Raman spectroscopy platform to achieve the measurement of local thin film temperature and mapping the overall temperature distribution on the microstructure surface at different heat fluxes.

In prior studies, the dynamics of liquid meniscus has not been accurately measured due to the technique limitation, especially the evolution of the liquid meniscus near nanopillars. Additionally, most investigation had been carried out directly based on pure evaporation like above mentioned. Although some works [113]-[115] observed the existence of boiling in those capillary-fed evaporators, the onset and evolution of nanobubbles in the wicks and how to avoid boiling have not been clearly characterized. To design a reliable capillary-fed evaporator, pure evaporation in the absence of boiling is preferred due to its stable nature compared with the chaotic boiling process and the boiling limit [93]. So, the understanding how to maintain stable evaporation is necessary. As we know the film thickness from cell to cell in capillary-fed evaporator is different due to the pressure gradient across the substrate [100][112], but the effect of film thickness on evaporation in nanopillars remains limited in

previous numerical and experimental studies and its role in the maintenance and enhancement of evaporation needs more investigation.

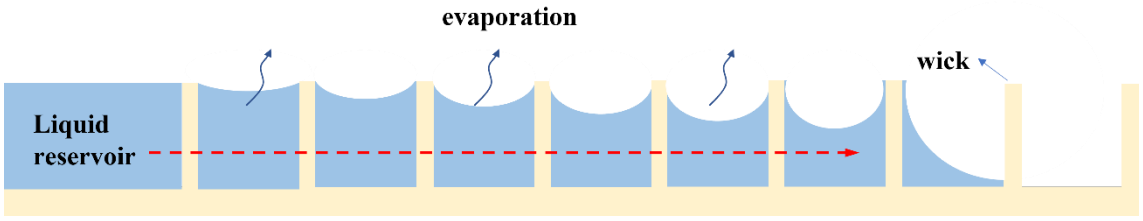

Figure 1.3: Schematic of a capillary-fed evaporator using cylindrical pillars [100].

1.6 Plasmonic nanobubbles

Some noble metal nanoparticles, such as Au, Ag and Pt, have shown tremendous promise for science and technology applications, such as biomedical diagnosis,[116],[117] photothermal therapy,[118]-[120] solar energy conversion [121]-[126] and locally enhanced chemical reactions [127],[128] due to its unique optical properties arising from localized surface plasmon resonance (LSPR). In these applications, the nanobubble generated around heated nanoparticles is referred to as plasmonic nanobubble and the dynamics of nanobubble formation and evolution is of crucial importance for energy utilization or even human health.[122],[125] For example, when nanoparticles are immersed in water, steam could be generated by directly irradiated sunlight without heating the whole volume of the fluid. This remarkably increases the solar-to-heat efficiency up to 80% and hence significantly broadens the solar energy harvesting.[123] When nanoparticles, selectively attached to the membrane of tumour cells, are exposed to the high-power laser, nanobubbles generated could mechanically destroy the cell membrane and lead to damage of tumour cells.[129] To advance and open up applications of nanoparticles, a fundamental understanding of the nanobubble dynamics around heated nanoparticles plays a core role. Many experimental

studies [130]-[135] have attempted to characterize the thermodynamic and kinetic aspects of nanobubble generation around heated nanoparticles. However, due to nanometric size, experimental study is limited for visualizing and measuring the diameter and time evolution of nanobubbles.

Molecular dynamics (MD) simulation, known as a state-of-the-art numerical method for the simulation of nanoscale process, provides an ideal resort in understanding the inception and dynamics of nanobubbles around nanoparticles from the molecular-level insights. Merabia et al.[136] first obtained a vapor nanobubble around a heated nanoparticle using MD simulation, and they observed a critical heat flux around strongly heated nanoparticles followed by development of a vapor layer and heat flux drop. Sasikumar et al.[137]studied the role of the nanoparticle curvature on the liquid phase stability. They found that phase change could just be observed above the critical size. They also investigated the nanoscale cavitation dynamics under non-continuous heating.[138] Recently, the effect of dissolved gas in the formation and growth dynamics of a nanobubble around a heated nanoparticle was considered by Maheshwar et al. [139].

1.7 Objectives of the thesis

The aim of this thesis is to carry out fundamental understanding about liquid-vapor phase-change process (condensation, evaporation, and boiling) using molecular dynamics simulation and help further enhance and control the phase-change process. The aim of the thesis can be achieved by the following objectives:

1) Reveal the mechanism of formation and transition of surface condensation mode from molecular insights and simultaneously understand how the temperature difference and surface wettability affect the transition mode. (Chapter 3)

2) Understand the dependence of nano-confined surface condensation on tangentially external force field and reveal the energy conversion mechanism during different condensation/cooling situations. (Chapter 4)

3) Prove the effectiveness of single nanodroplet self-jumping driven by the Laplace pressure difference; reveal the growth and jumping characteristics of single condensed nanodroplet on nanostructured surfaces. (Chapter 5)

4) Investigate how to maintain and enhance nanofilm evaporation on nanopillar surfaces considering from both geometry structure and nanofilm thickness aspects. (Chapter 6)

5) Reveal the generation and evolution dynamics of nanobubbles on heated nanoparticles and consider the effects of surface wettability and heating intensity of the nanoparticles; present the heating-up characteristics of nanoparticles during these processes. (Chapter 7)

1.8 Organization of the thesis

This thesis consists of eight chapters. In Chapter 1, the background of this thesis is presented and the previous efforts to understand and control liquid-vapor phase-change process are reviewed. In Chapter 2, a detailed introduction about molecular dynamics method is given. In Chapter 3, the dependences of formation and transition of surface condensation mode on surface wettability and temperature difference are investigated. A schematic overview of all the mechanisms is presented. In Chapter 4, the dependence of nano-confined surface condensation on tangentially external force field is elucidated. The energy balance analysis during condensation process is carried out. In Chapter 5, the growth and self-jumping dynamics of single condensed droplet on nanostructured surfaces are focused. The effect of the feature of the pinning site is investigated. In Chapter 6, how to maintain and enhance nanofilm evaporation on nanopillar surfaces is systematically investigated. The effects of geometry and nanofilm thickness are revealed. In Chapter 7, the generation and evolution of

nanobubbles on heated nanoparticles are studied in detail. The investigation about effects of surface wettability and heating intensity of the nanoparticles are conducted. In Chapter 8, the findings of this thesis are summarized and suggestions for the future work are provided.

2 Molecular Dynamics Method

2.1 Introduction

Since Alder and Wainwright successfully achieved molecular dynamics simulation in 1957 [140], molecular dynamics (MD) method has been developed to a powerful tool to reveal microscopic mechanism of different physical and chemical phenomenon and overcome the length and time limitation of experiment. MD method is a computational technique based on classical mechanics and statistical mechanics and can connect microscopic information of a system with its macroscopic properties. The basic idea of MD is to determine the trajectory of each particle (atom or molecule) for an interacting many-particle system by solving Newton's equations of motions then extract the interested properties of the system by statistical mechanics methods.

For a system consisting of N particles, given the initial positions and momenta of all particles, the trajectory of particle i (velocity and position) at time t is determined by the following equations of motions based on Newton's second law,

$$F_i(t) = m_i a_i \tag{2-1}$$

$$\frac{\mathrm{d}^2}{\mathrm{d}t^2} r_i = \frac{\mathrm{d}v_i}{\mathrm{d}t} = a_i \tag{2-2}$$

$$v_i = v_i^0 + a_i t \tag{2-3}$$

$$r_i = r_0 + v_i^0 t + \frac{1}{2} a_i t \tag{2-4}$$

where F_i is the force acting on particle i; m_i, a_i, r_i, and v_i are the mass, acceleration, coordinate, velocity of particle i, respectively; the superscript 0 represents the initial state of particle i. To integrate the motions of equations, a lot of integration algorithms have been

developed, such as the Leap-Frog method, Velocity-Verlet method, Euler method, and Predictor-Corrector method.

The F_i can be derived from the gradient of the potential function φ_i contributed from every other particle in the system,

$$F_i(t) = -\nabla \varphi_i \tag{2-5}$$

Thus, besides giving the initial positions and momenta of all particles, determining a realistic force field describing the interparticle interaction in the system is arguably essential for a successful MD simulation.

Based on the above brief introduction, a schematic of main steps involved in MD simulation is depicted in Figure 2.1. In this thesis, all the MD simulations are conducted in open-source software LAMMPS (large-scale atomic/molecular massively parallel simulator) [141]. LAMMPS is a widely used MD code developed by Steve Plimpton in the early 90's at Sandia National Laboratory and continues to be an effective open-source platform for enabling MD simulations. It could model an ensemble of particles in a liquid, solid, or gaseous state and can also model atomic, polymeric, biological and metallic systems using various force fields and boundary conditions. LAMMPS executes by reading commands from an input script. When the input script ends, LAMMPS exits. Each command causes LAMMPS to take some action. It may set an internal variable, read in a file, or run a simulation. The OVITO (Open Visualization Tool) software is employed as the visualization program for displaying snapshots and animations of simulation system. More details about MD method can be found in research papers and popular MD books [142]-[144].

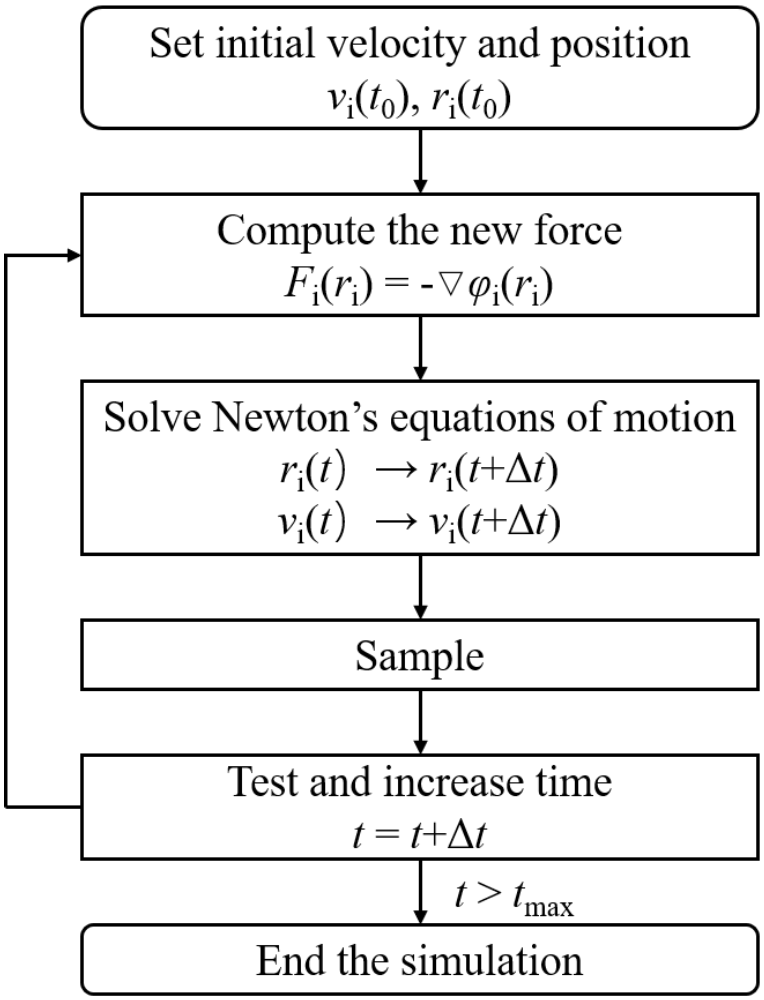

Figure 2.1: Basic flowchart of MD program. *v* and *r* are the velocity and position of particle *i*. *F* and φ represent force and potential function.

2.2 Potential functions

The accuracy of MD simulation is highly determined by the force field used to describe the interactions between the particles in the system. The force field generally comprises the bonded and non-bonded interactions and is written as

$$\varphi_{toal} = \varphi_{bonded} + \varphi_{non-bonded} \tag{2-6}$$

The bonded interactions include bond stretching (b), angle bending (θ), dihedral angle torsion (ϕ), and out of plane torsion (χ), as shown in Figure 2.2(a) and the mathematical form is given as

$$\varphi_{bonded} = \varphi_b + \varphi_\theta + \varphi_\phi + \varphi_\chi \tag{2-7}$$

The non-bonded interactions include Van der Waals interaction (short range force) and Coulomb interaction (long range force), as shown in Figure 2.2(b) and the mathematical form is given as

$$\varphi_{non-bonded} = \varphi_{VdW} + \varphi_{Coulomb} \tag{2-8}$$

In this thesis, the simulation systems consist of molecules with only non-bonded interaction and Lennard Jones (L-J) potential and embedded-atom method (EAM) potential are used to describe the non-bonded interactions.

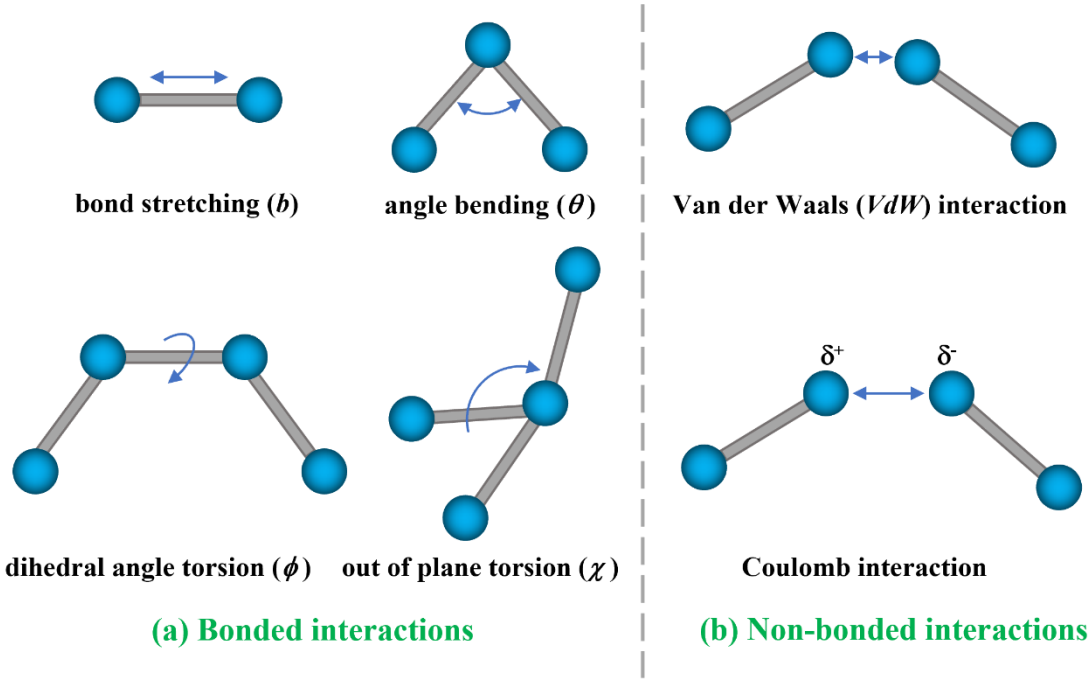

Figure 2.2: Schematics of interatomic interactions in a force field.

2.2.1 Lennard Jones potential

Lennard-Jones (L-J) potential is the most commonly used pairwise potential in MD simulation and was first proposed by Lennard-Jones in 1924 [145]. It is given as

$$\varphi(r) = 4\varepsilon\left[\left(\frac{\sigma}{r}\right)^{12} - \left(\frac{\sigma}{r}\right)^{6}\right] \tag{2-9}$$

Where r is the interparticle separation, ε and σ are the energy and length characteristic parameters, respectively. This equation considers the short-range repulsive behavior ($(1/r)^{12}$) and long-range attractive effect ($-(1/r)^{6}$). The repulsive force dominates at short distance and originates from the Pauli exclusion principle. The attractive force takes over at long distance and comes from dipole-dipole interactions. Figure 2.3 demonstrates this potential distribution as a function of interparticle separation r. It can be seen that ε determines the depth of the well in the potential and the higher it is, the deeper the well will be. σ gives the length at which the potential is zero.

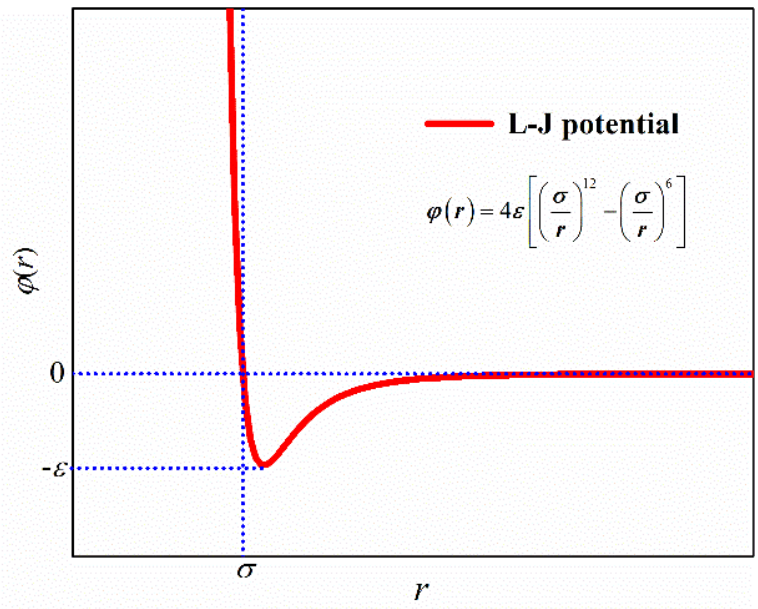

Figure 2.3: Lennard-Jones (L-J) potential: ε and σ are the energy and length characteristic parameters, respectively.

2.2.2 Embedded-atom method potential

To accurately describe non-bonded interactions for metals, the embedded-atom method (EAM) potential is widely used. The EAM potential was initially developed by Daw and Baskes in 1983 [146] and based on density-functional theory. The EAM potential takes into consideration not only simple pair potential, but also the local electron density in the region surrounding the considered atom. The total energy of an atom *i* in a system is written as

$$\varphi_i\left(r_{ij}\right) = E_\alpha\left(\sum_{j\neq i}\rho_\gamma\left(r_{ij}\right)\right) + \frac{1}{2}\sum_{j\neq i}\phi_{\alpha\gamma}\left(r_{ij}\right) \tag{2-10}$$

where E is the embedding energy, and it is the energy to embed atom i into the background electron density. α and γ are the element types of atoms i and j. ρ is the host electron density at atom i due to the remaining atoms of the system; r is the interparticle separation; ϕ is the pair potential interaction.

2.3 Boundary conditions

Due to the limitations of computational power, simulation boxes in MD method generally contain thousands of molecules, which makes it insufficient to accurately estimate the bulk properties of a large macroscopic system. Besides, the severe artefacts will be introduced due to boundary effect when the simulated microscopic system is a simply closed container with finite size. To address these issues, periodic boundary conditions are implemented. Figure 2.4 demonstrates a schematic about periodic boundary conditions in a 2-dimension (2D) system. Due to the employment of periodic boundary conditions in all directions, the original simulation box with N particles (in the center) is replicated infinitely and translated in all directions. All particles in the replicated cell follow the same trajectory as their counterparts in the original simulated box, which minimize the surface effects. In the periodic boundary conditions, when a particle in the simulated box moves out through a boundary face, it will

re-enter the system instantly through the opposite face with same velocity. In the meantime, each particle in the simulated box interacts not only with all other particles in the simulated box but also with the particles in the images, which leads to the dramatical increase in the number of pairwise interactions and tremendous computation cost. To solve this issue, the minimum image convention is used: each particle in the original simulated box only interacts with the closest periodic image of the other particles when calculating the potential energy. It should be noted that the periodic boundary condition does not need to be applied in all directions for some nonperiodic simulation systems, e.g., fluid flow in nanoconfined channel, in which the condition of periodicity seems to be inappropriate in nature. In these situations, in certain directions, fixed boundary condition should be used and meanwhile reflect boundary condition is added to avoid program errors. In the reflect boundary condition, when a particle leaves the boundary on a timestep by a small distance, it will be reflected inside the simulation box by the same distance with identical velocity in the opposite direction.

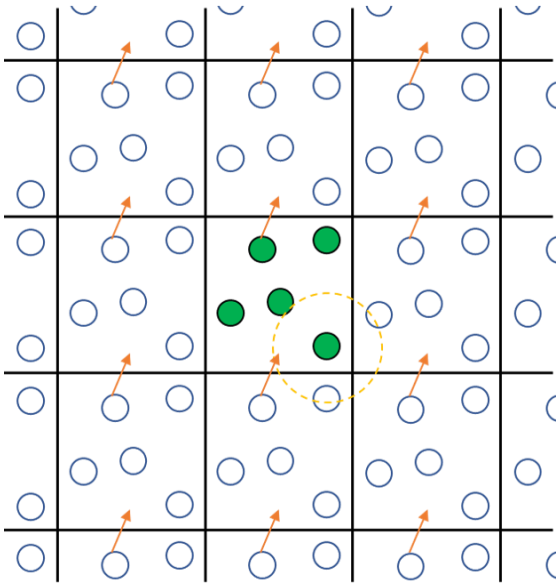

Figure 2.4: 2-dimension (2D) schematic of periodic boundary conditions. The original simulated system is in the center, where particles are marked in green and is surrounded by images. A particle in the given system moves out the simulation box and correspondingly an image particle moves in from opposite site with same velocity.

2.4 Potential truncation

To improve the computational efficiency, a neighbor table along with a distance-based interaction cutoff is used and this method makes the study about significantly large system possible. Using this method, the interactions occurring between two particles beyond the introduced cut-off distance (r_c) are ignored and the potential function is set as zero. To guarantee the consistency with the minimum image convention, the cutoff distance needs to be smaller than half length of the shortest dimension of the simulation box. In this thesis, the r_c for L-J potential adopts the normally used 3.5σ. For EAM potential, r_c is determined by the specific used potential.

2.5 Thermostats

In MD simulation, thermostats are applied to achieve the temperature control and different thermostat has been developed based on either the method of adding additional force term or the method of explicitly scaling the velocity. In this thesis, two of the most popular thermostats, Berendsen and Langevin thermostats, are used to obtain the target temperature.

2.5.1 Berendsen thermostat

Berendsen thermostat was first proposed by Berendsen in 1984 based on the method of scaling the velocity by a certain factor λ [147]. The motivation of Berendsen thermostat is to minimize the local disturbances of a stochastic thermostat when maintaining the global effects unaffected. This thermostat has the advantage that it allows the temperature fluctuations compared with velocity-rescaling thermostat. In Berendsen thermostat, a week coupling between the current system with temperature T and an external heat bath with a target temperature T_0 is applied. The external bath adds or removes heat from the considered system to balance any temperature fluctuations. When using this thermostat, the velocities

are scaled every timestep to achieve the target temperature. Therefore, the rate of change in temperature is proportional to the temperature difference between the given system and external bath and it is written as

$$\frac{dT}{dt} = \frac{T_o - T}{\tau_T} \tag{2-11}$$

where τ_T is the coupling parameter for Berendsen thermostat, and it controls the level of coupled tightness between the given system and external bath. Correspondingly, the scaling factor λ for velocity is given by

$$\lambda^2 = 1 + \frac{\delta t}{\tau_T}\left(\frac{T_o}{T(t-\delta t)} - 1\right) \tag{2-12}$$

where δt is the time step in simulation.

2.5.2 Langevin thermostat

In Langevin thermostat, at each timestep, a frictional force and a random force are added to the system instead of only scaling the fluctuation velocities by a temperature-dependent variable [148]. The friction and stochastic contributions are both considered to correct the current temperature and the equation of motion for particle *i* is modified as

$$a_i = \frac{F_i(r_i)}{m_i} - \gamma v_i + \frac{f_i}{m_i} \tag{2-13}$$

where γ is the frictional coefficient and is the inverse of the characteristic viscous damping time; *f* is the random forces and comes from a Gaussian distribution with an average of zero. There are some advantages for Langevin thermostat in achieving temperature control. First, fewer computations per time step are needed since many atoms are eliminated and included implicitly by stochastic terms. Second, a relatively large time step can be chosen due to dissipative term, because damping term stabilizes the equations of motion. Third, temperature response of a system under Langevin thermostat is fast, and the time costed to

achieve target temperature is usually shorter than that using Nose-Hoover thermostat [149]. However, this thermostat cannot accurately compute the momentum transfer and thus it is not a suitable choice for the simulation about diffusion coefficient et al [150].

2.6 Barostats

In MD simulation, barostats are used to achieve the pressure control and the volume of the system is rescaled to achieve the desired pressure by different barostats. The volume can be adjusted by either isotropic scaling (each direction is scaled equally) or anisotropic scaling (each direction is changed differently). It should be noted that as the pressure in MD is dependent on the virial, which usually varies quickly, there are dramatic fluctuations for pressure. In this thesis, Berendsen barostat is used to acquire the desired pressure.

Analogous to Berendsen thermostat, the simulated system with current pressure P is weekly coupled to an external pressure bath with a fixed target pressure P_o in Berendsen barostat to correct the current pressure. The pressure change rate also varies proportionally with the difference in pressure between the considered system and external bath and is given by

$$\frac{dP}{dt} = \frac{P_o - P}{\tau_P} \tag{2-14}$$

where τ_P is the coupling parameter for Berendsen barostat, and it can be adjusted to change the coupling strength depending on the simulation purpose. The barostat can adjust both the vectors of simulation box and the coordinates of all particles to reach the target pressure. The scaling factor μ for each direction is followed by

$$\mu = 1 - \frac{\alpha \delta t}{\tau_P}\left(P_o - P(t)^{1/3}\right) \tag{2-15}$$

where α is the isothermal compressibility of the given system; δt is the time step in simulation.

3 Formation and Transition of Surface Condensation Mode

The vapor-to-surface temperature difference is the driving force of surface condensation and a key factor affecting this process. However, the effect of vapor-to-surface temperature difference on the onset of formation and transition of surface condensation mode has rarely been taken into account yet. On the other hand, because the condensed liquid keeps contact with the solid surface during surface condensation, wettability also plays a significant role in this process. Therefore, the effects of vapor-to-surface temperature difference and wettability on surface condensation are considered simultaneously in the present chapter. As the continuation and enrichment of earlier studies, this chapter presents a map of surface condensation mode with different surface wettabilities and vapor-to-surface temperature differences based on plenty of MD simulation results. We conduct detailed analyses, from the views of fluid dynamics, heat transfer and thermodynamics, on the formation mechanisms and characteristics of different surface condensation modes, and the transition mechanisms between them.

3.1 Computational methods

In the present work, the surface condensation mode on surfaces with different wettabilities and vapor-to-surface temperature differences is investigated using MD simulation (see Figure 3.1). The simulations are conducted using LAMMPS (large-scale atomic/molecular massively parallel simulator) software package [141]. The overall size of simulation box measures $l_x \times l_y \times l_z$ = 471.12 × 39.26 × 588.9 Å. In the x and y directions, periodic boundary conditions are used, while in the z direction, reflective boundary condition is applied to the uppermost end. The solid wall is constructed by three layers of Pt-like atoms arranged in

face-centered cubic (FCC) lattice and the length of the unit cell is 3.926 Å. Two extra layers of Pt-like atoms are fixed to serve as a frame. The 12-6 L-J potential function is employed for fluid-fluid interaction:

$$\varphi(r) = 4\varepsilon\left[\left(\frac{\sigma}{r}\right)^{12} - \left(\frac{\sigma}{r}\right)^{6}\right] \tag{3-1}$$

where r is the intermolecular separation, ε and σ are the energy and length characteristic parameters, respectively. The potential function is truncated at the cut-off radius $r_c = 3.5\sigma$, beyond which molecular interactions are ignored. $\varepsilon_{Ar\text{-}Ar}$ = 0.01040 eV and $\sigma_{Ar\text{-}Ar}$ = 3.405 Å are used. The interaction among solid atoms is L-J type with $\varepsilon_{Pt\text{-}Pt}$ = 0.521875 eV and $\sigma_{Pt\text{-}Pt}$ = 2.475 Å. The fluid-solid interaction is also governed by Eq. (3-1) but with different energy and length parameters i.e., $\varepsilon_{Ar\text{-}Pt} = \beta\varepsilon_{Ar\text{-}Ar}$ and $\sigma_{Ar\text{-}Pt} = 0.91\sigma_{Ar\text{-}Ar}$, where β is the fluid-solid bonding strength parameter indicating the surface free energy or equivalently the surface wettability. A higher surface free energy corresponds to a stronger surface wettability.

All the simulations are performed in two stages with a time step of 5 fs. In stage 1 (equilibrium stage), the saturated vapor molecules at T_v = 120 K are uniformly arranged. The initial 3 ns guarantees the system to reach the thermal equilibrium state. In stage 2 (condensation/cooling stage), the surface temperature is suddenly reduced to a target temperature and maintained constant afterwards for a period of time. Meanwhile, a vapor supply region is arranged at the uppermost end (thickness is $2l_z/15$), where the temperature and density are maintained at saturation state. For the fluid except for those in the supply region, only NVE ensemble is used. All these temperature control processes are achieved by Berendsen thermostat. In the present work, different surface wettabilities are chosen from super-hydrophobic (β=0.1) to super-hydrophilic (β=0.7). Meanwhile, different vapor-to-surface temperature differences (ΔT) from 5 K to 35 K are considered and the increase in ΔT is achieved by the decrease in surface temperature (T_w) because the initial vapor state is taken to

be the same for all simulation cases. Note that the maximum ΔT is determined by the triple point of argon (T = 84 K).

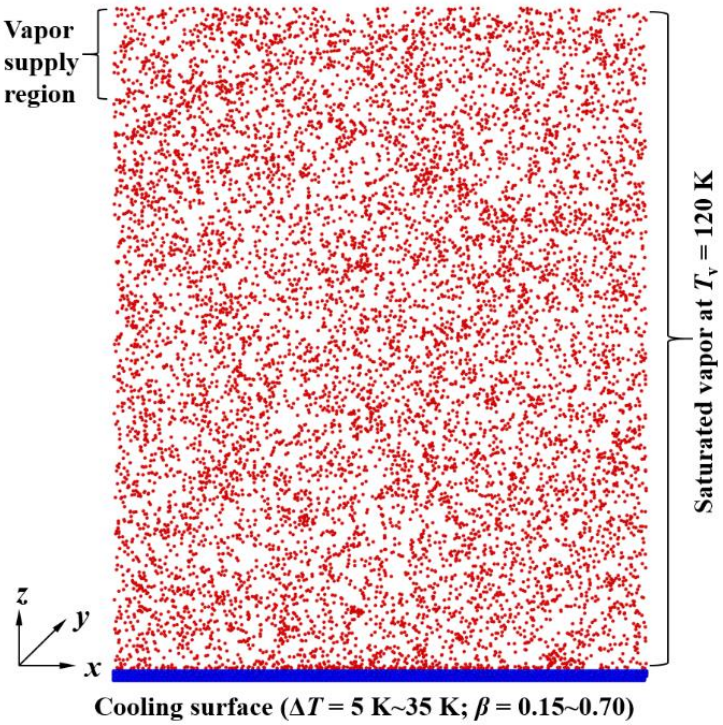

Figure 3.1: Schematic of computational model. Solid atoms are in blue and fluid molecules are in red.

3.2 Results and discussion

3.2.1 Map of surface condensation mode with different β and ΔT

Based on plenty of MD simulation results within 24 ns in stage 2, a map of surface condensation mode with different β and ΔT is shown in Figure 3.2. The red, green and blue squares represent no-condensation (NC), dropwise condensation (DWC) and filmwise condensation (FWC), respectively. It is seen from Figure 3.2 that, for a given ΔT, β significantly affects the formation and transition of surface condensation mode. Generally, for all ΔT, the surface condensation mode transits from NC to DWC and finally to FWC with β increasing. Thus, there are two boundaries among them i.e., NC-DWC boundary and

DWC-FWC boundary. Comparatively, for a given β, the vapor state would not necessarily experience from NC to DWC and finally to FWC with ΔT increasing. When $\beta \leq 0.15$, NC is observed for any ΔT within the maximum ΔT of the simulation. When $0.425 \leq \beta \leq 0.45$ and $\beta \geq 0.525$, the condensation mode does not change with ΔT increasing and they stay DWC and FWC, respectively. When $0.15 < \beta < 0.425$, DWC emerges with increasing ΔT. When $0.45 < \beta < 0.525$, the condensation mode could transit from DWC to FWC. It is readily found that ΔT demonstrates significant effect on the formation of DWC and the boundary between NC and DWC moves to lower β with increasing ΔT. For the transition between DWC and FWC, the effect of ΔT is small and the boundary between DWC and FWC slightly alters towards lower β with ΔT increasing.

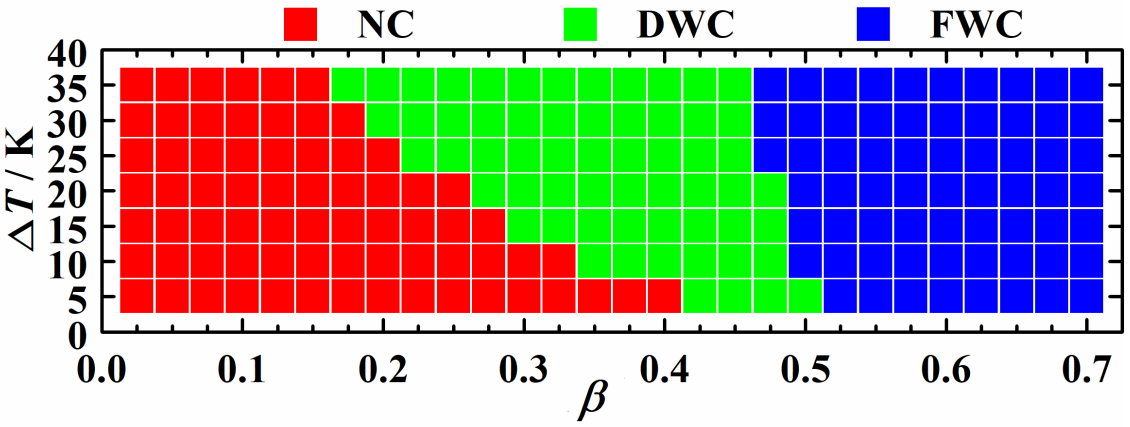

Figure 3.2: Map of different surface condensation modes with β and ΔT. NC, DWC and FWC represent no-condensation in red, dropwise condensation in green and filmwise condensation in blue, respectively.

3.2.2 Dynamic characteristics of surface condensation

1) Formation of different surface condensation modes

To investigate the mechanisms of the formation and transition of different condensation modes on surfaces with different β under different ΔT, four representative values are considered for β (0.275, 0.475, 0.55 and 0.7) and ΔT (5 K, 15 K, 25 K and 35 K),

respectively. Figure 3.3 shows the contour of the total energy (summation of potential and kinetic energies) of fluid molecules for several cases, illustrating typical evolution of surface condensation. Note that to save space the upper part of the fluid region (z > 100 Å) is omitted and the black line at the bottom represents the solid surface. For the NC case shown in Figure 3.3(a), although some fluid molecules near the solid surface are seen to have lower total energy in the late stage, no condensation is observed. In the whole evolution process, except those lower total energy fluid molecules the total energy in the entire fluid region is higher than -0.005 eV.

For the DWC cases, two different formation pathways are observed, as shown in Figure 3.3 (b) and (c). Compared with the NC case (see Fig. 3(a)), when β remains the same (β = 0.275) but ΔT increases from 15 K to 35 K, as shown in Figure 3.3(b), the molecules with lower total energy, apparently seen, randomly appear on the solid surface and the number of those molecules increases with time. During the evolution process, molecules with lower total energy form some small discrete clusters (see definition in 2) in section 3.2.2) firstly, then they gradually grow and coalesce, finally large droplets emerge. When β increases to 0.475 and ΔT = 15 K, as shown in Figure 3.3(c), different evolution is seen during the formation process of DWC. Some molecules with lower total energy are already adsorbed on the surface before the surface is cooled (t = 0 ns) in comparison with the case with β = 0.275 (see Figure 3.3(b)). Similarly, clusters first discretely appear on the solid surface when the solid surface is cooled, but the number and size of clusters increase more quickly, thus most part of the solid surface are occupied by the clusters when t = 2 ns, which indicates a film-like condensation. The vapor molecules continue condensing and the film-like condensation remains for a period of time. Such condensate film characterizes uneven thickness distribution, which potentially leads to contraction and rupture at the locations of thinner film thickness (see marked locations in Figure 3.3(c)). The cap-shaped droplets then

develop and DWC appears from ca. t = 7 ns. It is seen that in DWC initially small surface clusters form randomly on the solid surface and DWC then evolves from either nucleation or film-rupture.

For the FWC cases, two different formation pathways are observed, as shown in Figure 3.3(d)-(f). On the surface with β = 0.475 and ΔT = 35 K, as shown in Figure 3.3(d), initially it is similar to DWC from film-rupture on the surface with β = 0.475 and ΔT = 15 K (see Figure 3.3(c)), where surface clusters form fast and quickly cover the whole surface. It results in the formation of an uneven thickness condensate film. Differently, the film then continues to grow into even thickness film instead of contracting and rupturing. We can see the locations with thinner film gradually disappear and the condensation develops into FWC instead of DWC in Figure 3.3(d). In Figure 3.3(e), due to the increase of β, more molecules with lower total energy appear and are adsorbed on the surface initially. Then, when the surface is cooled, the discrete clusters form and cover the surface quickly. A condensate film forms, indicating FWC. This film is more even than the case with β = 0.475 but it still develops from discrete clusters. Figure 3.3(f) shows another formation pathway. It is seen that the adsorption ability of the surface with β = 0.7 is sufficiently strong and the surface is fully covered by lower total energy molecules before it is cooled. Those molecules have already formed an ultra-thin film on the surface. Therefore, the vapor molecules directly condense onto the existing film and the film grows evenly when the surface is cooled. We can conclude that FWC could originate from either nucleation or adsorption-induced film.

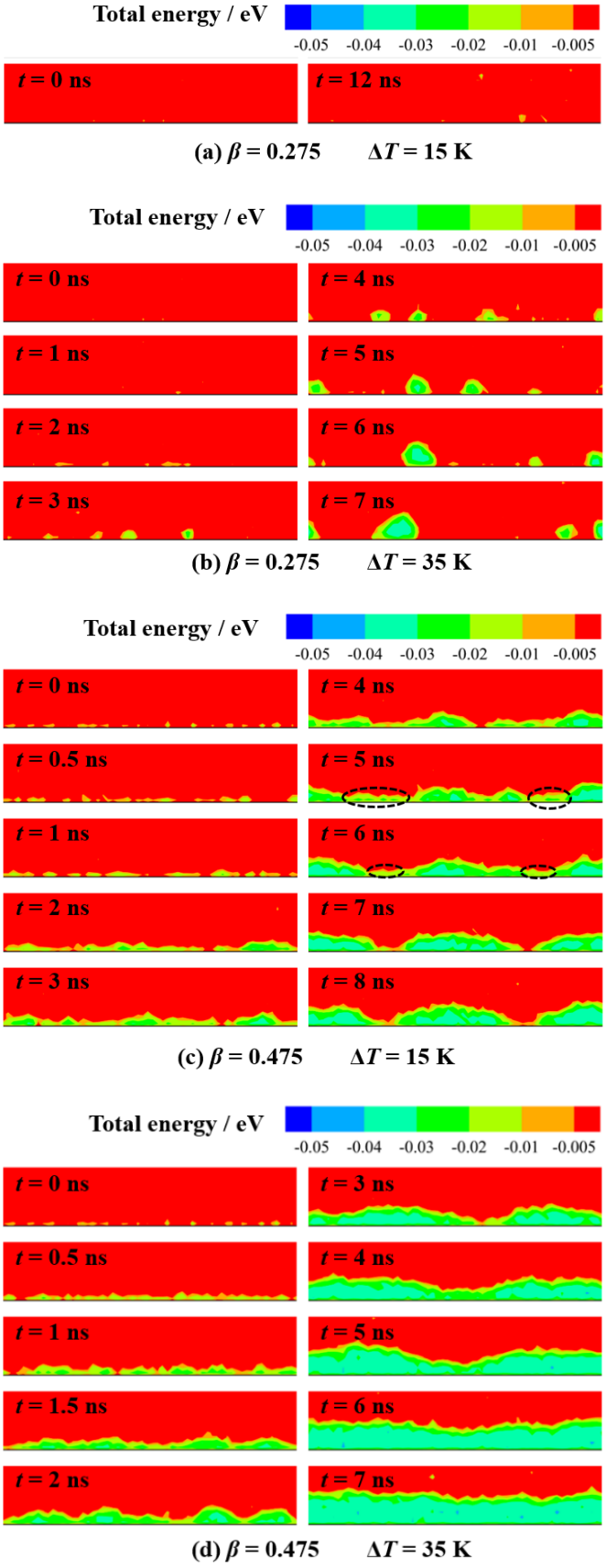
Total energy / eV
-0.05 -0.04 -0.03 -0.02 -0.01 -0.005
t = 0 ns
t = 12 ns
(a) β = 0.275 ΔT = 15 K
Total energy / eV
-0.05 -0.04 -0.03 -0.02 -0.01 -0.005
t = 0 ns
t = 4 ns
t = 1 ns
t = 5 ns
t = 2 ns
t = 6 ns
t = 3 ns
t = 7 ns
(b) β = 0.275 ΔT = 35 K
Total energy / eV
-0.05 -0.04 -0.03 -0.02 -0.01 -0.005
t = 0 ns
t = 4 ns
t = 0.5 ns
t = 5 ns
t = 1 ns
t = 6 ns
t = 2 ns
t = 7 ns
t = 3 ns
t = 8 ns
(c) β = 0.475 ΔT = 15 K
Total energy / eV
-0.05 -0.04 -0.03 -0.02 -0.01 -0.005
t = 0 ns
t = 3 ns
t = 0.5 ns
t = 4 ns
t = 1 ns
t = 5 ns
t = 1.5 ns
t = 6 ns
t = 2 ns
t = 7 ns
(d) β = 0.475 ΔT = 35 K

Figure 3.3

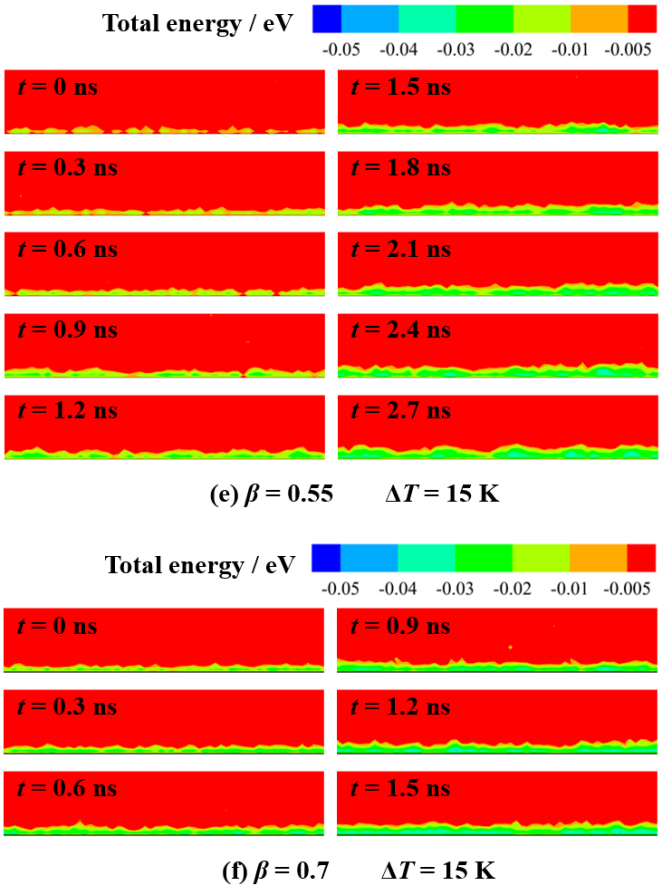

Figure 3.3: Contours of total energy of fluid molecule under different condensation modes.

2) Heat transfer

To quantitatively analyze the heat transfer during surface condensation, the number of molecules in the maximum size cluster (n_{max}) and the number of surface clusters (n_c) are recorded, as shown in Figure 3.4. The Stillinger criterion [151] is employed to define the cluster. If two atoms are separated by a distance less than a critical value, they are regarded as being within a cluster. In this work, the critical distance is taken to be $1.5\sigma_{Ar\text{-}Ar}$ [152],[153]. Moreover, if the distance between the solid surface and any atoms in a cluster is less than $3.5\sigma_{Ar\text{-}Ar}$, the cluster is identified as surface cluster. The simulation results within 12 ns, sufficiently to show the evolutions, are shown in Figure 3.4. For the NC cases (β = 0.275 with ΔT = 5 ~ 15 K), although n_c is not zero when ΔT increases to 15 K, n_{max} remains less

than 50 for most of the time. This indicates that the emerging surface clusters have not survived or developed into droplets for the period of time. For the DWC cases (β = 0.275 with ΔT = 25 ~ 35 K; β = 0.475 with ΔT = 5 ~ 15 K), the variations of n_c show similar trend. Initially, n_c starts to increase due to the condensing of vapor molecules after the surface is cooled. Subsequently, the coalescence of surface clusters occurs more quickly, which results in the decrease of n_c. Then, n_c fluctuates around a certain value after a peak has been reached. For β = 0.275, n_c fluctuates around 2 and 3 for ΔT = 25 K and ΔT = 35 K, respectively. For β = 0.475, n_c fluctuates around 2 and 1 for ΔT = 5 K and ΔT = 15 K, respectively. For some cases, the abruption of n_{max} indicates that large clusters coalesce or rupture. Additionally, Figure 3.4 also shows that the surface clusters appear earlier with ΔT and β increasing. For example, for β = 0.275, the appearance time of the surface clusters moves earlier from ca. 4 ns to ca. 1.5 ns when ΔT increases from 25 K to 35 K. As β increases, the bonding intensity increases and some molecules with lower total energy adhere on the solid surface already before the solid surface is cooled. This benefits the quick formation of surface clusters. Therefore, the clusters form quickly, and their size and number increase immediately when the surface is cooled. For FWC cases (β = 0.475 with ΔT = 25 ~ 35 K; β = 0.55 ~ 0.7 with ΔT = 5 ~ 35 K), the variation of n_c also proves the two different formation pathways of FWC (nucleation or adsorption-induced film). On surfaces with β = 0.475 (ΔT = 25 ~ 35 K) and β = 0.55 (ΔT = 5 ~ 35 K), at the initial period of time, some surface clusters appear and then the clusters grow and coalesce into a film, which leads to n_c = 1. On surface with β = 0.7 (ΔT = 5 ~ 35 K), the surface is fully covered by fluid molecules before the surface is cooled and n_c keeps unity within the simulation time.

In order to further analyze the heat transfer performance of surface condensation, the time evolution of the number of condensed molecules (n) is shown in Figure 3.5. The slope of each curve represents the condensation rate. It is seen that the condensation rate increases

with β and ΔT increasing. Reaching to the same n, for example n = 5000, it takes ca. 6.0 ns for the case with β = 0.475 and ΔT =15 K, while it only takes ca. 2.5 ns when ΔT increases to 35 K. When β decreases to 0.275, n is less than 5000 for all ΔT within the simulation time. For a fixed β, the slope of the curve increases with ΔT increasing, indicating that increasing ΔT significantly increases the condensation rate.

Adsorption could occur on any surface [154]. From the results in 1) in section 3.2.2, we see that the adsorption ability is dependent on β and has apparent effect on the formation of surface condensation mode. To further clarify this, Figure 3.6 shows the number of adsorbed molecules (N_{ad}) on the surfaces with different β before the surface is cooled (ΔT = 0 K). It is seen that the adsorption ability apparently increases with increasing β, which is a reason that FWC occur more readily with increasing β. N_{ad} increases from 133 to 1579 with β increasing from 0.275 to 0.7. The adsorbed molecules are evidently seen to form an ultra-thin film on the surface with β = 0.7. This adsorption-induced film leads to formation of FWC directly when surface is cooled.

Figure 3.7 shows the variation of accumulative energy transferred in different cases. The results show that heat transfer apparently increases with increasing ΔT and β. Considering that we focus on the onset of condensation and referring to our earlier work that the interfacial thermal resistance, rather than the bulk thermal resistance, dominates the condensation process in this stage [58], FWC has higher heat transfer than DWC when ΔT is fixed. However, we can also see that the slope of each curve for β = 0.55 and β = 0.7 (FWC) slightly decreases, which is due to the increase of bulk thermal resistance resulting from the growing of film thickness. For instance, it decreases from ca. 170 to 130 eV/ns in the simulation time for β = 0.7 and ΔT = 35 K.

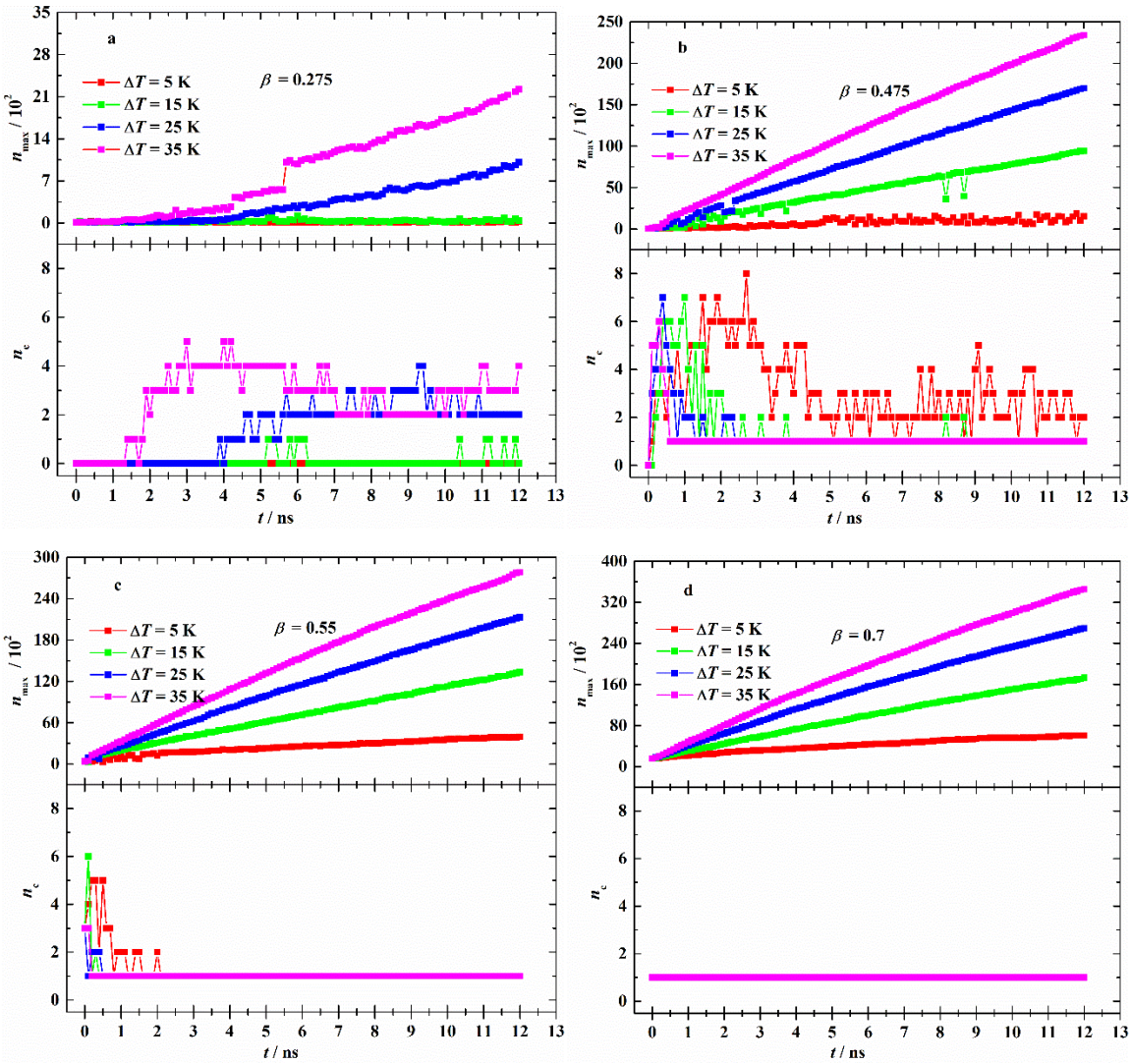

Figure 3.4: Time evolutions of maximum size cluster (n_{max}) and the number of surface clusters (n_c) for different temperature differences (ΔT) and surface wettabilities (β).

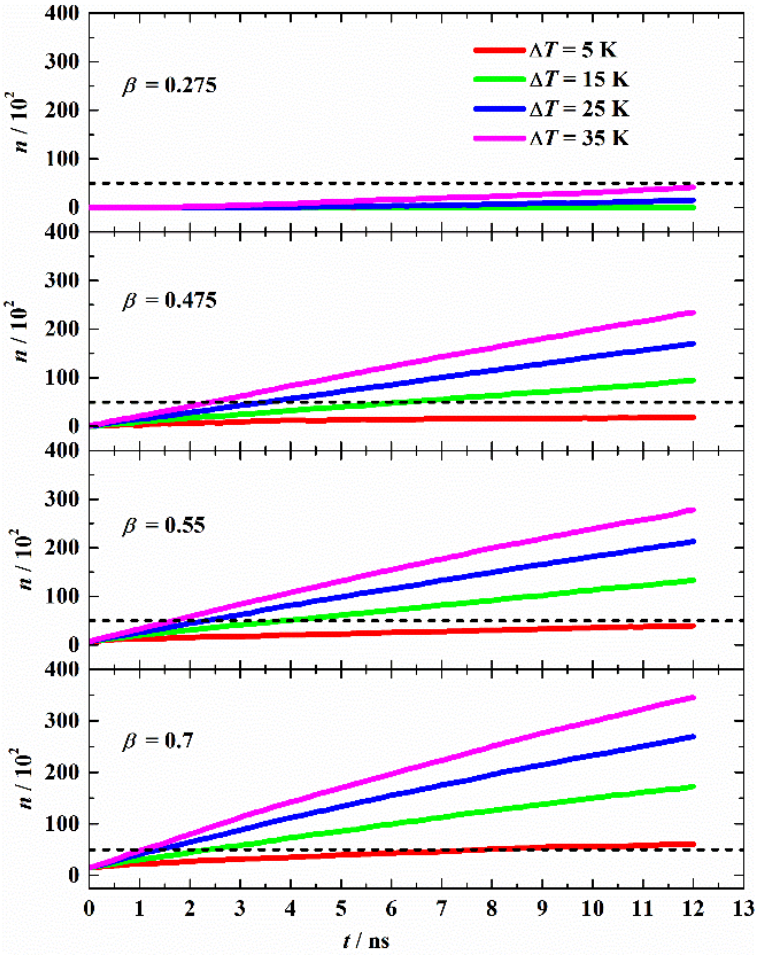

Figure 3.5: Time evolution of number of condensed molecules.

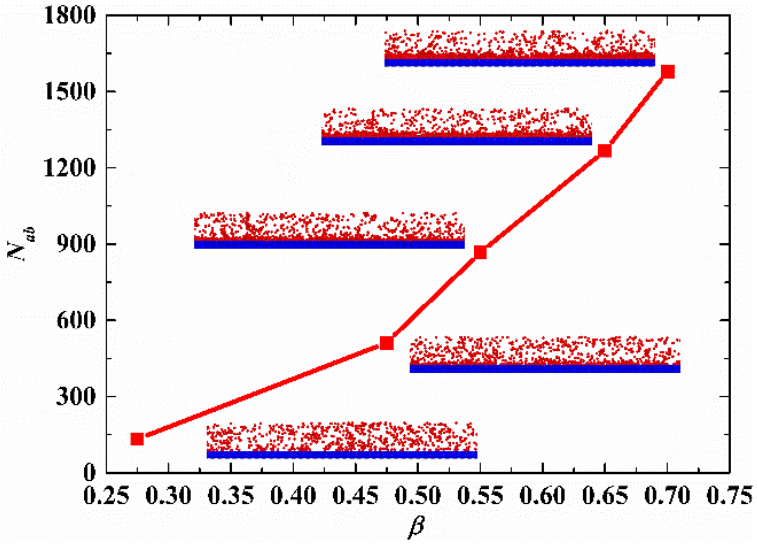

Figure 3.6: Number of adsorbed vapor molecules N_{ab} with different β before condensation.

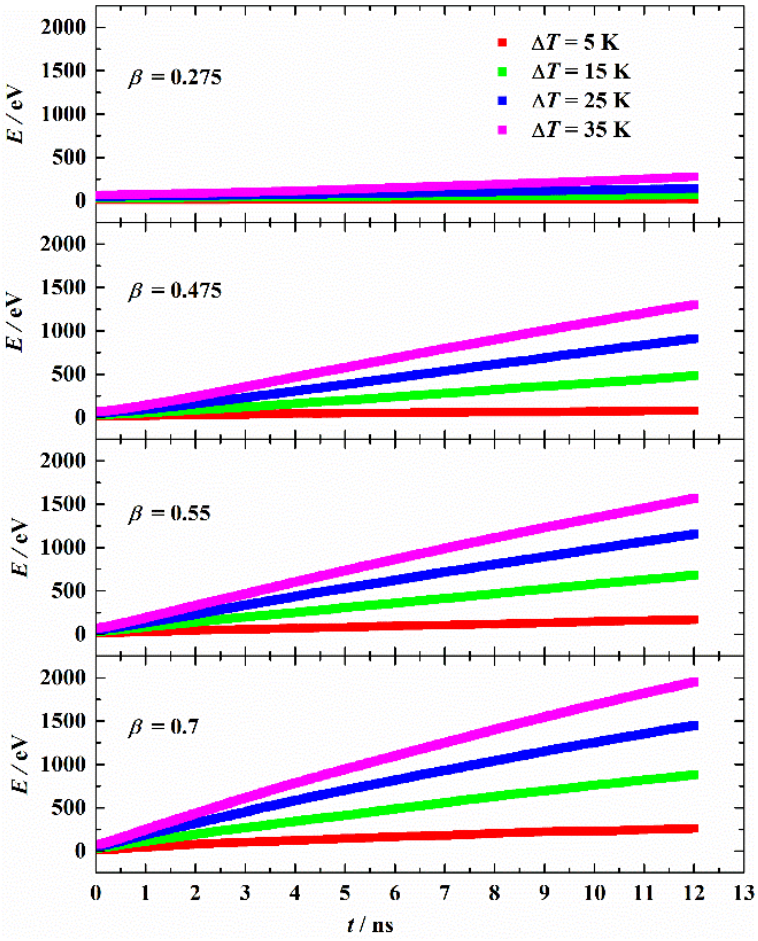

Figure 3.7: Time evolution of accumulated energy transferred.

3.2.3 Transition mechanisms between different surface condensation modes

As discussed above, we find that both DWC and FWC have two different pathways of formation. For convenience, the DWC cases resulting from nucleation and film rupture are denoted as DWC^n and DWC^r, respectively. Similarly, the FWC cases resulting from nucleation and adsorption-induced film are denoted as FWC^n and FWC^a. The transition mechanisms between neighboring surface condensation modes, i.e., between NC and DWC or between DWC and FWC, will be discussed below from the perspective of classical nucleation theory (CNT) and the dynamics of liquid film.

1) Transition mechanism between NC and DWC

According to CNT, nucleation is a non-spontaneous process and the formation of nucleus with critical number of molecules requires to overcome the free energy barrier ΔG^*. In other words, only when the free energy barrier is overcome could a newly formed cluster survive and develop into droplet. Additionally, the lower the free energy barrier, the more easily the surface condensation happens. This free energy barrier is given by

$$\Delta G^* = \frac{16\pi\gamma_{lv}^3}{3\rho_l^2\Delta\mu^2}F \tag{3-2}$$

where γ_{lv} is the liquid-vapor surface tension, ρ_l is the density of liquid, $\Delta\mu$ is the chemical potential difference between liquid (μ_l) and vapor (μ_v), and F is the Fletcher factor. F is a geometry factor, but it can also represent the ratio between heterogeneous and homogeneous free energy barrier. F varies from 0 to 1, indicating the surface condensation occurs from easily to hard. For a droplet on a flat surface, $F = (2-3\cos\theta+\cos^3\theta)/4$ and it is an increasing function of θ.

Firstly, the detailed effect of ΔT on ΔG^* is analyzed when β is fixed. Due to the increase of ΔT resulting from the decrease of the solid wall temperature (T_w), increasing ΔT significantly decreases the liquid temperature T_l. Figure 3.8 demonstrates the contact angle θ with different β and T_l. θ is obtained based on the density contour of droplets [48]. First, a cubic box with 7264 argon atoms is placed on the solid surface. Then, the system is equilibrated by the NVT ensemble for 4 ns. Finally, the density of argon molecules is sampled and averaged for 200 ps. Generally, θ increases with decreasing T_l when β is fixed, although the difference is small for lower β. Therefore, we easily have the correlations that the increase in ΔT leads to the decrease in T_w; correspondingly T_l will decrease, which then results in the increase in θ; thus, F also increases because it is an increasing function of θ; consequently, ΔG^* will increase ($\Delta T\uparrow \rightarrow T_w\downarrow \rightarrow T_l\downarrow \rightarrow \theta\uparrow \rightarrow F\uparrow \rightarrow \Delta G^*\uparrow$). According to ref. [155], γ_{lv} increases

with decreasing T_l. Therefore, we obtain the correlations that the increase in ΔT leads to the decrease in T_w; correspondingly T_l will decrease, which then results in the increase in γ_{lv}; consequently, ΔG^* will increase ($\Delta T \uparrow \rightarrow T_w \downarrow \rightarrow T_l \downarrow \rightarrow \gamma_{lv} \uparrow \rightarrow \Delta G^* \uparrow$). It is known that the ρ_l also increases with decreasing T_l. For $\Delta\mu$, decreasing T_l reduces μ_l due to higher stability at lower temperature for liquid but μ_v is constant due to the same initial vapor state for all cases, which leads to the increase in $\Delta\mu$. Considering our simulation results and analysis, when ΔT increases, the condensation intensity increases, thus ΔG^* should be lower theoretically. From this aspect, we can conclude that the ΔT-induced variation in $\rho_l^2\Delta\mu^2$ is always larger than that in $F\gamma_{lv}^3$. So we can obtain the correlations that the increase in ΔT leads to the decrease in T_w; correspondingly T_l will decrease, which then results in the increase in ρ_l and $\Delta\mu$; consequently, ΔG^* will significantly decrease ($\Delta T \uparrow \rightarrow T_w \downarrow \rightarrow T_l \downarrow \rightarrow \rho_l$ & $\Delta\mu\uparrow \rightarrow \Delta G^* \downarrow\downarrow\downarrow$). It is known that the variations of ρ_l, $\Delta\mu$ and γ_{lv} are dependent on the thermodynamic states of fluid. As the vapor state remains constant in our simulation, the term $16\gamma_{lv}^3/3\rho_l^2\Delta\mu^2$ is determined by fluid state. According to the above analysis, when T_l decreases, this term will decrease.

Secondly, the detailed correlation between β and ΔG^* is analyzed below. Based on Figure 3.8, it is shown that θ decreases with increasing β. Therefore, we can easily obtain that the increase in β leads to the decrease in θ; correspondingly F will decrease, which consequently results in the decrease in ΔG^* ($\beta \uparrow \rightarrow \theta \downarrow \rightarrow F \downarrow \rightarrow \Delta G^* \downarrow$). According to our earlier work [55], the increase of β results in the significant decrease of thermal resistance R_{th}, which reduces the temperature jump between fluid and solid surface, thus leads to the decease of T_l. Similarly, we have the correlations that the increase in β leads to the decrease in R_{th}; correspondingly T_l will decrease, which then results in the increase in γ_{lv}, ρ_l and $\Delta\mu$; consequently, ΔG^* will decrease ($\beta \uparrow \rightarrow R_{th} \downarrow \rightarrow T_l \downarrow \rightarrow \gamma_{lv}$ & ρ_l & $\Delta\mu \uparrow \rightarrow \Delta G \downarrow$). Therefore,

we conclude that increasing β lowers ΔG^*, which consequently promotes the onset of surface condensation.

Based on the above results and analyses, it is revealed that β and ΔT have significant effects on ΔG^*, which results in the transition between NC and DWC with β and ΔT varying. Due to the decreasing of ΔG^* with increasing β and ΔT, the NC-DWC boundary appreciably shifts towards lower β with ΔT increasing.

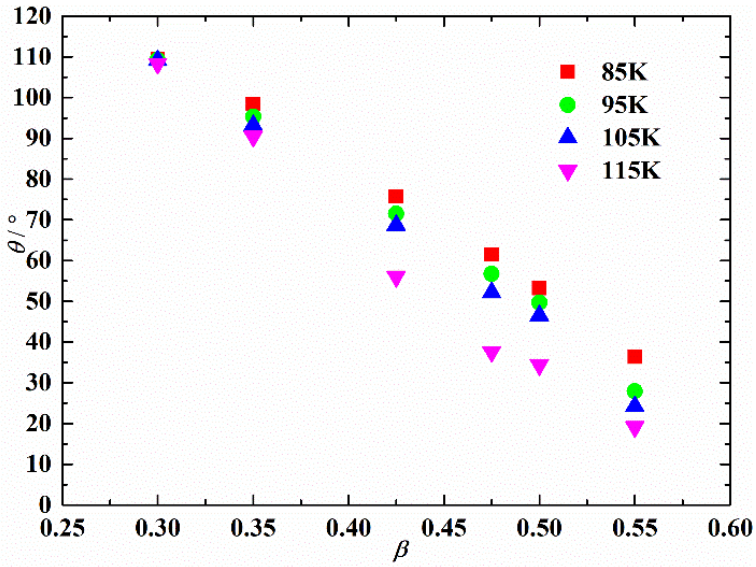

Figure 3.8: Surface contact angle (θ) with different β and liquid temperature T_l.

2) Transition mechanism between DWC and FWC

The transition between DWC and FWC occurs in the cases of DWC^r and FWC^n. The difference between them is in that the film-like condensate in DWC^r could finally contract and rupture into droplets and then develop into larger droplets. On the contrary, the film-like condensate in FWC^n eventually evolves into a complete film instead of rupturing into droplets. The film-like condensate tends to rupture at the locations with thinner film. Thus, it is reasonably necessary to investigate the stability of an existing nanoscale liquid film of different thicknesses on a solid surface with different surface characteristics.

Initially, a liquid film with different liquid molecule layers is set on the surface with β = 0.55 and thermally equilibrated at 110 K. Then, suddenly decreasing β to 0.45 is conducted and attempts to make the film rupture (see Figure 3.9). It is seen from Figure 3.9 that the liquid film with 5 and 8 layers of liquid molecules ruptures into droplets when β drops. On the other hand, a much thicker liquid film (9 layers) remains a complete film. The film with 5 layers ruptures faster than that with 8 layers. There are apparent droplets in 1 ns for the film with 5 layers, while the film with 8 layers does not rupture into droplets even up to 5 ns. Therefore, we conclude that liquid film intends to contract and rupture when β is lower, whereas when the liquid film is sufficiently thick, it remains to be film regardless of β. Moreover, it is found that the contraction and rupture of liquid film takes a period of time rather than instantly. Thicker liquid film is more stable and takes longer time to rupture. Therefore, as surface condensation occurs, there exists the competition between the trend that the uneven condensate film contracts and ruptures into droplets (large θ) favored by lower β (see in Figure 3.3(c) and Figure 3.9) and the trend that the uneven condensate film remains growing (large condensation rate) promoted by higher ΔT (see 2) in section 3.2.2). The stronger trend in the competition finally determines the transition between DWC and FWC. When the trend that the uneven condensate film contracts and ruptures into droplets favoured by lower β is relatively stronger, DWC occurs otherwise film-like condensate keeps growing to even condensate film and FWC is observed. However, for lower β cases, θ is dramatically large so the trend of contraction and rupture is significant. On the other hand, the trend the uneven condensate film remains growing promoted by increasing ΔT is limited. Therefore, the boundary between DWC and FWC shifts slightly towards lower β with ΔT increasing. It is seen that the condensation mode is primarily determined by β at the onset of surface condensation.

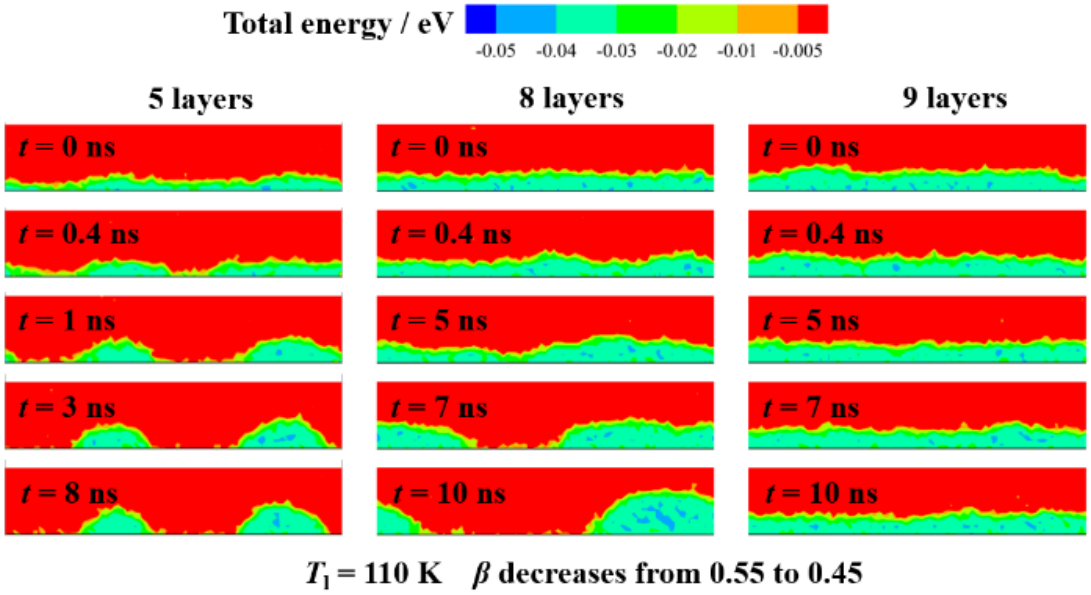

Figure 3.9: Time evolution of films with different thickness when β decreases.

3.3 Conclusions

The simulation results are summarized in Figure 3.10, a map schematically representing the condensation formation and mode transition determined by surface wettability β and vapor-to-surface temperature difference ΔT. Five formation mechanisms and two transition mechanisms of condensation mode are revealed. At low β and ΔT, the high free energy barrier ΔG^* prevents surface clusters to survive and therefore NC is observed (see (a) in Figure 3.10). The developments of both DWC and FWC are categorized as two apparently different formation pathways into droplet and film, respectively. Specifically, the formation of DWC could evolve from either nucleation (see (b) in Figure 3.10) or film-rupture (see (c) in Figure 3.10), and that of FWC could evolve from either nucleates (see (d) in Figure 3.10) or adsorption-induced film (see (e) in Figure 3.10). The transition between NC and DWC

(see (I) in Figure 3.10) is determined by ΔG^* according to classical nucleation theory. Lower ΔG^* (high β and ΔT) guarantees that surface clusters survive, and condensation occurs. As condensation proceeds, there emerges the competition between the trend that the uneven condensate film contracts and ruptures to droplet favored by lower β and the trend that the uneven condensate film remains growing promoted by higher ΔT. When the former trend is stronger than the latter one, DWC appears otherwise FWC appears (see (II) in Figure 3.10). We can see that both β and ΔT have significant effects on the formation of surface condensation and the condensation mode is primarily determined by β on the onset of surface condensation.

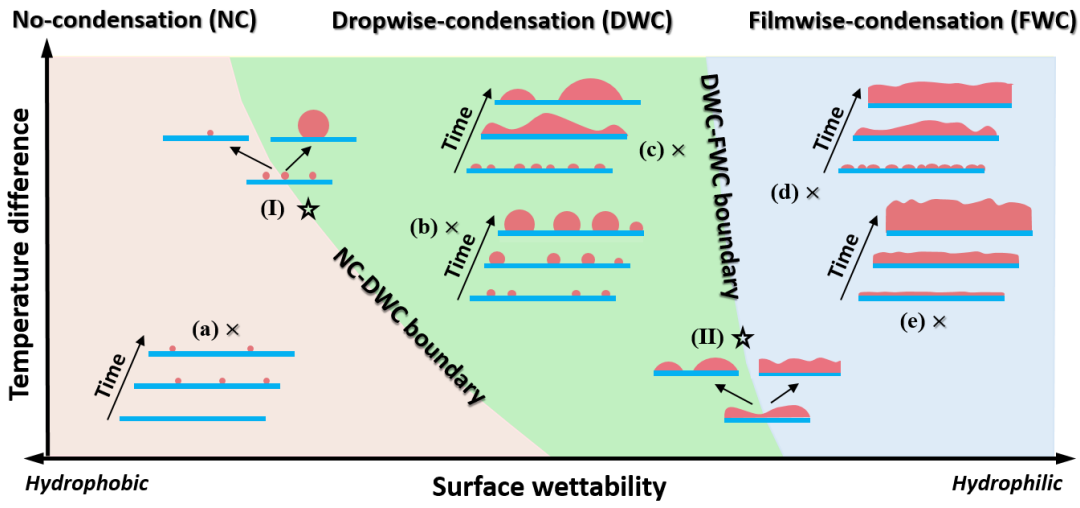

Figure 3.10: Schematic presentation of formation and transition mechanisms of surface condensation mode with β and ΔT. NC, DWC and FWC represent no-condensation in red, dropwise condensation in green and filmwise condensation in blue, respectively. Five mode formation mechanisms are: (a) NC; (b) DWC from nucleation; (c) DWC from film-rupture; (d) FWC from nucleation; (e) FWC from adsorption-induced film. Two mode transition mechanisms are: (I) Transition between NC and DWC; (II) Transition between DWC and FWC.

4 Nano-confined Surface Condensation on Tangentially External Force Field

In practice surface condensation occurs under external force field and its effect needs to be taken into account, where fluid flow and heat transfer are coupled. MD simulations [54] investigated features of surface condensation under external force field but mainly focused on how the composite nano-surface to sustain and enhance condensation heat transfer as well as the enhancement mechanism from the thermal resistance point of view. The detailed investigations have been rarely done on the surface condensation of nano-confined fluids under external force field. In this chapter, we will investigate the effect of external force field on nano-confined surface condensation using MD simulation. Owing to the strong effects of nanoscale surfaces, the surface wettability is also taken into account. Moreover, attentions in MD simulations of condensation have been mainly paid to cluster analysis [53], formation free energy [51], computational strategies [49],[50], surface properties [60] and so on. In this chapter, we will quantitatively analyze the energy balance and look at the mechanism of the effects of external force field from energy conversion point of view. Our work helps further understand the fundamental of practical nano-confined surface condensation and potentially offers a new way for artificial control and enhancement of surface condensation.

4.1 Computational methods

The surface condensation with external force field is of concern in the present work using MD simulation (see Figure 4.1). All the simulations are conducted using LAMMPS [141] (large-scale atomic/molecular massively parallel simulator) software package. The overall size of simulation box measures $l_x \times l_y \times l_z = 588.45 \times 39.23 \times 470.76$ Å. Owing to symmetry,

this simulation domain is just half of the nanochannel. Therefore, in the *y* and *z* directions, periodic boundary conditions are used, while in the *x* direction, fixed boundary condition is employed, and reflection boundary condition is also applied at the rightmost end. The solid wall constructed by Pt-like atoms is arranged on the leftmost region of the simulation box and the rest region is occupied by the Lennard-Jones (L-J) fluid of Ar. The 12-6 L-J potential function is employed for fluid-fluid interaction:

$$\varphi(r) = 4\varepsilon\left[\left(\frac{\sigma}{r}\right)^{12} - \left(\frac{\sigma}{r}\right)^{6}\right] \tag{4-1}$$

where r is the intermolecular separation, ε and σ are the energy and length characteristic parameters, respectively. The potential function is truncated at the cut-off radius $r_c = 3.5\sigma$, beyond which molecular interactions are ignored. $\varepsilon_{\text{Ar-Ar}} = 0.01040$ eV and $\sigma_{\text{Ar-Ar}} = 3.405$ Å are used. The solid wall is represented by three layers of Pt-like atoms arranged as a face-centered cubic (FCC) lattice and the length of the unit cell is 3.926 Å. Two extra layers of Pt-like atoms are fixed on the leftmost region of the solid wall to serve as a frame. The interaction between solid atoms is L-J type only with $\varepsilon_{\text{Pt-Pt}} = 0.521875$ eV and $\sigma_{\text{Pt-Pt}} = 2.475$ Å. The fluid-solid interaction is also governed by Eq. (4-1) but with different energy and length parameters, i.e., $\varepsilon_{\text{Ar-Pt}} = \beta\varepsilon_{\text{Ar-Ar}}$ and $\sigma_{\text{Ar-Pt}} = 0.91\sigma_{\text{Ar-Ar}}$, where β is fluid-solid bonding strength parameter indicating the surface free energy, or equivalently the surface wettability, because normally higher surface free energy suggests stronger surface wettability. All the simulations are performed in three stages with a time step of 5 fs. In stage 1 (equilibrium stage), the saturated vapor molecules at $T_v = 120$ K are uniformly arranged. The initial 3 ns allows the system to reach the thermal equilibrium state at 120 K, where the Langevin thermostat is used to maintain the temperature of both the wall and fluid. In stage 2 (steady-state stage), an external force is applied on each fluid molecule in the *z*-direction. Meanwhile, the thermostat applied on argon is removed and only the NVE ensemble is

employed for argon. The temperature control of the solid wall is still maintained at 120 K. The following 30 ns guarantees the system to reach a steady state, after which another 5 ns is employed to sample the properties, such as velocity and temperature. In stage 3 (condensation/cooling stage), the condensation process is triggered by suddenly reducing the surface temperature to 90 K and maintained afterwards for a period of 20 ns by the Langevin thermostat. To investigate the effects of external force field on condensation over surfaces with different free energies, two steps are carried out. In step one, the effect of external force field on condensation is primarily investigated with different external force (f_e) in the z direction from $0.0001\varepsilon\sigma^{-1}$ to $0.0007\varepsilon\sigma^{-1}$ (ε and σ employ Ar parameters.) and fixed β equal to 0.35. In step two, the effect of surface free energy on condensation is investigated with fixed f_e equal to $0.0005\ \varepsilon\sigma^{-1}$ and different β from 0.15 to 0.75. In order to conveniently evaluate the external force fields, Table 4.1 gives the exact values in real unit.

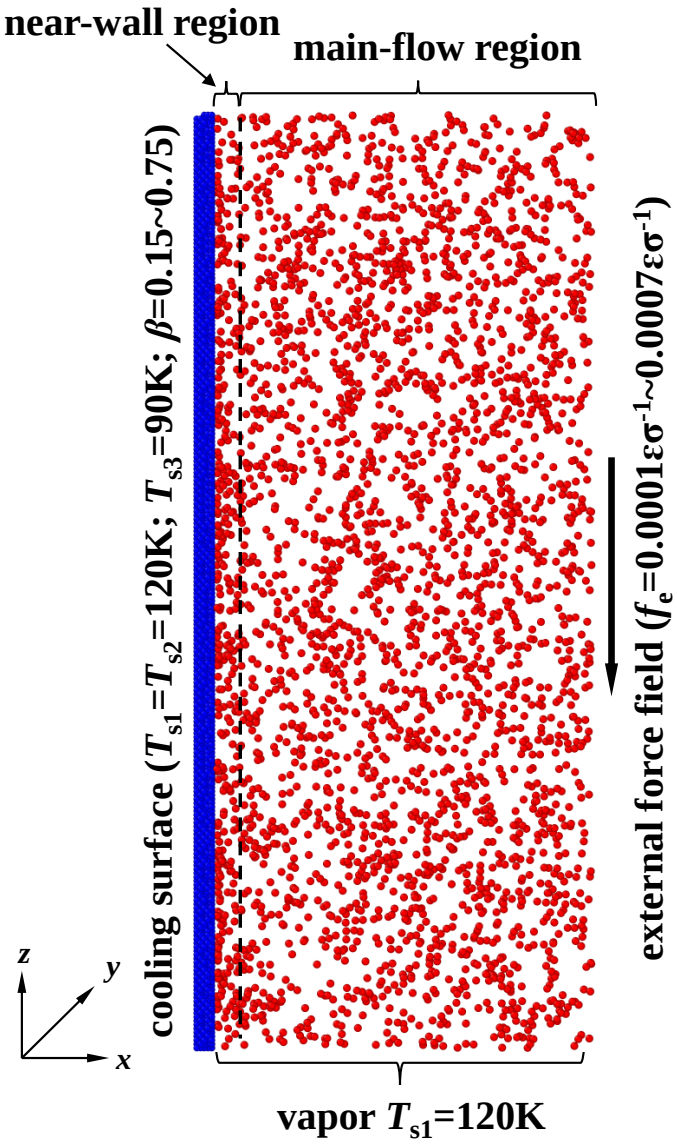

Figure 4.1: Schematic of computational model. The size of simulation box is $l_x \times l_y \times l_z$ = 588.45 × 39.23 × 470.76 Å. Solid atoms are in blue and fluid molecules are in red.

Table 4.1: External forces exerted on each fluid molecular in the present simulations.

f_e / eV·Å^{-1}	0.0001$\varepsilon\sigma^{-1}$	0.0002$\varepsilon\sigma^{-1}$	0.0003$\varepsilon\sigma^{-1}$	0.0004$\varepsilon\sigma^{-1}$	0.0005$\varepsilon\sigma^{-1}$	0.0006$\varepsilon\sigma^{-1}$	0.0007$\varepsilon\sigma^{-1}$
f_e / 10^{-15} N	0.4887	0.9774	1.4661	1.9548	2.4435	2.9322	3.4209

4.2 Results and discussion

4.2.1 Condensation dynamics

1) On surface with fixed wettability under different external force fields

In stage 2, the vapor molecules reach a steady state under different f_e. With fixed surface wettability (β = 0.35), the velocity in the z direction (v_z) and temperature profiles, shown in Figure 4.2, are found to be sensitive to f_e. When f_e increases, velocity gradient along the x direction rises, and the apparent slippage appears and increases at the solid-vapor interface. Correspondingly, temperature of the vapor increases, which allows the saturated vapor to become superheated and the degree of superheat increases. Meanwhile, the temperature jump and gradient along the x direction become larger with increasing f_e. From the top views, as shown in Figure 4.3(a), it is indicated that there is no significant difference of first layer of the liquid molecules between $f_e = 0$ and $f_e = 0.0007\varepsilon\sigma^{-1}$ cases. This is also confirmed by the detailed quantitative results shown in Figure 4.3(b) that the differences of density profiles under different f_e are generally small. Specifically, it can be seen, from the locally amplified inset in Figure 4.3(b), that the averaged density adjacent to the solid wall decreases from 0.0020 $Å^{-3}$ to 0.0011 $Å^{-3}$ with increasing f_e from 0 to $0.0007\varepsilon\sigma^{-1}$ due to the increase of fluid temperature resulted from the dissipated heat.

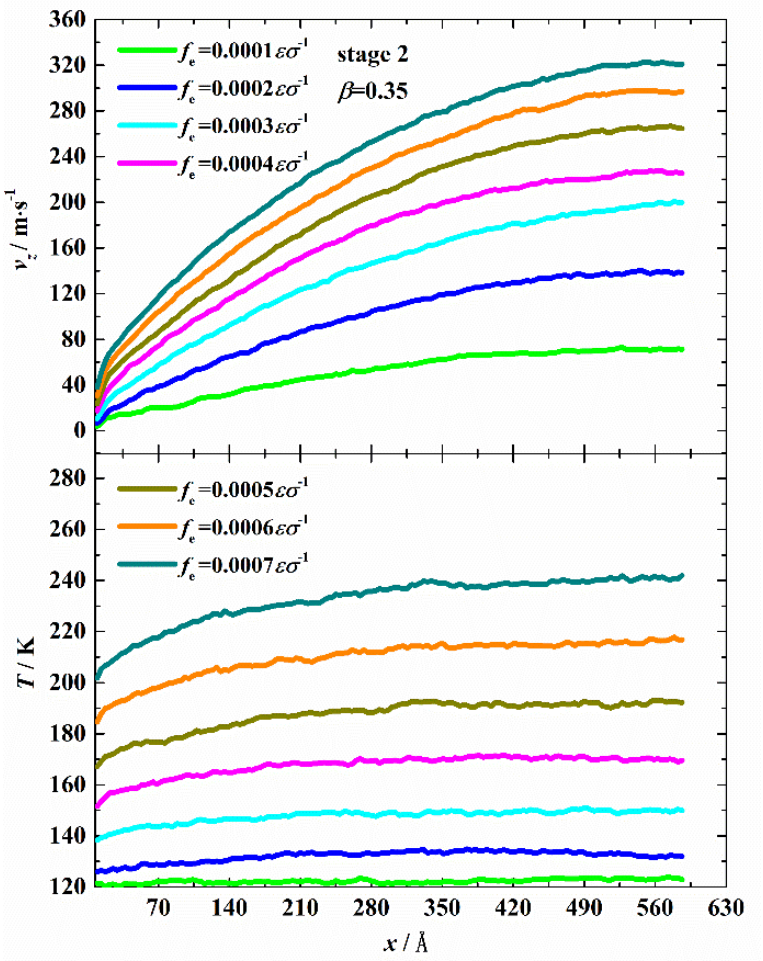

Figure 4.2 Velocity and temperature profiles of vapor molecules with β = 0.35 under different external force on stage 2.

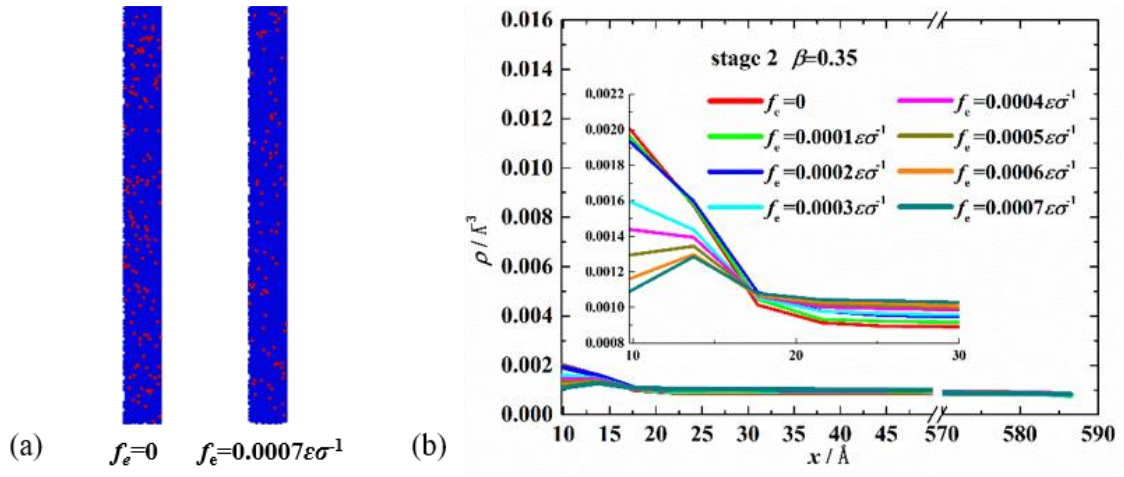

Figure 4.3: (a) Top view of first layer molecules adjacent to the solid wall. (b) Density profiles of vapor molecules with β = 0.35 under different external force on Stage 2.

In stage 3, when the surface temperature suddenly drops from 120 K to 90 K, the vapor molecules are immediately cooled by the wall surface. The transient density profiles in the *x*-direction under different f_e are given in Figure 4.4. It can be clearly seen that in the cases with $f_e \geq 0.0005\varepsilon\sigma^{-1}$, the density profiles during stage 3 rarely vary, which suggests that there is no surface condensation. For those condensation cases ($f_e < 0.0005\varepsilon\sigma^{-1}$), the condensate on the wall surface growing thicker is clearly indicated by the liquid density peaking and expanding as time evolves. Eventually, $f_e = 0$, $0.0001\varepsilon\sigma^{-1}$ and $0.0002\varepsilon\sigma^{-1}$ cases shape similarly in the density profile while $f_e = 0.0003\varepsilon\sigma^{-1}$ and $0.0004\varepsilon\sigma^{-1}$ cases shape another. By observing the animation of condensation under different f_e, it can be found that similar density profiles are due to the same number of primary droplets. For $f_e = 0$, $0.0001\varepsilon\sigma^{-1}$ and $0.0002\varepsilon\sigma^{-1}$ cases, finally there are two primary droplets during stage 3, while for $f_e = 0.0003\varepsilon\sigma^{-1}$ and $0.0004\varepsilon\sigma^{-1}$ cases, there is only one. Figure 4.5 shows the transient snapshots (t = 2, 4, 6, 8, 10, 12 and 14 ns) for three representative cases ($f_e = 0$, $0.0002\varepsilon\sigma^{-1}$ and $0.0004\varepsilon\sigma^{-1}$). No matter for $f_e = 0$ or other cases, primary droplets form through three over-lapping stages. Initially, obvious clusters are observed to deposit on the wall surface. Then, some clusters randomly migrate and coalesce with other clusters to form nuclei while the others disappear. Finally, a primary droplet emerges with upsizing by condensation of vapor molecules and numerous coalescences between those surviving nuclei. However, there are significant differences between these cases. Combining Figure 4.4 and Figure 4.5 together, it is clearly found that the existence of f_e can postpone the appearance of condensation when f_e is beyond to a certain threshold ($f_{cr} = 0.0005\varepsilon\sigma^{-1}$ for surface with β = 0.35). In the $f_e = 0$ case, obvious clusters can be observed at the initial time, while in the $f_e = 0.0004\varepsilon\sigma^{-1}$ case, they only do after 4 ns (see Figure 4.5). In addition, the densities for $f_e = 0.0003\varepsilon\sigma^{-1}$ and $0.0004\varepsilon\sigma^{-1}$ cases are apparently lower than those for $f_e = 0$, $0.0001\varepsilon\sigma^{-1}$ and $0.0002\varepsilon\sigma^{-1}$ cases, which suggests that the condensation intensity decreases with increasing f_e.

The essential reason is that f_e causes the dissipated heating effect, which further leads to the locally superheating state of vapor in vicinity of the wall surface. Due to the fact, after the surface temperature drops, the superheated vapor needs to be cooled to saturation state first before condensing, the strong dissipated heating effect greatly prevents the vapor molecules from condensing. The larger f_e, the larger degree of superheating and harder the condensation could occur. It can also be seen that even small droplets start to move downward after formation with larger f_e, which facilitates the coalescence between them and causes fewer primary droplets to emerge. For example, as shown in Figure 4.5, three primary droplets can be seen at 10 ns in f_e = 0 case while only two form in f_e = 0.0002$\varepsilon\sigma^{-1}$ case.

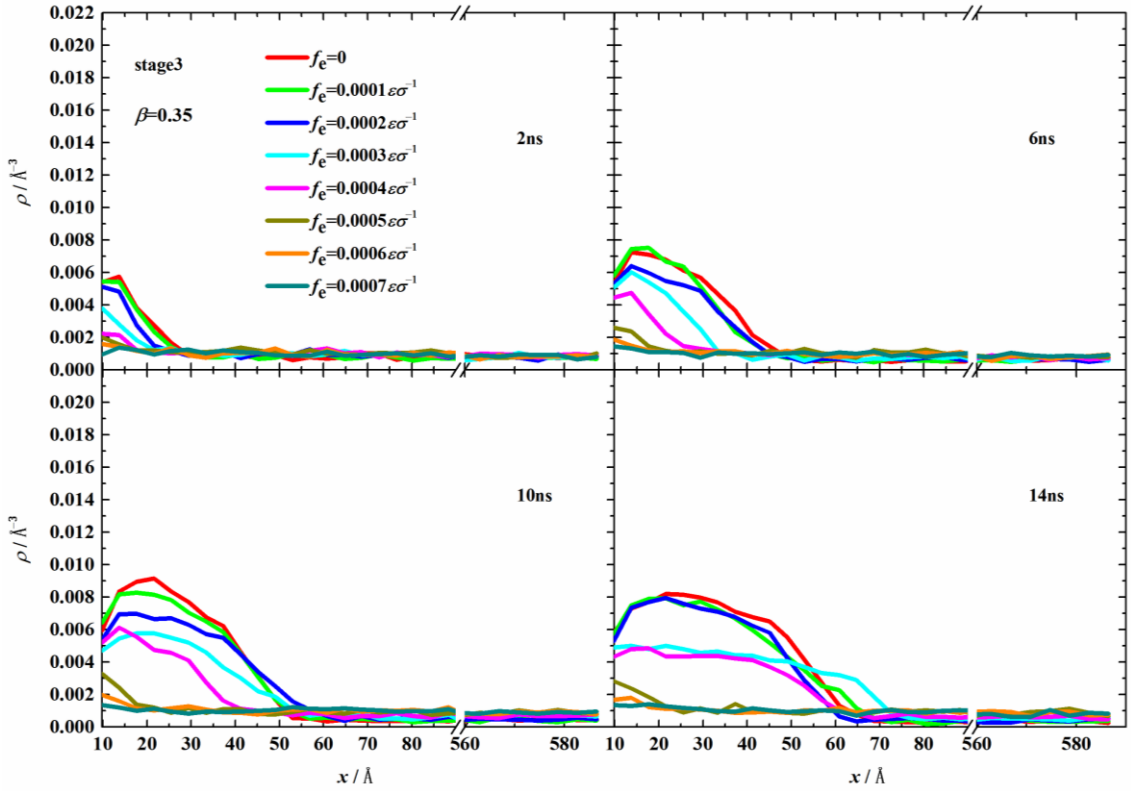

Figure 4.4: Transient density profiles with β=0.35 and different f_e during stage 3.

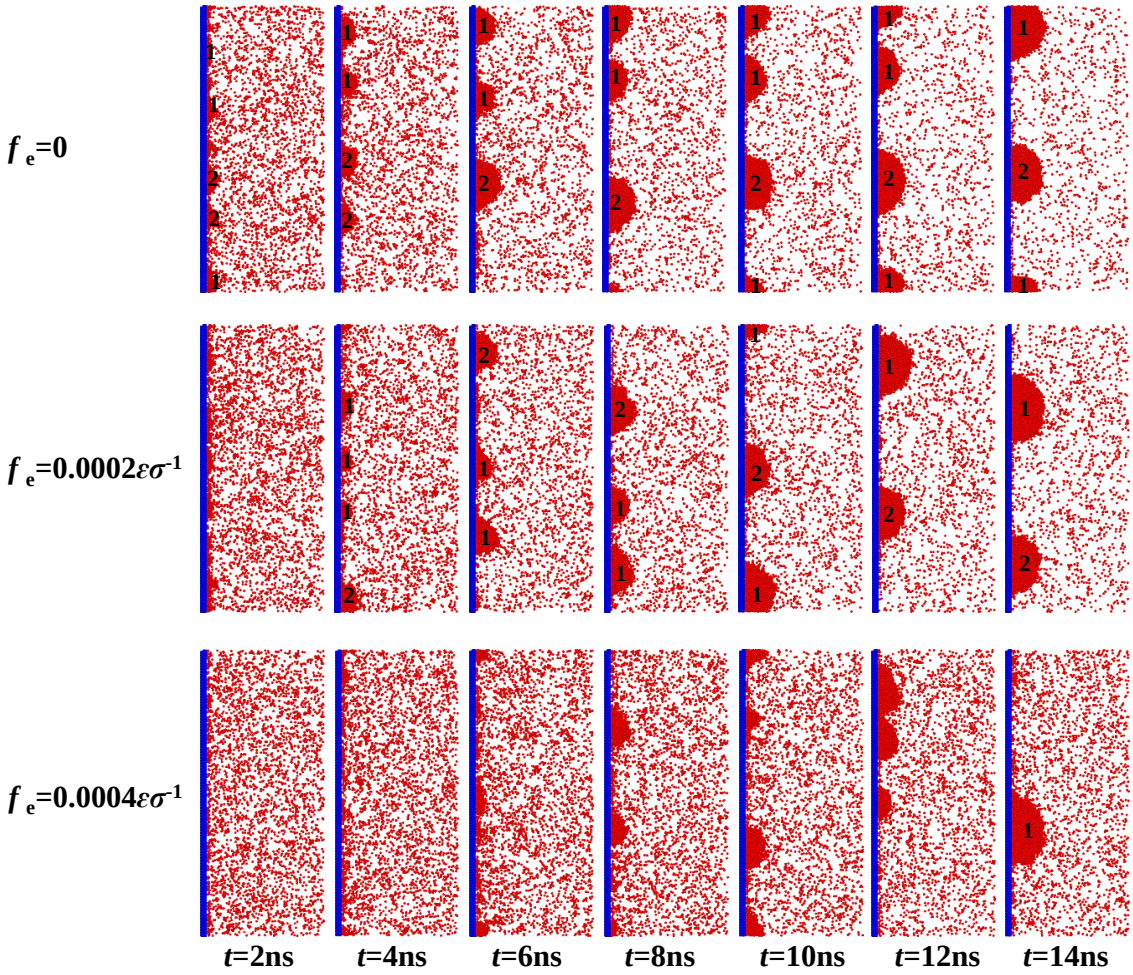

Figure 4.5: Transient snapshots with β=0.35 and different f_e during stage 3.

2) On surfaces with different wettabilities under fixed external force field

In Figure 4.6, based on whether there exists the velocity slippage under $f_e = 0.0005\varepsilon\sigma^{-1}$, velocity profiles in the z direction (v_z) are shown separately and different variations are observed. When β is small ($\beta \leq 0.45$), the velocity slip appears and decreases with increasing β. The variation near the main stream is not significant. All these lead to the velocity gradient along the x-direction increases with increasing β. Correspondingly, the temperature profile drops as a whole, whereas the temperature gradient tends to become steeper with increasing β. When β is large ($\beta > 0.45$), the slippage disappears and the difference in velocity profiles is not conspicuous, which results from stronger solid-fluid interaction. Consequently, the

increase in the fluid temperature is not dramatic and the difference between different β is small when $\beta > 0.45$ compared with small β cases. As for density profiles shown in Figure 4.7, when β increases, suggesting stronger solid-fluid interaction, the density adjacent to solid wall surface increases obviously. It can also be clearly seen from the top view of the first layer of fluid molecules adjacent to the solid wall surface, as shown in Figure 4.7(b). On surface with $\beta = 0.15$, the adsorbed fluid molecules are few and isolated to each other, while as β increases to 0.75, the wall surface is almost fully occupied by massive fluid molecules.

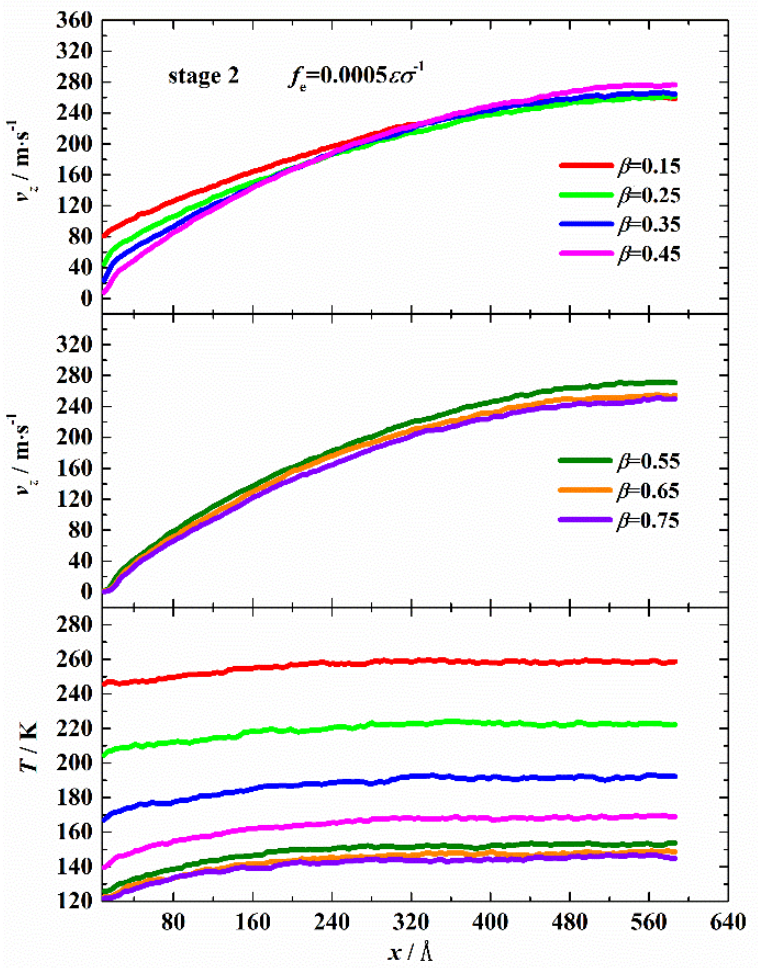

Figure 4.6: Velocity and temperature profiles of vapor molecules with different β under f_e = 0.0005$\varepsilon\sigma^{-1}$ on stage 2.

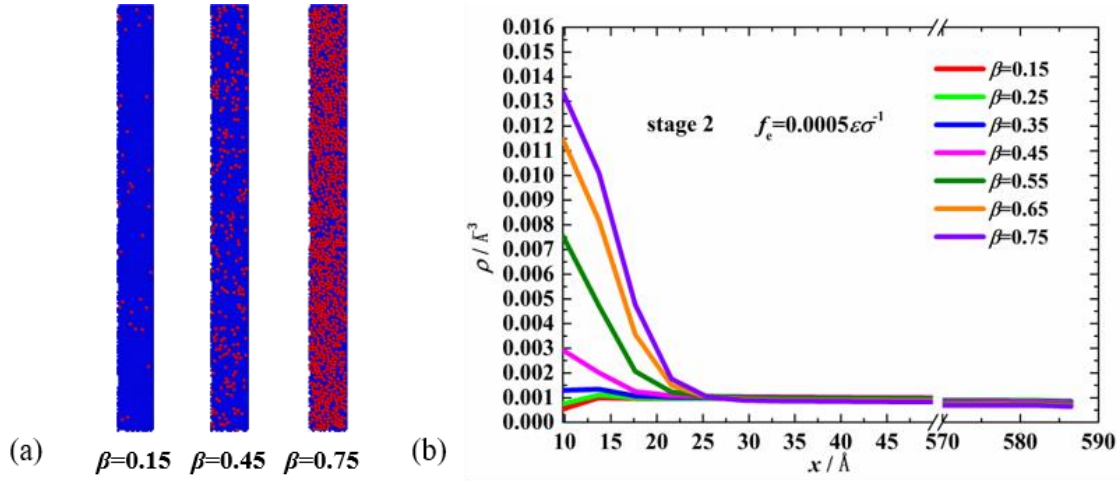

Figure 4.7: (a) First layer of molecules adjacent to solid wall (top view). (b) Density profiles of fluid molecules with different β under $f_e = 0.0005\varepsilon\sigma^{-1}$ in stage 2.

From Figure 4.8, it is seen that there are eventually three different kinds of density profiles in stage 3. When $\beta < 0.45$, the density profiles do not increase and vary significantly, which indicates that the condensate bulk hardly forms due to the existence of external force field and weak solid-fluid interaction. When $\beta = 0.45$, the density increases, and the condensate grows thicker with time before $t = 6$ ns. Comparatively, at $t = 10$ ns, although the condensate becomes thicker significantly, the density drops. This can be explained by the transient snapshots of condensation shown in Figure 4.8. It is seen that the film-like condensate grows continuously covering most of the wall surface at the initial time (see Figure 4.8 at $t = 2$ ns). Therefore, the density increases, and the condensate grows thicker. Then, the film-like condensate starts to contract and rupture. After rupturing, obvious discrete droplets appear and start to coalesce. Due to the existence of external force, the droplets move downward and coalesces with a primary droplet. As the primary droplet forms and grows large enough, the droplet moving becomes much faster. The droplet forms an asymmetric cap-like shape, of which the front part is denser. Consequently, the density distribution tends to flatten. When $\beta > 0.45$, the solid-fluid interaction is sufficiently strong so that numerous clusters instantaneously deposit on the wall surface when cooled and the surface is fully occupied by

fluid molecules immediately. As can be seen in Figure 4.8 and Figure 4.9 (t = 2 ns), the condensate film already becomes thick. With time evolving, the condensate film continues to grow thicker but the growth rate decreases and tends to cease at t = 10 ns. As the condensate film grows thick enough, it starts to move downward slowly with noticeable fluctuation at the liquid-vapor interface due to the strong frictional force.

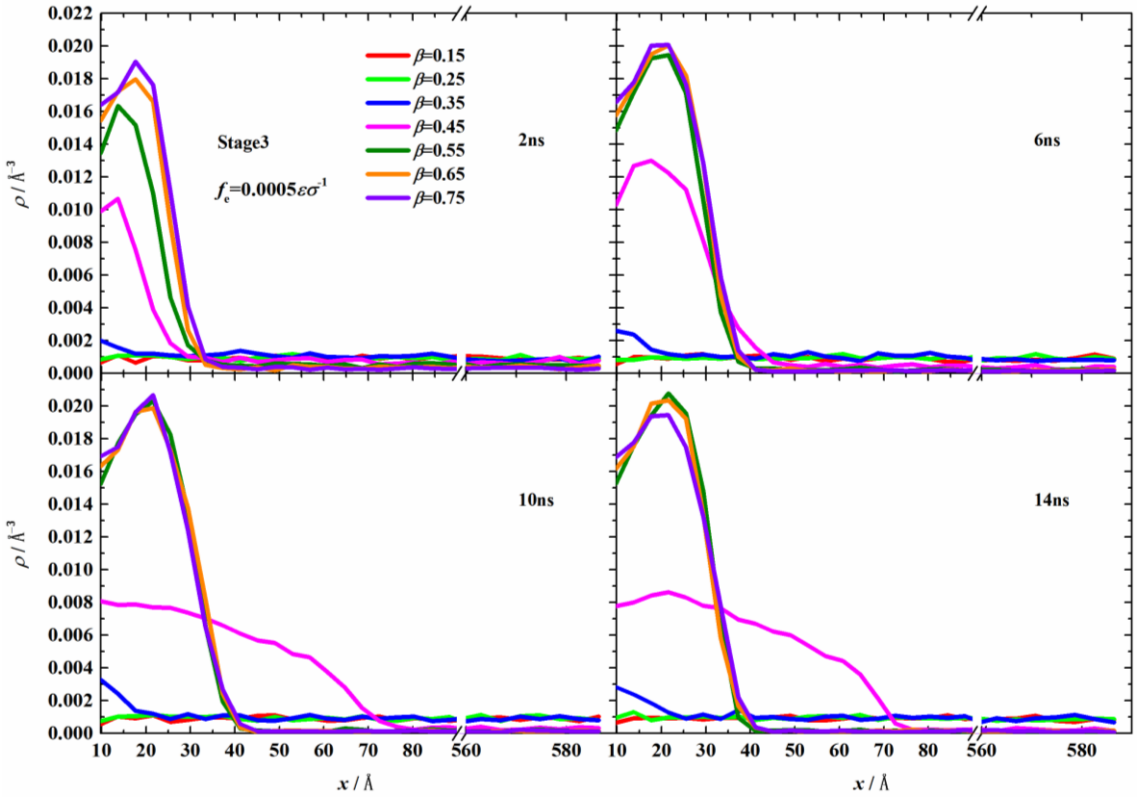

Figure 4.8: Transient density profiles with different β and f_e = 0.0005$\varepsilon\sigma^{-1}$during stage 3.

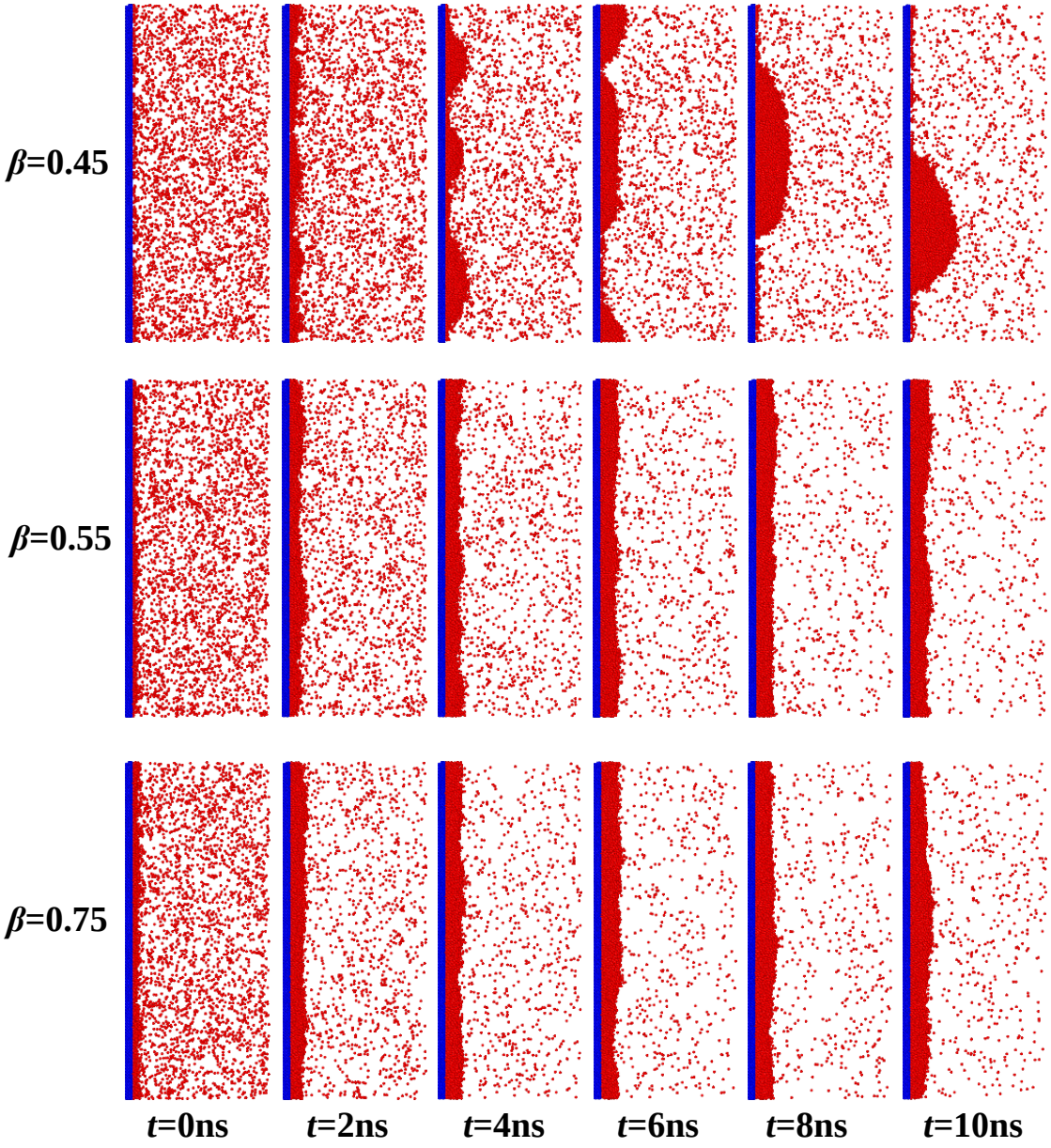

Figure 4.9: Transient snapshots with different β and f_e = 0.0005εσ-1 during stage 3.

4.2.2 Interfacial heat transfer

1) On surface with fixed wettability under different external force fields

Surface condensation is influenced by solid-fluid interfacial heat transfer. In order to understand the effect of external force field on condensation, we measured the interfacial thermal resistance (R) between the fluid and wall surface in stage 3. The interfacial thermal

resistance is determined as $R = \Delta T/QA$, where ΔT is the temperature difference between the wall surface and the first layer of fluid molecules adjacent to it; Q is the heat transfer rate, calculated as the slope of accumulated energy (E) against time; A is the heat transfer area. From Figure 4.10 and Figure 4.11, it is found that if there is no condensation ($f_e \geq 0.0005\varepsilon\sigma^{-1}$), the slope of E remains unchanged, namely Q keeps constant. Whereas, if condensation occurs ($f_e < 0.0005\varepsilon\sigma^{-1}$), Q drops with time, which qualitatively means that the condensation intensity decreases with time. Variations of R under different f_e are given in Figure 4.12, which indicates that R generally holds for all cases. It strongly verifies that R is the inherent property for a given couple of solid and fluid (liquid or vapor), and independent of the transient heat transfer processes with different f_e. In other words, once the solid wall and fluid (liquid or vapor) are primarily fixed, R is simultaneously determined and fixed regardless of different transient heat transfer rates (see $f_e = 0 \sim 0.0004\varepsilon\sigma^{-1}$ for solid-liquid cases with condensation and $f_e = 0.0006\varepsilon\sigma^{-1} \sim 0.0007\varepsilon\sigma^{-1}$ for solid-vapor cases without condensation occurring in Figure 4.12). On the other hand, also note that the solid-liquid and solid-vapor interfacial thermal resistances are significantly different in nature, therefore, when there exists liquid-vapor phase-change, e.g. condensation in the present work, R no longer holds but changes gradually and correspondingly, e.g. from the high value of solid-vapor interfacial thermal resistance to the low value of solid-liquid interfacial thermal resistance with notably transitional characteristics in the present work (see $f_e = 0 \sim 0.0002\varepsilon\sigma^{-1}$ cases before $t = 4$ ns, $f_e = 0.0003\varepsilon\sigma^{-1}$ case before $t = 8$ ns, $f_e = 0.0004\varepsilon\sigma^{-1}$ case before $t = 10$ ns and $f_e = 0.0005\varepsilon\sigma^{-1}$ case for whole simulation time-span in Figure 4.12).

In order to further investigate how f_e determines the surface condensation, two intentionally designed cases of $f_e = 0.0005\varepsilon\sigma^{-1}$ near-wall (f_e is just exerted on fluid molecules on near-wall region where the width of x direction is r_c, shown in Figure 4.1) and $f_e = 0.0005\varepsilon\sigma^{-1}$ main (f_e is exerted on every fluid molecule except that situated on near-wall region, namely

main-flow region) are carried out. Informative and distinct results are acquired that the variations of E, Q and R for $f_e = 0.0005\varepsilon\sigma^{-1}$ near-wall case are completely in accord with $f_e = 0$ case whereas those for $f_e = 0.0005\varepsilon\sigma^{-1}$ main case agree well with $f_e = 0.0005\varepsilon\sigma^{-1}$ case (see Figure 4.10-Figure 4.12). The results clearly show that the exertion of external force field on all fluid molecules is equivalent to that on the non-near-wall fluid molecules in the mainstream. This means that the external force field influences the surface condensation, including the onset and intensity, through the fluid bulk rather than the solid-fluid interface. Referring to the concepts in our previous work that the influencing factors to micro/nanofluidic phenomena can be categorized as either boundary or bulk factors [43], the external force field is clearly a bulk factor, rather than a boundary factor, to surface condensation. On the other hand, it is notable that the external force field does show indirect influence on the solid-fluid interfacial thermal resistance through direct influence on the surface condensation resulting from the generation of dissipated heat.

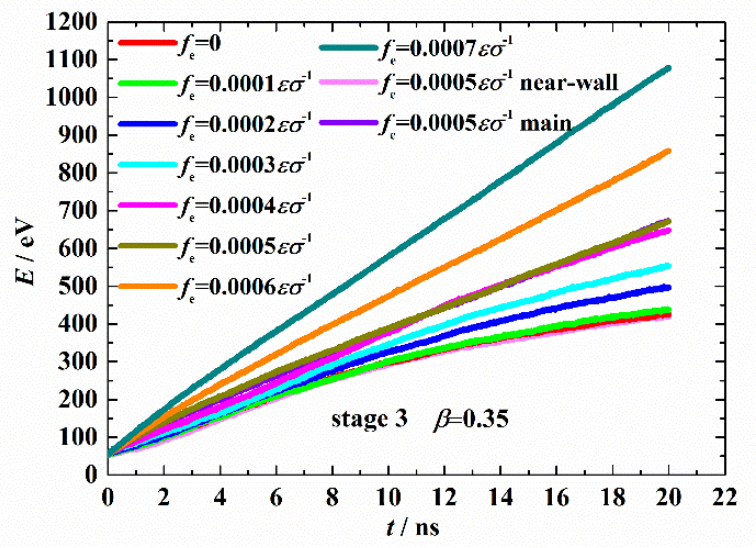

Figure 4.10: Time evolution of total heat transfer accumulation on surface with $\beta = 0.35$ under different external force during stage 3.

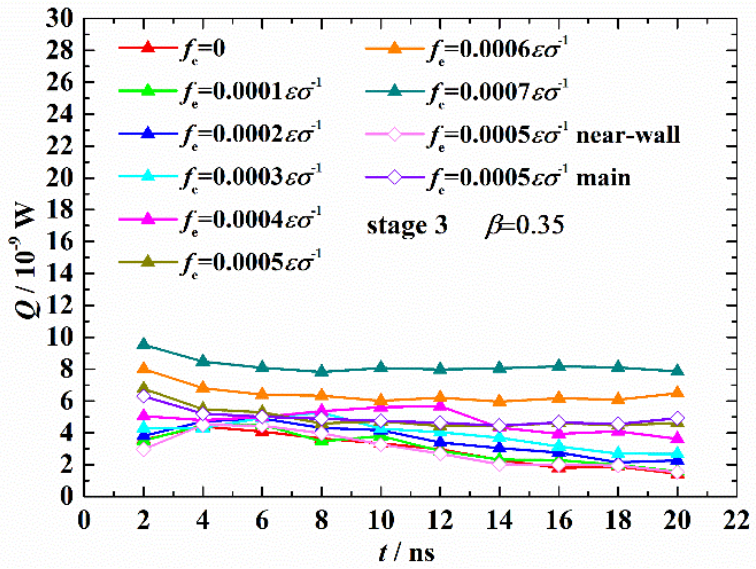

Figure 4.11: Time evolution of heat transfer rate on surface with β = 0.35 under different external force during stage 3.

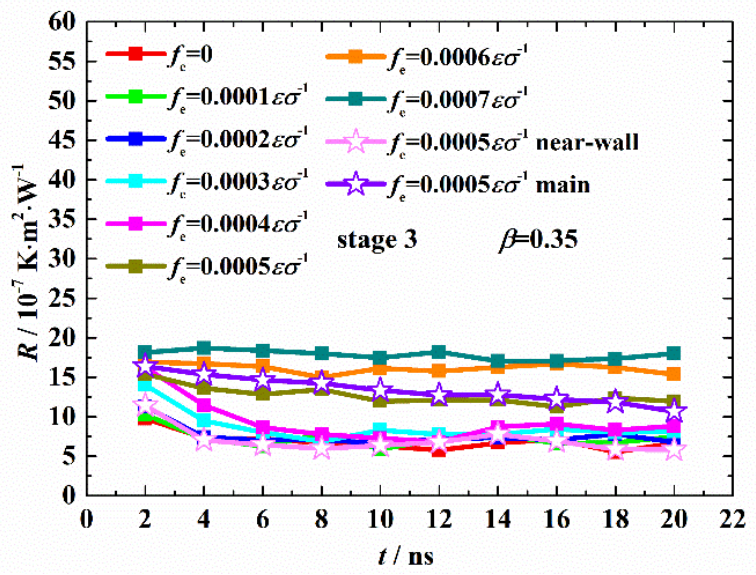

Figure 4.12: Time evolution of interfacial thermal resistance (R) on a surface with β = 0.35 under different external force fields during stage 3.

2) On surfaces with different wettabilities under a fixed external force field

Similarly, the variations of E, Q and R against time with different β and f_e = 0.0005$\varepsilon\sigma^{-1}$ are statistically obtained during stage 3, as shown in Figure 4.13-Figure 4.15. We find that Q

stays at low value (< 7×10^{-9} W) and almost remains the same in non-condensation (NC) cases ($\beta \leq 0.35$). For condensation cases ($\beta > 0.35$), Q, which indicates the condensation intensity, increases with increasing β at the initial time but deceases with time, as shown in Figure 4.13 and Figure 4.14. Due to the high condensation intensity, Q drops more dramatically with increasing β. For the dropwise condensation (DWC) case ($\beta = 0.45$), the condensation process does not cease during our simulation time, whereas, for the filmwise condensation (FWC) cases ($\beta > 0.45$), the condensation process ceases before $t = 14$ ns. As for R, it is highly sensitive to β. Generally, R decreases with increasing β following a nonlinear law [43]. When β is relatively large, the difference of R between cases with different β is much smaller, as shown in Figure 4.16. All these results strongly suggest that the surface wettability exerts a significant effect on surface condensation.

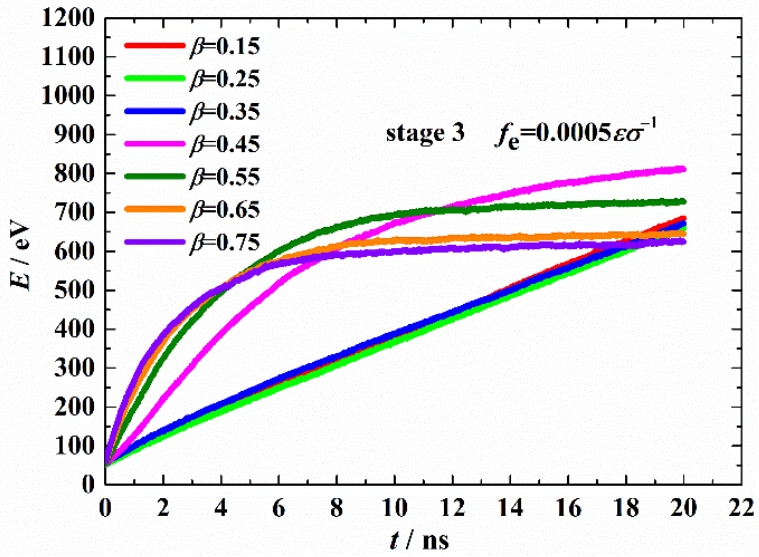

Figure 4.13: Time evolution of total heat transfer accumulation with different surface wettabilities under $f_e = 0.0005\varepsilon\sigma^{-1}$ during stage 3.

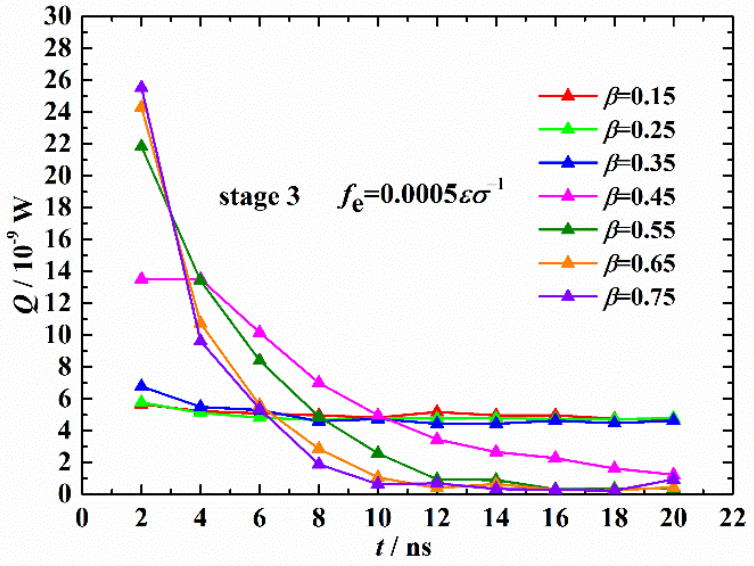

Figure 4.14: Time evolution of heat transfer rate with different surface wettabilities under f_e = 0.0005$\varepsilon\sigma^{-1}$ during stage 3.

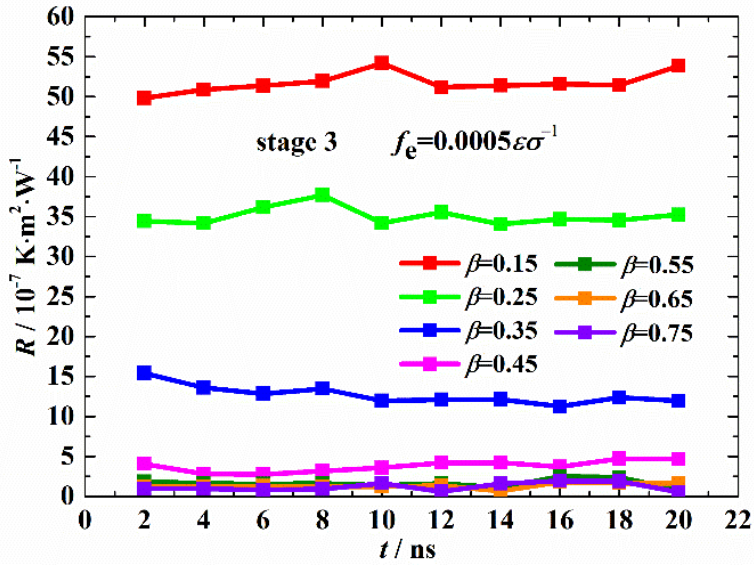

Figure 4.15: Time evolution of interfacial thermal resistance (R) with different surface wettabilities under f_e = 0.0005$\varepsilon\sigma^{-1}$ during stage 3.

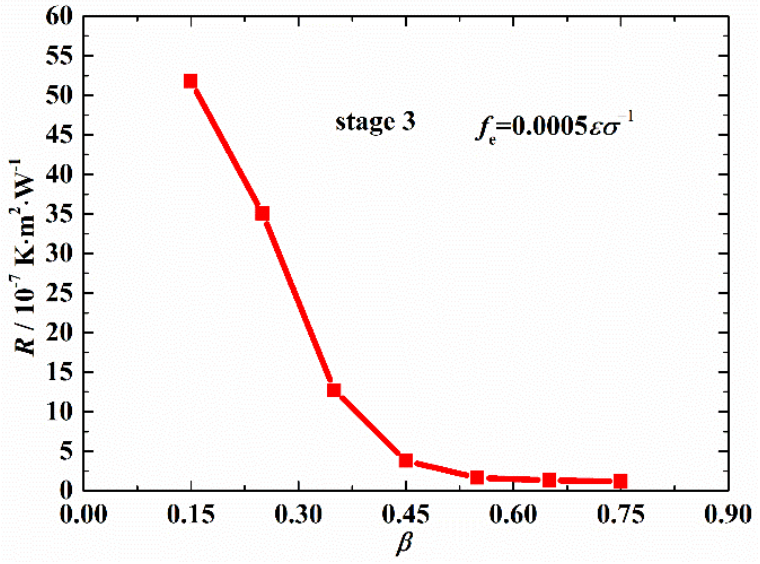

Figure 4.16: Interfacial thermal resistance (R) against different surface wettabilities under f_e = 0.0005$\varepsilon\sigma^{-1}$ during stage 3.

4.2.3 Energy conversion

To reveal the fundamental mechanism of effect of f_e on condensation from an energy point of view, energy conversion analysis has been carried out based on energy balance. The internal energy (U), microscopically defined as the sum of thermal kinetic energy and potential energy, can be employed as the indicator of whether condensation/cooling occurs and how intensive it is. Figure 4.17 and Figure 4.18 show the time-evolutions of changes in U for different cases during stage 3. It is seen that for NC cases, U slightly decreases at the initial time, then gradually converges to a certain value (marked in Figure 4.17 and Figure 4.18) after about 10 ns. The convergence value increases with increasing f_e and decreasing β. For condensation cases, U shows dramatic change when f_e = 0 ~ 0.0004$\varepsilon\sigma^{-1}$ and β = 0.45 ~ 0.75. It is also seen that U changes more dramatically for FWC compared with DWC cases, which indicates that FWC is more intensive than DWC. All FWC cases almost cease after about 10 ns and U converges to a certain value with slight difference between different cases. On the contrary, DWC cases apparently last after 10 ns. Due to the dissipated heating effect of f_e,

vapor molecules are superheated, and the degree of superheating, as well as the initial values of U before cooling, increases with increasing f_e and decreasing β. Generally, when the surface is cooled, U decreases correspondingly. Note that this is a pure cooling process without condensation. Then, if U stops decreasing and holds afterward, no condensation occurs. If U continues to decrease dramatically, condensation occurs. Moreover, the more dramatically U changes, the more intensive the condensation and more likely the filmwise condensation. It is clearly shown from Figure 4.17 and Figure 4.18 that both f_e and β can significantly influence the nano-confined surface condensation.

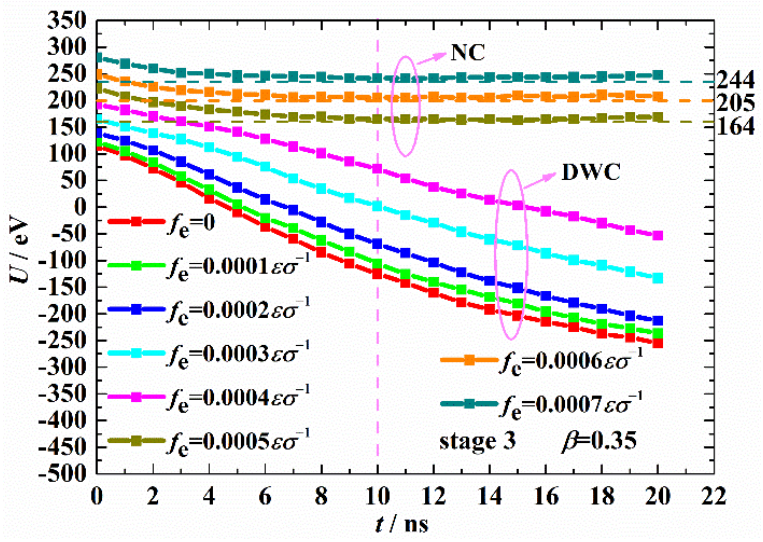

Figure 4.17: Time evolution of the internal energy (U) with β = 0.35 under different external forces during stage 3

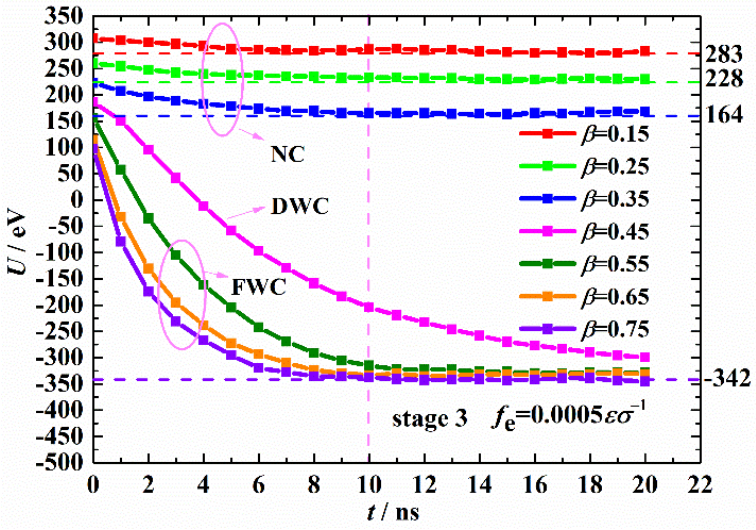

Figure 4.18: Time evolution of the internal energy (U) with different surface wettabilities under $f_e = 0.0005\varepsilon\sigma^{-1}$ during stage 3.

For NC cases, U remains steady after 10 ns, suggesting condensation is unlikely to occur. Therefore, we carry out energy conversion analysis based on the following equation:

$$E_Q = \Delta U + \Delta E_K + W \tag{4-2}$$

in the time span of $t = 0 \sim 10$ ns, where ΔU and ΔE_K are the changes in internal energy and macroscopic kinetic energy; W and E_Q are the work done by external force and heat transferred from the fluid to the wall. The quantitative results are tabulated in Table 4.2 and Table 4.3. To verify the energy balance, E_Q and $\Delta U+\Delta E_K+W$ are compared with the relative deviations (RDs). It is found that almost all RDs are within ±4%, which guarantees the energy balance in Eq. (4-2) considering the statistical fluctuation. Generally, no matter for the cases with same β and different f_e or with different β and same f_e, the energy conversions obey the unified mechanism. Figure 4.19 schematically illustrates the energy conversions based on Eq. (4-2).

For condensation cases (see $f_e = 0\sim0.0003\varepsilon\sigma^{-1}$ in Table 4.2 and $\beta = 0.45\sim0.75$ in Table 4.3), it is found that the heat transferred from fluid to solid mainly comes from ΔU (60~100%), releasing latent heat through the phase-change process. On the other hand, two other sources

contributing to E_Q are identified to be secondarily W (0~36%) and thirdly ΔE_K (0~11%). Note that the case of $f_e = 0.0004\varepsilon\sigma^{-1}$ and $\beta = 0.35$ does not fully follow the above regulation (ΔU, W and ΔE_K respectively contribute 37%, 61% and 2%) due to its transitional condensation state, therefore not considered. When condensation occurs, the work done within the bulk fluid (W) completely converts into heat and dissipated through the solid wall. Meanwhile, E_K decreases due to the frictional effect at the solid-liquid interface. The corresponding change in E_K (ΔE_K) finally converts into heat and dissipated through the solid wall. In principle, ΔE_K and W, which both result from f_e, are dissipated by the friction and viscosity, and finally lead to heating effect to the fluid as an internal heat source, which can be clearly supported by the fact that when f_e is removed ($f_e = 0$), both ΔE_K and W disappear simultaneously, as seen in Table 4.2.

However, for non-condensation cases, either very strong viscous and frictional dissipations heating effect due to large f_e (see $f_e = 0.0005\varepsilon\sigma^{-1} \sim 0.0007\varepsilon\sigma^{-1}$ in Table 4.2) or very large interfacial thermal resistance due to small β (see $\beta = 0.15 \sim 0.35$ in Table 4.3) keeps the bulk vapor temperature higher than the saturation temperature and denies the occurrence of condensation though U decreases a little, releasing sensible heat, due to the cooling of vapor molecules by the solid wall surface. Meanwhile, W due to f_e mostly converts into dissipated heat while slightly contributes to the increase in E_K. Therefore, it is found that W and ΔU respectively contribute firstly (86~94%) and secondly (7~17%) to E_Q whereas ΔE_K gives negative contribution (-1~-3%).

Table 4.2: Energy conversions for cases with β = 0.35 under different external force fields (t = 0 ~ 10 ns).

f_e	ΔU	ΔE_K	W	$\Delta U+\Delta E_K+W$	E_Q	RD
eV·Å^{-1}	eV	eV	eV	eV	eV	%
0	-224.2	0.0	0.0	-224.2	-227.5	-1.43
0.0001$\varepsilon\sigma^{-1}$	-222.5	-2.7	-11.9	-237.1	-237.5	-0.19
0.0002$\varepsilon\sigma^{-1}$	-189.8	-9.0	-46.8	-245.6	-249.8	-1.70
0.0003$\varepsilon\sigma^{-1}$	-173.6	-13.6	-104.1	-291.4	-301.1	-3.30
0.0004$\varepsilon\sigma^{-1}$	-111.3	-5.2	-181.4	-297.8	-314.5	-5.45
0.0005$\varepsilon\sigma^{-1}$	-52.9	9.2	-277.5	-321.3	-330.8	-2.94
0.0006$\varepsilon\sigma^{-1}$	-40.3	9.8	-380.9	-411.4	-418.8	-1.80
0.0007$\varepsilon\sigma^{-1}$	-41.7	10.0	-487.9	-519.6	-523.8	-0.80

Table 4.3: Energy conversions for cases with different surface wettability under f_e = 0.0005$\varepsilon\sigma^{-1}$ (t = 0 ~ 10 ns).

β	ΔU	ΔE_K	W	$\Delta U+\Delta E_K+W$	E_Q	RD
-	eV	eV	eV	eV	eV	%
0.15	-23.7	3.8	-298.9	-318.8	-321.0	-0.68
0.25	-28.2	6.1	-288.2	-310.3	-313.0	-0.86
0.35	-52.9	9.2	-277.5	-321.3	-330.8	-2.94
0.45	-383.5	-66.7	-164.6	-614.8	-613.1	0.27
0.55	-467.4	-70.5	-103.8	-641.7	-629.5	1.91
0.65	-449.6	-57.9	-76.7	-584.2	-570.2	2.42
0.75	-438.3	-51.5	-66.0	-555.8	-542.8	2.37

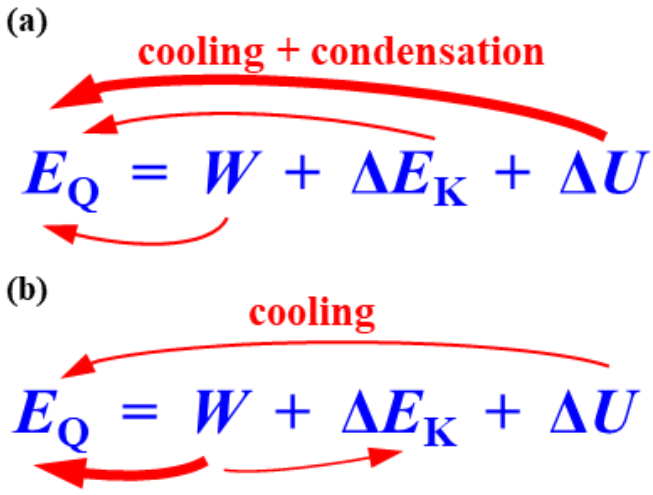

Figure 4.19: Energy conversion analyses for (a) condensation and (b) no-condensation cases (bold arrows indicate primary contributions).

Based on the above energy conservation analyses, the heat transferred from fluid to solid can be divided into two categories. One is the latent and sensible heats originated from the cooling and condensation, or pure cooling, of the fluid, which is represented by Q_c. The other is the dissipated heat generated due to the existence of the external force field, which is represented by Q_f. The proportional contributions of Q_c and Q_f in different cases based on f_e and β are illustrated in Figure 4.20 and Figure 4.21, respectively. It is clearly seen that Q_c decreases and Q_f increases with increasing f_e and decreasing β. When f_e is small (β = 0.35) or β is large ($f_e = 0.0005\varepsilon\sigma^{-1}$), condensation occurs in either FWC or DWC mode and the heat transferred from fluid to solid mainly comes from Q_c. When f_e increases above a critical value of ca. $f_{cr} = 0.0004\varepsilon\sigma^{-1}$ (β = 0.35) or β decreases below a critical value of ca. β_{cr} = 0.45 ($f_{cr} = 0.0005\varepsilon\sigma^{-1}$), condensation never occurs, and the heat transferred from fluid to solid wall surface mainly comes from Q_f. It has been reported that the surface wettability is significant in determining the condensation mode and intensity. More importantly, it has not been reported that the existence of the external force field can postpone and even suppress the occurrence of condensation. Note that the surface wettability is normally regarded as a

pretreating factor that cannot be easily and artificially changed during operation whereas the external force field is often a process factor that can be flexibly controlled in-situ, e.g., electrostatic and magnetic force fields.

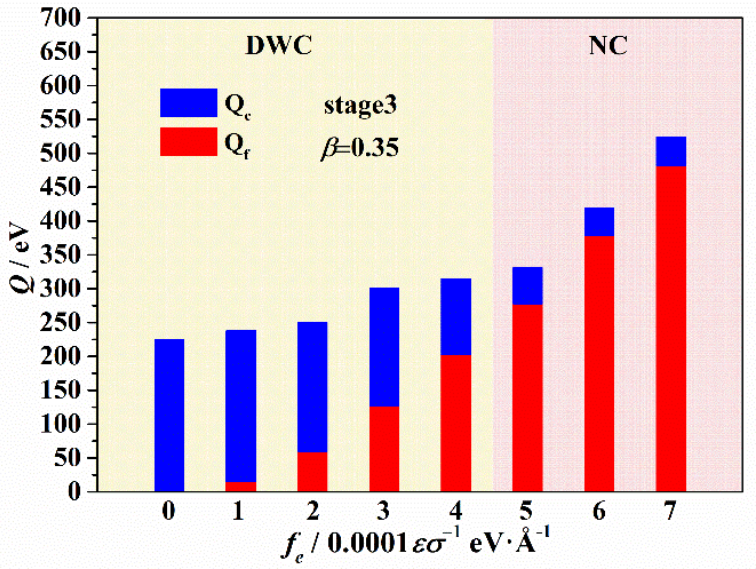

Figure 4.20: Different heat generation from 0 to 10 ns on surface with β = 0.35 under different external force. The dropwise condensation (DWC) and no-condensation (NC) cases are shown in light yellow and red backgrounds.

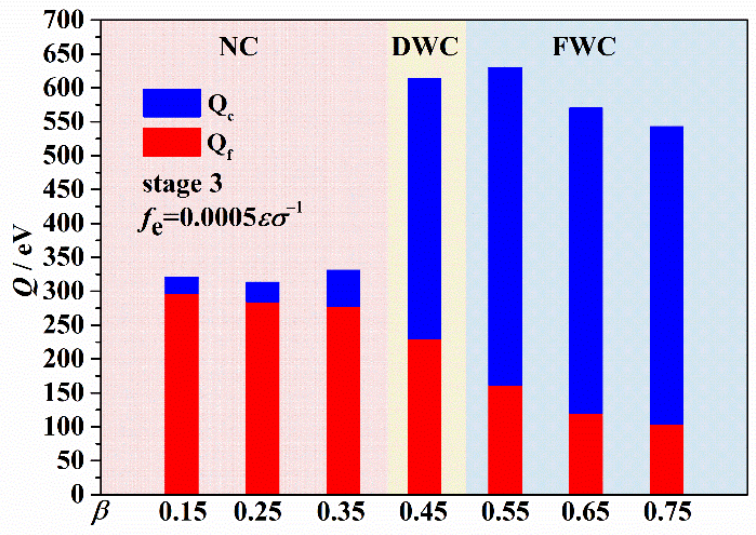

Figure 4.21: Different heat generation from 0 to 10 ns with different surface wettability under f_e = 0.0005$\varepsilon\sigma^{-1}$. The no-condensation (NC), dropwise condensation (DWC) and filmwise condensation (FWC) cases are shown in light red, yellow and blue backgrounds.

4.3 Conclusions

In the present work, we investigate the dynamic behaviors of nano-confined surface condensation with different β and f_e using MD simulations in the views of heat transfer and energy conversion. The simulation results show that both the velocity slip and temperature jump become larger with increasing f_e and decreasing β. Meanwhile, the existence of the velocity slip shows significant influence on the increase of fluid temperature. The density profiles for different f_e vary slightly on stage 2. Contrastively, those for different β show obvious difference and the density near the wall surface increases with increasing β. Asymmetric droplet is observed due to f_e, which promotes the coalescence of droplets after nuclei form. Meanwhile, increasing f_e postpones or even suppresses the onset of surface condensation when it reaches a certain critical value ($f_{cr} = 0.0005\varepsilon\sigma^{-1}$ for surface with $\beta = 0.35$).

Based on the heat transfer analysis, it can be found that f_e, as a bulk factor, shows indirect effect on R through direct influence on the surface condensation resulting from the generation of dissipated heat. In addition, when R increases with decreasing β, the solid-vapor interfacial thermal resistance becomes significantly larger than the solid-liquid one.

Based on the energy balance analysis, for condensation cases, the heat transferred from fluid to solid mainly comes from the change in U, while for non-condensation cases, the dissipated heats are the major contributions to this heat. In all cases, W mainly converts into dissipated heats, only except for the no-condensation case where a small proportion of W converts into E_k. We classify the heat transferred from fluid to solid into two categories, namely Q_c (due to condensation/cooling) and Q_f (due to f_e). It is found that Q_f increases and dominates the total heat with increasing f_e and decreasing β. It is also found that Q_f plays an

important role as the internal heat source and suppresses the further decrease of U, consequently the condensation is weakened or even inhibited.

5 Growth and Self-jumping of Single Condensed Droplet on Nanostructured Surfaces

Due to the limitation of the observation technique and the difficulty of fully eliminating coalescence interference, most of previous experimental studies carried out the investigation about the characterization of the self-jumping of individual droplet without condensation and just artificially dispensed the droplet. Additionally, with the observation of the self-jumping of single-microdroplet driven by the Laplace pressure, it has been raised that if nanodroplet can also achieve self-jumping driven by the Laplace pressure difference stored within the droplet as viscous forces during droplet bursting becomes more significant in the nanoscale [87]. Molecular dynamics (MD) method has been widely used to investigate the surface condensation in nanoscale and provides an effective avenue to overcome the experimental limitation [48],[52],[55],[58],[156]. Therefore, in this chapter, we employed MD method to demonstrate the effectiveness of Laplace pressure driven single-nanodroplet jumping and clearly characterize the growth and self-jumping of single condensed droplet on super-hydrophobic nanostructured surface with local hydrophilic pinning site. Additionally, the effect of the feature of the pinning site is preliminary discussed here. Our work enriches the understanding of the droplets self-jumping driven by the Laplace pressure and sheds light on the achievement of passive method for condensate removal, self-cleaning, thermal management and so on.

5.1 Computational methods

In this work, the growth and self-jumping of single condensed droplet on nanostructured surfaces were investigated using MD method. All the simulations are carried out using

LAMMPS (large-scale/molecular massively parallel simulator) software package [141]. The simulation model consists of a superhydrophobic nano-groove with a hydrophilic pinning site and argon-like fluid, as shown in Figure 5.1 The overall size of the simulation box measures $l_x \times l_y \times l_z = 80a \times 94a \times 142a$, where a is lattice constant with $a = 0.392$ nm. In the x and y directions, periodic boundary conditions are employed, while in the z direction, the fixed boundary condition is used, and the reflection boundary condition is also applied at the uppermost end. The nanostructured surface is constructed by Pt-like atoms arranged in a face-centered cubic (FCC) lattice with a lattice constant of 0.392 nm. To save the computational cost, the solid surface only consists of three layers of Pt-like atoms and one extra layer of Pt-like atoms is fixed underneath to serve as a frame. In the simulation, the nano-groove has a fixed depth (H) of $35a$ and width (W) of $20a$ but for its hydrophilic pinning site, different sizes (A_i) are introduced ($A_i = 4a \times 4a$, $8a \times 8a$, and $12a \times 12a$). In this work, all the atomic interactions are modeled by the Lennard-Jones (LJ) potential:

$$\varphi(r) = 4\varepsilon\left[\left(\frac{\sigma}{r}\right)^{12} - \left(\frac{\sigma}{r}\right)^{6}\right] \tag{5-1}$$

where r is the intermolecular separation, ε and σ are the energy and length characteristic parameters, respectively. For the interaction between fluid atoms, $\varepsilon_{ff} = 0.0104$ eV and $\sigma_{ff} =$ 3.40 Å. For the interaction between solid atoms, $\varepsilon_{ss} = 0.521875$ eV and $\sigma_{ss} = 2.475$ Å. Between solid and fluid atoms, $\varepsilon_{fs} = \beta\varepsilon_{ff}$ and $\sigma_{fs} = 0.91\sigma_{ff}$, where β is fluid-solid bonding strength parameter indicating the surface free energy, or equivalently the surface wettability. A larger value of β suggests higher surface free energy and stronger surface wettability. According to our previous work [157], $\beta = 0.1$ is chosen to describe the interaction between atoms of superhydrophobic nanostructured surface and fluid atoms. For the interaction between atoms of local pinning site and fluid atoms, β is chosen to be 0.4 and 1.0, representing hydrophilic and superhydrophilic sites, respectively. For the convenience of

later expression, the amphiphilic nanostructured surfaces are labeled as β = (0.1, 0.4) and β = (0.1, 1.0) and the surface wettability of the pinning site is noted by β_i. For all interactions, the potential function is truncated at the cut-off distance $r_c = 3.5\sigma_{ff}$, beyond which atom interactions are ignored.

All the simulations are performed with a time step of 5 fs. In the equilibrium stage, the vapor molecules of 123988 are uniformly arranged in the simulation system at T = 115 K and the initial 2.5 ns guarantees the system to reach a thermal equilibrium state using a Berendsen thermostat. Afterwards, the surface temperature is suddenly decreased to 84 K to initiate the occurrence of condensation. Simultaneously, a vapor supply region with a thickness of l_z /14 is arranged at the uppermost end, where the temperature and density are maintained at a saturation state. For the fluid except for those in the vapor supply region, the added thermostat is removed and only NVE ensemble is employed.

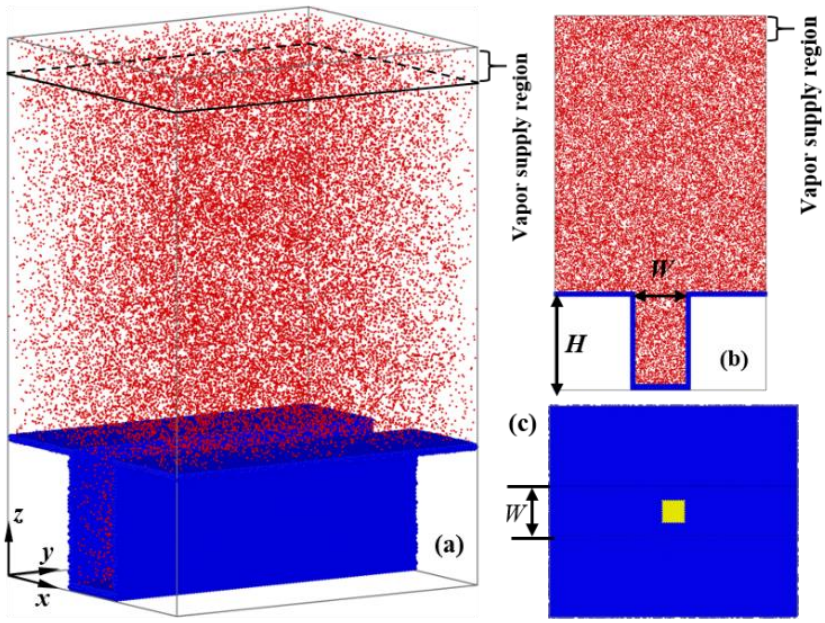

Figure 5.1: (a) Schematic of the computational model. Superhydrophobic solid atoms are in blue, hydrophilic solid atoms are in yellow, and fluid molecules are in red. (b) Front view of the simulation system. (c) Top view of the nanostructured surface. *H* and *W* represent the depth and width of nano-groove.

5.2 Results and discussion

5.2.1 Growth and Self-jumping

To clearly characterize the growth and self-jumping dynamics of single condensed droplet on the nanostructured surface, the nanostructured surface with β = (0.1, 0.4) and $A_i = 8a \times 8a$ is chosen here and finally a condensed droplet with radius of 7.5 nm is observed self-jumping from the nanostructured surface. This successfully proves, using MD method, that droplet self-jumping driven by the Laplace pressure difference is also efficient for nano-sized droplet. The snapshots of fluid condensation dynamics are shown in Figure 5.2(a) and correspondingly the trajectory of the droplet centroid in the *z* direction (z_c) is collected (see Figure 5.2(b)). On the basis of observations, we generally divide the condensation process before the droplet self-jumping from the nanostructured surface into two stages: incubation and burst stages.

(1) Incubation stage

According to the classical nucleation theory (CNT), surface condensation is a nonspontaneous process and only when the Gibbs free energy barrier is overcome could a nucleus survive and develop into a droplet. The lower the free energy barrier, the more easily the surface condensation happens. Based on our previous study [157], larger β can diminish the Gibbs free energy barrier and promote the onset of surface condensation. Thus, after the surface temperature drops from 115 to 84 K, a droplet nucleates from the hydrophilic pinning site and then smoothly grows. Due to the confinement from the superhydrophobic groove walls in the *x*-*z* plane, the growth of droplet in this plane is squeezed and naturally deformed to a pancake shape instead of a circular shape (see t = 35 ns in Figure 5.2(a)). Comparatively, the droplet freely grows in the *y*-*z* plane parallel to the nano-groove and its shape remains nearly circular (see t = 35 ns in Figure 5.2(a)). During this process, the whole droplet is embedded in the groove and the radii of curvature for the bottom interface ($R_b(t)$)

and top interface ($R_t(t)$) of the droplet are nearly same, as illustrated in Figure 5.2(c). The top interface of the condensed droplet continuously moves upward with a constant contact angle ($\theta_t(t)$) and $R_t(t)$ due to the occurrence of condensation, see in Figure 5.2(d) and Figure 5.2(e). Gradually, the upper front of the growing droplet emerges from the groove and the emerging part frees from the constraint of the groove (see t = 107.5 ns in Figure 5.2(a)). When the triple-phase contact line of the top interface reaches the groove edges, the baseline for $\theta_t(t)$ changes from the vertical plane of the groove wall to the horizontal plane of the groove top (see Figure 5.2(c)), which leads to a significant drop in $\theta_t(t)$ in Figure 5.2(e). Subsequently, the emerging part of the condensed droplet can also freely grow in the *x*-*z* plane. In this stage, z_c smoothly increases as the droplet grows (see Figure 5.2(b)). The measured widest length of the droplet (L_{max}) in the *y*-*z* plane also steadily increases (see Figure 5.3).

(2) Burst stage

As seen in Figure 5.2(a), after the triple-phase contact line of the top interface reaches the groove edges, the droplet top grows with pinned contact line at the sharp groove edges during the following condensation process. Gradually, we observed that L_{max} starts decreasing due to the shrinkage of the droplet in the *y*-*z* plane (see Figure 5.3). The reason of this is that the droplet top can not only freely grow and expand in the *y*-*z* plane but also in the *x*-*z* plane, which makes it recover to a spherical shape due to surface tension. Since then, the growth of the droplet moves to the burst stage and $\theta_t(t)$ and $R_t(t)$ start increasing obviously (see Figure 5.2(d) and Figure 5.2(e)). In contrast, $R_b(t)$ remains small, and its change is not significant due to the confinement of the groove wall. Thus, as the droplet grows further, a Laplace pressure difference ($\Delta P = \gamma_{lv}(1/R_b - 1/R_t)$, where γ_{lv} is the liquid-vapor surface tension of fluid) is built up in the deformed droplet due to the curvature difference. Consequently, an upward force is generated and gradually increases by this Laplace pressure difference. Due to the existence of the local hydrophilic site, there is a strong pinning force

preventing the detachment of the droplet from the valley of the groove and the droplet bottom is gradually stretched in the *z* direction. When the droplet top grows to a certain size, the upward force can overcome the significant pinning force and the deformed droplet can detach from the valley of the groove. After detaching from the valley of the groove, the increase rate in the number of condensed molecules (N) of the droplet dramatically decreases, as shown in Figure 5.4. This is because phase change is a nonspontaneous process, and the cooling effect mainly results from the local hydrophilic site. Once the droplet detaches from the local hydrophilic site, vapor molecules is difficult to condense to liquid molecules due to the high Gibbs free energy barrier for condensation on a superhydrophobic surface. Thus, we can conclude that the droplet growth mainly occurs before the droplet detaches from the local hydrophilic site and the final size of the self-jumping droplet is affected by the feature of the local hydrophilic site.

Relief from the pinning site, the droplet top expands more quickly and the whole droplet fast moves upward due to the significant Laplace pressure difference and subsequently self-jumps from the nanostructured surface (see Figure 5.2(a)). Correspondingly, the increases in z_c and R_t become more significant, especially after detaching from the groove valley (see Figure 5.2(b) and Figure 5.2(d)). From the energy point of view, due to the confinement of the groove, the condensed droplet is deformed, and its surface area is larger than the spherical droplet having the same volume, which leads to the existence of excess surface energy stored in the droplet. After the droplet detaches from the local pinning site, a big part of the excess surface energy converts into kinetic energy, which makes the droplet achieve self-jumping.

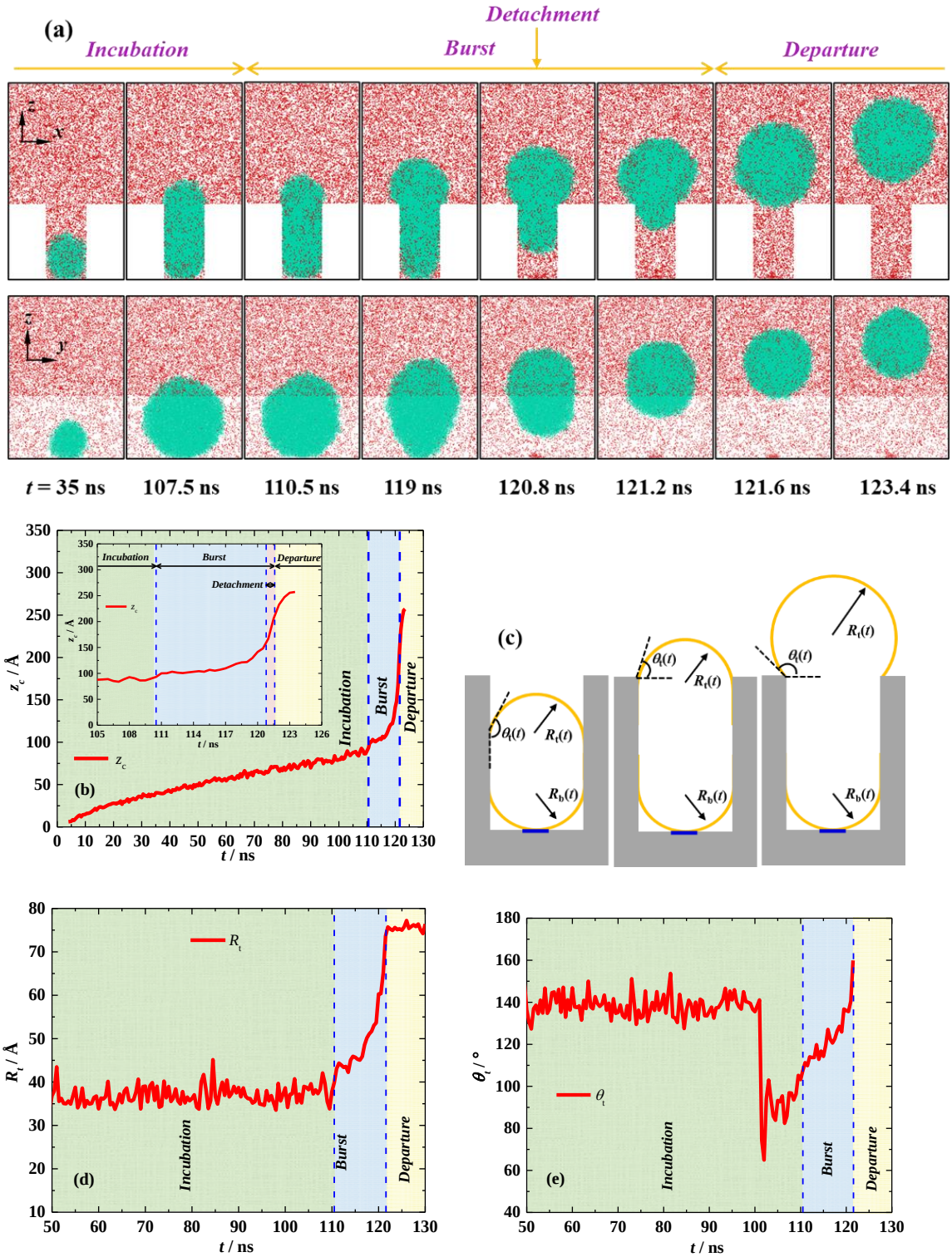

Figure 5.2: (a) Snapshots of the growth and self-jumping of single condensed droplet from the nanostructured surface with β = (0.1, 0.4) and A_i = 8a ×8a. Here only fluid atoms are shown, and the focused condensed droplet is marked in green, and the rest fluid atoms are in red. (b) Trajectory of the droplet centroid in the z direction (z_c). (c) Schematic of the droplet growth and burst process. (d) Radius of the curvature for the top interface (R_t) of the condensed droplet. (e) Contact angle for the top interface of the condensed droplet (θ).

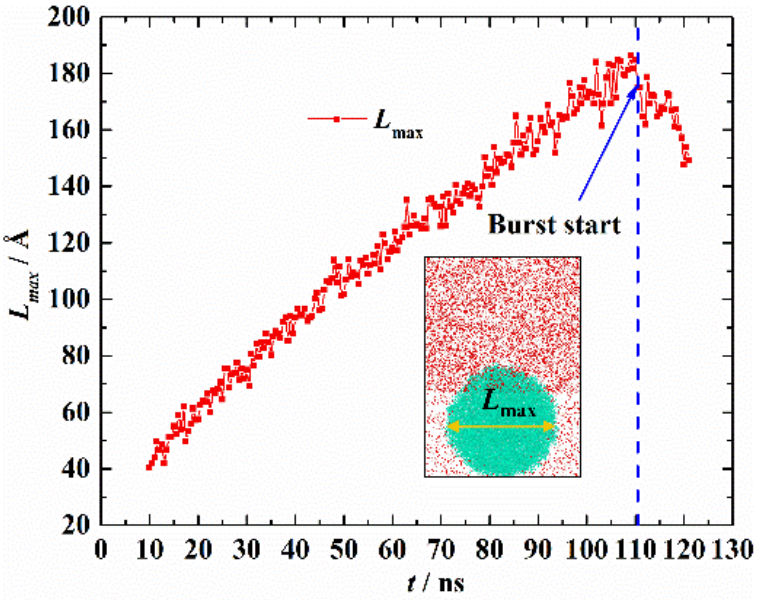

Figure 5.3: The widest length of the droplet (L_{max}) in the *y*-*z* plane parallel to the nano-groove.

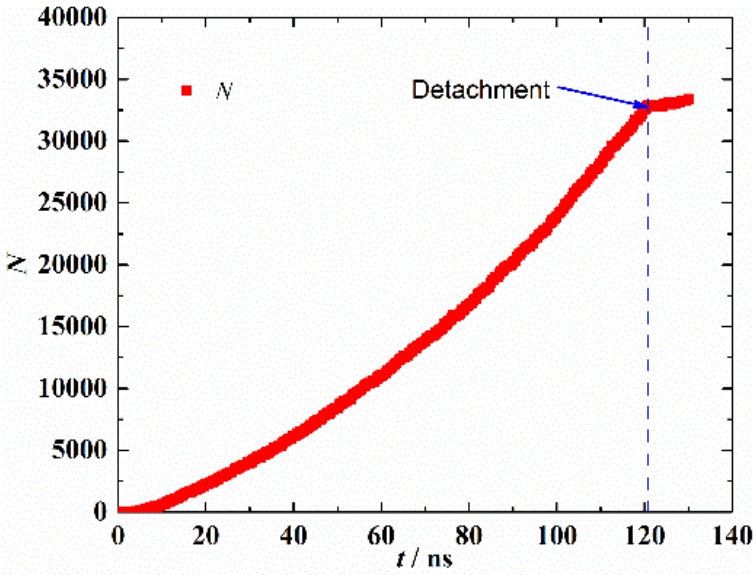

Figure 5.4: Number of condensed molecules (N) of the focused droplet.

5.2.2 Jumping velocity

To identify the self-jumping velocity, the velocity of the condensed droplet centroid in the *z*-direction (v_z) is collected and shown in Figure 5.5(a). It can be seen that v_z essentially

fluctuates around 0.005 Å·ps^{-1} before the droplet detaches from the groove valley. The fluctuation and much small nonzero v_z mainly results from the thermal motion of the droplet molecules and the occurrence of condensation [72]. Here, the droplet can be seen static before the droplet detachment from the groove valley occurring. This also shows that due to the pinning effect from the local hydrophilic site, the upward flow from the droplet bottom due to the Laplace pressure difference is accommodated by the static droplet top. The droplet top behaves like an inactive momentum sink and the excessive surface energy makes no direct contribution to upward kinetic energy. As the droplet top continuously grows larger and establishes a sufficient favorable Laplace pressure difference to overcome the pinning force, the deformed droplet detaches from the groove valley with v_d = 0.0381 Å·ps^{-1} (see Figure 5.5(a)). Following the droplet detachment from the groove valley, v_z continuously increases significantly as the large excessive surface energy partly converts to kinetic energy and the upward momentum appears after lacking impedance of the pinning force. The stretched droplet bottom quickly adjusts to circular shape, meanwhile the deformed droplet quickly moves upward and tries recovering to a spherical shape. Before the triple-phase contact line of the bottom interface arrives at the groove edges, the droplet bottom moves upward with nearly constant shape and at the same time the droplet top still expands continuously, which leads to the increase in Laplace pressure difference. As a result, v_z significantly increases (see Figure 5.5(a) and Figure 5.5(b)). As seen in Figure 5.5(b) and Figure 5.5(c), after the triple-phase contact line of the bottom interface arrives at the groove edges, the contact line of the bottom interface is pinned at the groove edges and the droplet bottom slowly moves upward, thus $R_b(t)$ increases and the curvature difference between the droplet bottom and top significantly decreases. In terms of energy conservation, during the pinning time at the groove edges, the deformation of the droplet is much small, and the stored excessive surface energy is small, so part of the kinetic energy turns to viscous

dissipation, which is significant in nanoscale. Therefore, it is observed that v_z starts decreasing before the droplet completely departs from the nanostructured surface. Finally, the condensed droplet departs the nanostructured surface with v_z = 0.0643 Å·ps^{-1}, which is regards as the jumping velocity (v_j) in our work. Note that the droplet-jumping velocity is defined as the instantaneous velocity when the droplet completely detaches from the nanostructured surface here, in other words, there is no contact between the droplet atoms and surface atoms. Therefore, the maximum velocity is not the jumping velocity in our work as there are still point contacts between the condensed droplet and the groove edges in the view from the *x*-*z* plane. After self-jumping from the nanostructured surface, the droplet has a spherical shape and there is no excessive surface energy stored in the droplet. Due to the viscous dissipation, v_z decreases gradually.

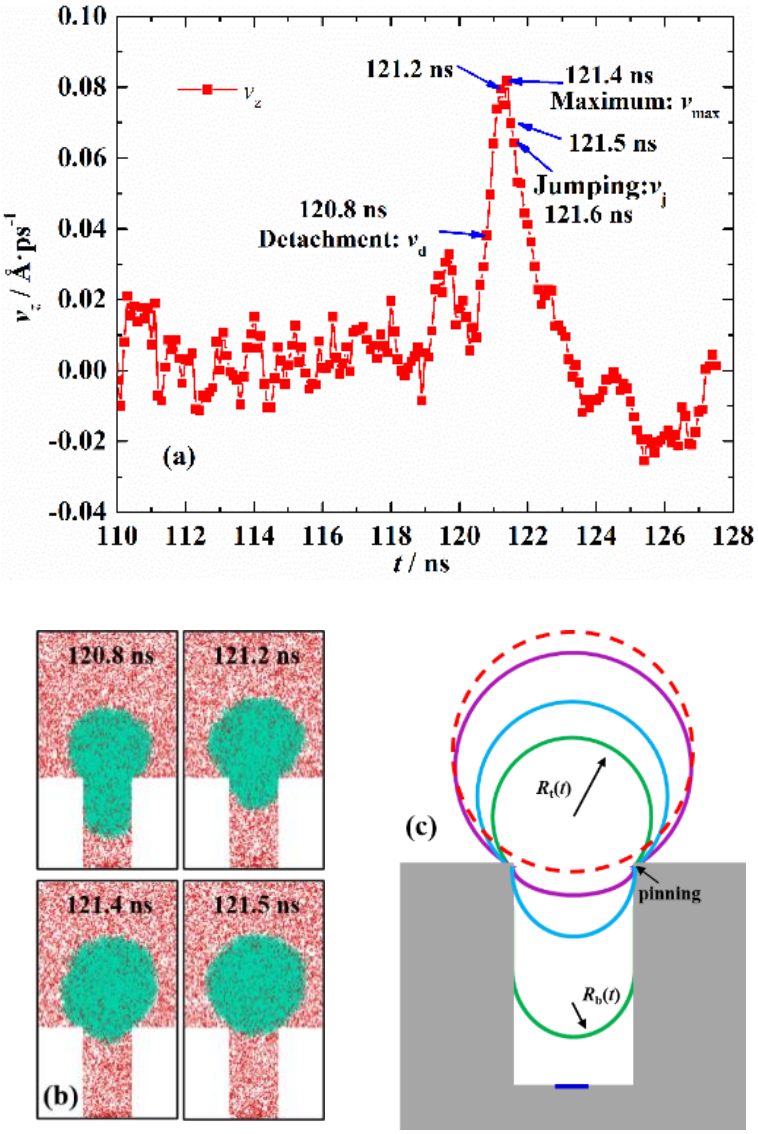

Figure 5.5: (a) Temporal evolution of velocity of the condensed droplet centroid in the *z* direction (v_z). (b) Snapshots of dynamical process about droplet moving in the groove after detaching from the groove valley. (c) Schematic showing droplet pinning phenomenon after detaching from the groove

5.2.3 Local pinning site

According to the abovementioned results, the local hydrophilic pinning site plays an important role in the growth and self-jumping of the droplet. Therefore, the effects of the surface wettability and size of the local pinning site on the whole condensation process is preliminary discussed here.

First, with a fixed pinning size of A_i = 12a ×12a, hydrophilic (β_i= 0.4) and superhydrophilic (β_i= 1.0) pinning sites are introduced. The condensation process is compared in Figure 5.6. Note that the time (t), the number of condensed molecules of the droplet (N) and the radius of the droplet top (R_t) in the x-z plane are also listed for different snapshots. The start of the burst stage, detachment point, and self-jumping point are specially marked with subscripts b, d and j, respectively. Generally, droplets evolve from pinning sites due to their high surface free energy. As the droplet top emerges from the groove, the droplet top starts freely expanding, but the droplet bottom is confined in the groove and gradually stretched. Finally, the droplets detach from the groove valley due to the large Laplace pressure difference in the droplets. Different from the droplet originating from the pinning site with β_i = 0.4, which departs the nanostructured surface by self-jumping, the droplet evolving from the pinning site with β_i= 1.0 does not depart from the nanostructured surface after detaching from the groove valley and stays on the groove top surface. According to our previous study [157], increasing β can promote the occurrence of condensation as it lowers the Gibbs free energy barrier. Thus, the droplet growth for the case with β_i = 1.0 is faster than that for the case with β_i = 0.4, and the burst and detachment of the droplet for β_i = 1.0 case start earlier than those for β_i = 0.4 case (see Figure 5.6). But simultaneously the pinning force from the pinning site also increases with the increase in β_i, which means that the droplet top needs to grow larger to have a higher Laplace pressure difference to make itself detach from the groove valley and meanwhile the droplet bottom is stretched more significantly. This is why N_d and R_{td} for β_i = 1.0 case are observed to be much larger than those for β_i = 0.4 (N_d = 37812 and R_{td} = 73.7 Å for β_i = 0.4 case; N_d = 75559 and R_{td} = 98.6 Å for β_i = 1.0 case). According to abovementioned results, the droplet growth nearly stops after detaching from the groove valley, which also proves in these cases. N is nearly constant after droplet detaching from the

groove valley and the little fluctuation is due to the thermal motion of fluid molecules. Thus, the final detached droplet on the surface with $\beta_i = 1.0$ is larger than that on the surface with $\beta_i = 0.4$ due to lower Gibbs free energy barrier for the former situation. Additionally, it can also be found that for larger β_i, the droplet bottom is stretched more dramatically before the droplet detaches from the groove valley; it takes significantly longer time to detach from the groove valley after the droplet starts bursting even though the droplet top grows faster for larger β_i. It lasts 17.0 ns from 82.5 to 99.5 ns for $\beta_i = 0.4$ case and 48.7 ns from 38.5 to 87.2 ns for $\beta_i = 0.1$ case. Due to the pinning effect, part of the droplet keeps pinned on the local hydrophilic site thus N drops after the droplet detachment occurs. For larger β_i, the pinning effect is stronger, and the droplet can even be pinched off as the droplet detachment occurs, then the obvious remainder of the droplet will contract and continue growing (see Figure 5.6(b)) from the pinning site. Because of the pinch-off and dramatic stretch of the droplet bottom, the detached droplet has small part squeezed in the groove for larger β_i case, which leads to less excessive free surface energy. Therefore, there is no sufficient kinetic energy converted for the droplet on the surface with larger β_i to support it self-jumping from the surface. Based on these findings, we can conclude that the droplet self-jumping relies on the confined portion of the detached droplet. The decrease of the confined portion reduces the excessive surface energy stored in the droplet and eventually makes droplet self-jumping from the structured surface fail.

For the effect of the size of local pinning site, with a fixed pinning β_i of 1.0, condensation on the nanostructured surface with pinning sites of $A_i = 4a \times 4a$ and $A_i = 12a \times 12a$ are compared in Figure 5.7. Comparing t_b, t_d, N_b and N_d, it can be seen that for pinning sites with $\beta_i = 1.0$, the increasing pinning size can also promote the droplet growth, but this results from increasing the effective heat transfer area where condensation can occur instead of lowering

Gibbs free energy barrier. Similar to increasing β_i, the total pinning force gets larger as the pinning size increases. Thus, as the pinning size increases, the droplet top needs to grow larger to make the droplet detach from the groove valley; the droplet bottom is stretched more significantly; the confined portion of the detached droplet decreases significantly, which also leads to the self-jumping fail.

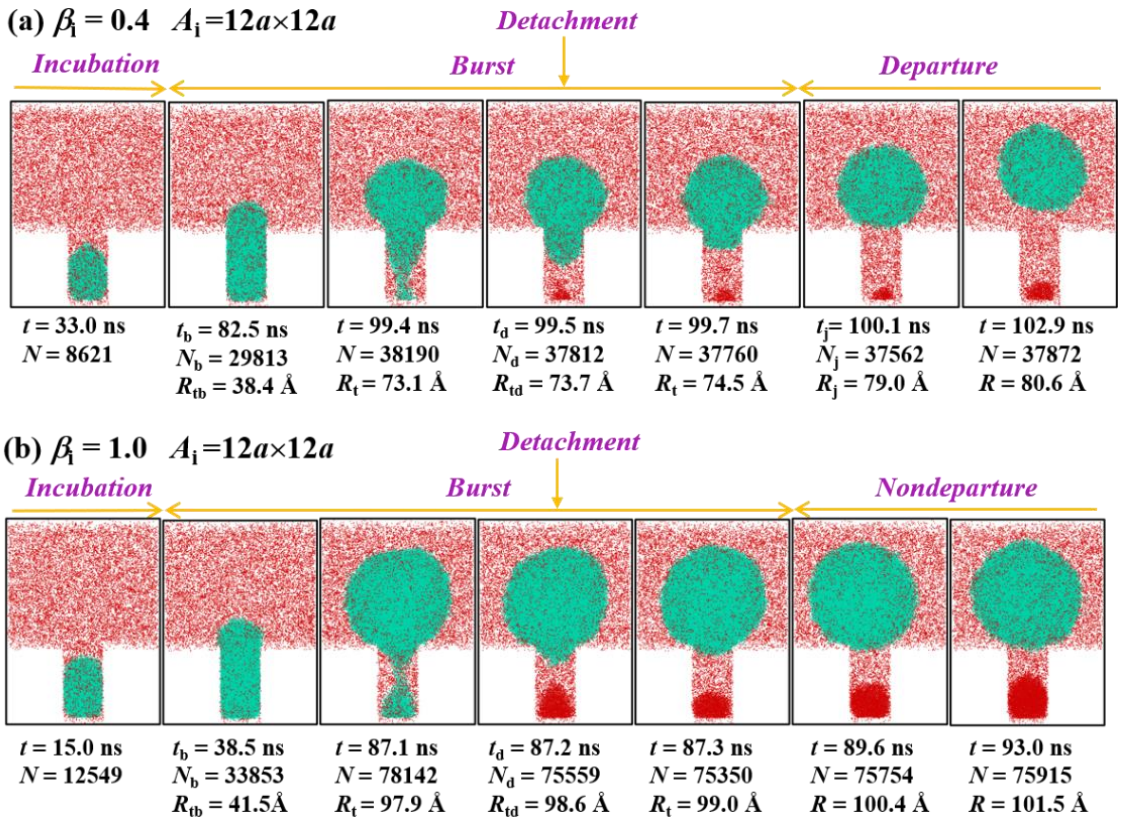

Figure 5.6: Condensation dynamics on nanostructured surface with local pinning site of (a) β_i = 0.4 and (b) β_i =1.0. The size of the pinning sites (A_i) is both 12a ×12a. t, N and R_t are time, number of condensed molecules for the droplet and the radius of the droplet top in the x-z plane, respectively. Subscripts b, d, and j represent the start of the burst stage, detachment point and self-jumping point, respectively.

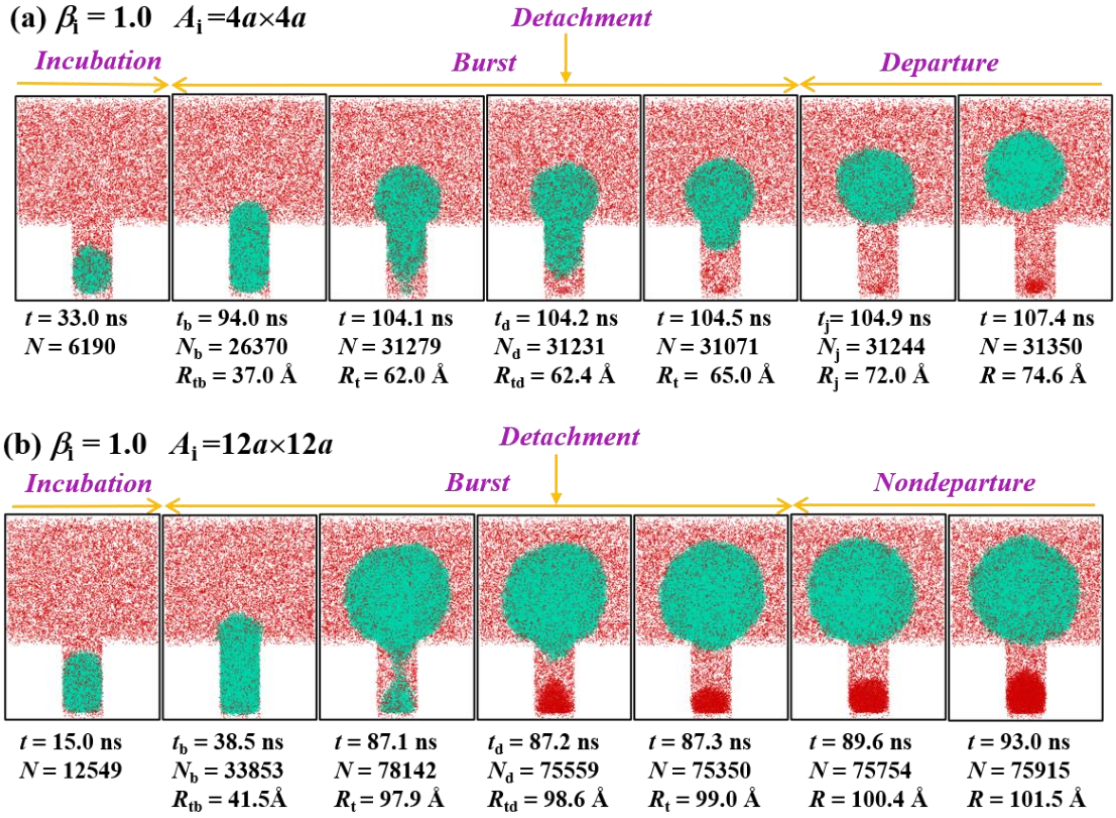

Figure 5.7: Condensation dynamics on nanostructured surface with local pinning site of (a) $A_i = 4a \times 4a$ and (b) $A_i = 12a \times 12a$, where is the A_i pinning size. The surface wettability of the pinning sites (β_i) is both 1.0. t, N and R_t are time, number of condensed molecules for the droplet and the radius of the droplet top in the x-z plane, respectively. Subscripts b, d, and j represent the start of the burst stage, detachment point and self-jumping point, respectively.

5.3 Conclusions

In this work, the growth and self-jumping dynamics of single condensed droplet on superhydrophobic nanostructured surface with a local hydrophilic pinning site have been investigated using MD simulations. The present work proves that self-jumping of condensed droplet driven by the Laplace-pressure is effective for nano-size droplet, which has not been previously observed by experiment. In our simulation, a single droplet first evolves from the hydrophilic pinning site and grows in the nanogroove. As its top emerges from the nanogroove, the droplet top gradually grows with pinned contact line at the groove edges

and freely expands both laterally and axially down the groove length, but its bottom is still confined in the nanogroove. This deformation leads to a curvature difference between the droplet top and bottom and a Laplace pressure difference is built up in the droplet. When the pressure difference reaches to a certain value, the upward force generated by the pressure difference can overcome the pinning force from the hydrophilic pinning site, which leads to the droplet detaching from the groove valley and finally self-jumping from the nanostructured surface. In this process, droplet growth mainly occurs in the time before the droplet detaching from the groove valley. Additionally, the effects of the surface wettability and size of the pinning site are also preliminarily discussed. Our results show that the hydrophilic pinning site with larger β_1 and size can promote the droplet growth but also make the self-jumping harder due to the increase in the total pinning force. The self-jumping of the condensed droplets lies on the confined portion of the detached droplets from the groove valley and its decrease will reduce the excessive surface energy stored in the droplet, which leads to less kinetic energy converted and it cannot support the droplet self-jumping from the nanostructured surface.

6 Stable and Efficient Nanofilm Pure Evaporation on Nanopillar Surfaces

In this chapter, MD method is employed to investigate how to maintain and enhance stable and efficient nanofilm evaporation without boiling. Moreover, to enrich the understanding of evaporation process, the dynamics of evaporation meniscus is also characterized from molecular insight. The onset and evolution of nanobubbles on nanopillar surfaces is captured and elucidated on the basis of energy analysis. Our work provides useful guidelines to understand and optimize the heat transfer performance of nanopillar wicks.

6.1 Computational methods

In this work, nanofilm evaporation on nanopillar surfaces was investigated using MD method. All the simulations are conducted using LAMMPS (Large-scale/molecular massively parallel simulator) software package [141]. A schematic of nanopillar array is depicted in Figure 6.1(a). The geometry parameters of a unit cell are noted in Figure 6.1(b). H and D are the height and diameter of the nanopillar, and P is the pitch between the pillars. δ is defined as the nanofilm thickness. Nanofilm evaporation on the surfaces of a unit cell is simulated and the MD model is shown in Figure 6.1(d). Correspondingly, nanofilm evaporation on a smooth surface, is also simulated (see Figure 6.1(e)). The overall size of all simulation boxes measures $l_x \times l_y \times l_z = P \times P \times 92\ a$, where a is the lattice constant (a = 0.392 nm). The nanopillars and solid substrate are constructed by Pt-like atoms arranged in the face-centered cubic (FCC) lattice, and the length of the unit cell is a. The solid substrate consists of three layers of Pt-like atoms and one extra layer of Pt-like atoms is fixed at the lowermost end to serve as a frame. In the x and y-directions, periodic boundary conditions

are used, while in the *z*-direction, the fixed boundary condition is employed, and the reflection boundary condition is also applied at the uppermost end. The embedded-atom method (EAM) potential is applied to model the interactions among solid atoms. The total energy of an atom *i* is described by:

$$\varphi_i\left(r_{ij}\right)=F_\alpha\left(\sum_{j\neq i}\rho_\beta\left(r_{ij}\right)\right)+\frac{1}{2}\sum_{j\neq i}\phi_{\alpha\beta}\left(r_{ij}\right) \tag{6-1}$$

where F is the embedding energy, and it is the energy to embed atom i into the background electron density. α and β are the element types of atoms i and j. ρ is the host electron density at atom i due to the remaining atoms of the system. φ is the pair potential interaction. The 12-6 Lennard-Jones (LJ) potential is employed to model the fluid-fluid atoms interaction and fluid-solid atoms interaction:

$$\varphi(r)=4\varepsilon\left[\left(\frac{\sigma}{r}\right)^{12}-\left(\frac{\sigma}{r}\right)^{6}\right] \tag{6-2}$$

where r is the intermolecular separation, ε and σ are the energy and length characteristic parameters, respectively. The potential function is truncated at the cut-off radius $r_c = 3.5\ \sigma_{ff}$, beyond which atom interactions are ignored. For the interaction between fluid atoms, ε_{ff} = 0.0104 eV and σ_{ff} = 3.40 Å. For the interaction between fluid-solid atoms, $\varepsilon_{fs} = 2\varepsilon_{ff}$ and $\sigma_{fs} = 0.91\sigma_{ff}$, which guarantees a strong surface wettability [156],[157], and benefits mass and heat transfer.

All the simulations are performed with a time step of 5 fs. The system is first equilibrated at T = 100 K for 7 ns using a Berendsen thermostat. Afterwards, fluid properties at equilibrium state were calculated. The NEMD (non-equilibrium molecular dynamics) simulation is initiated by increasing the solid temperature. Simultaneously, the thermostat added on fluid molecules is removed and only NVE ensemble is employed. Additionally, to save simulation cost and eliminate the effect of pressure increase due to evaporation, the vapor atoms

propagating into a region with thickness of 15*a* at the uppermost end are removed. In the present work, a parametric study of achieving stable and efficient evaporation without boiling was conducted by varying *P*, *D*, and *H* between 48-80, 8-32, and 24-50 *a* (*a* = 0.392 nm), respectively. Simulation cases are conveniently denoted by their typical geometry parameters. For example, the simulation case with *P* = 48*a*, *D* = 16*a*, and *H* = 36*a* is denoted as *P*48*D*16*H*36.

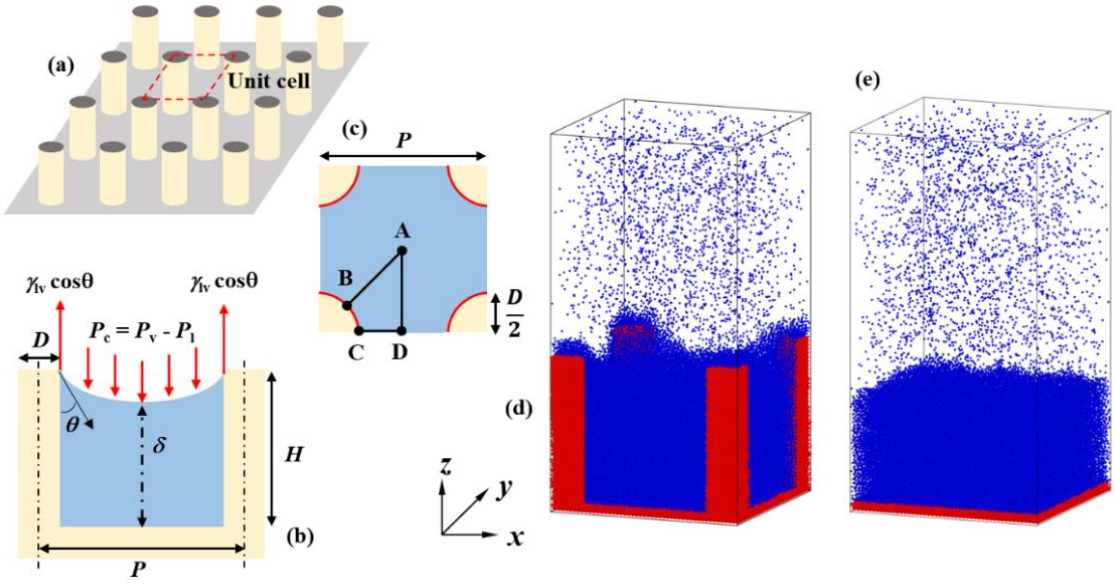

Figure 6.1: (a) Schematic of a typical nanopillar array. (b) Front view of a unit cell in a nanopillar array, where *P*, *D* and *H* represent the pitch between two pillars, the diameter and height of the pillar, respectively. θ and δ are the contact angle and nanofilm thickness. Force analysis on the meniscus in the vertical direction is also depicted, where γ_{lv} is liquid-vapor surface tension, and P_c, P_v, and P_l are capillary pressure, vapor pressure and liquid pressure, respectively. (c) Top view of a unit cell in a nanopillar array. The red lines represent the triple-phase contact line of the meniscus around nanopillars. (d) Schematic of the computational model for a unit cell in a nanopillar array. Solid atoms are in red, and fluid molecules are in blue. (e) Schematic of the computational model for nanofilm evaporation on a smooth surface.

6.2 Results and discussion

6.2.1 Capillary Pressure

After the simulation system evolves to equilibrium state, a meniscus is formed due to the existence of surface tension. Correspondingly, there is a pressure difference between the liquid and vapor side of the meniscus. This pressure difference is named as capillary pressure (P_c). For capillary-fed evaporator, accurately quantifying capillary pressure is quite important when we try to design or improve its performance. In MD simulation, the capillary pressure can be directly determined from the difference between vapor pressure (P_v) and liquid pressure (P_l): $P_c = P_v - P_l$. The MD results (P_c_MD) are shown in Figure 6.2. As can be seen, increasing P leads to the decrease in P_c when D and H are fixed. For fixed P and H, P_c can be increased by increasing D. Additionally, the capillary pressure in a nanopillar array can also be obtained by a force balance method [158]. In the equilibrium stage, there shows a steady meniscus, on which the downward force due to capillary pressure (F_c), namely the force due to the pressure difference between liquid and vapor sides of the meniscus, is opposed by the upward force due to the surface tension (F_γ) on the circumference of the nanopillars. Considering a unit cell (see Figure 6.1(b) and Figure 6.1(c)),

$$F_c = P_c A_{vertical} = P_c \left(P^2 - \frac{\pi D^2}{4} \right) \tag{6-3}$$

$$F_\gamma = \pi D \gamma_{lv} \cos\theta \tag{6-4}$$

where $A_{vertical}$ is the vertical projected area of the meniscus, γ_{lv} is the liquid-vapor surface tension and θ is the contact angle. At mechanical balance, $F_c = F_\gamma$, hence

$$P_c = \frac{4\gamma_{lv}\cos\theta}{D\left[\frac{4}{\pi}\left(\frac{P}{D}\right)^2 - 1\right]} \quad . \tag{6-5}$$

To obtain γ_{lv}, an EMD (equilibrium molecular dynamics) system is simulated (see A.1 in Appendix). For T = 100 K, γ_{lv} = 8.964 mN·m^{-1} and ρ_{sat} = 1285 kg·m^{-3}, where ρ_{sat} is saturated fluid density. To obtain θ, the liquid-vapor interface location, where the fluid density is half of the bulk liquid density, is extracted and these data are fitted to a two-term exponential function. Considering the non-axisymmetric nature of the meniscus around a nanopillar, θ in Eq. (4-5) is calculated by the average of θ in CD direction and AB direction (see Figure 6.1(c)). The capillary pressure determined from analytical solution (P_c_Eq.5) is compared with that from MD (P_c_MD) in Figure 6.2. As can be seen, they are in good agreement.

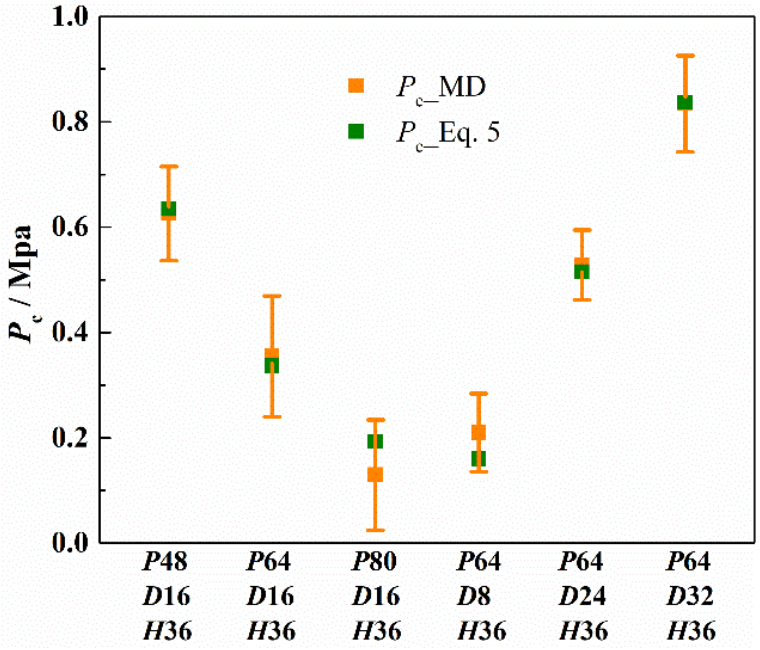

Figure 6.2: Comparison of capillary pressure determined from MD simulation (P_c_MD) and from analytical solution (P_c_Eq.5).

6.2.2 Dynamics of Evaporation Meniscus

When the solid temperature is increased, evaporation appears, and the meniscus develops. To examine the dynamic behavior of the evaporation meniscus, the liquid-vapor interface, where ρ = 0.009 Å^{-3}, is extracted from the density contour of fluid. To identify the location

of the vapor-liquid interface, the number of fluid neighbors of a fluid molecule within a certain distance ($1.5\sigma_{ff}$), named as the coordination number (CN), is collected for every fluid molecule. Afterwards the normalized histogram of the coordination number per fluid molecule during evaporation is analyzed. Figure 6.3 presents a typical distribution. It is seen that the low faction is always located between CN = 2 to 4. To further identify liquid and vapor molecules during evaporation, the fluid molecules with CN = 2, 3 and 4 are marked and observed by OVITO software (see Figure 6.4) [159]. In the vapor region, fluid molecules are observed with CN = 2 and 3 but are rarely or never observed with CN = 4. Therefore, the molecules with CN = 4 are identified as interface molecules. Correspondingly according to the definition of CN, the interface density is obtained: $\rho = 5/(4/3\cdot\pi\cdot(1.5\sigma_{ff})^3)$ Å^{-3}. Note that it should include the center molecule when calculating density, so the numerator is 5.

Figure 6.5 shows the evolution of evaporation meniscus for *P*48*D*16*H*36 at (a) ΔT = 10 K and (b) ΔT = 35 K. Note that two *z* axes are the position of the nanopillar surface ($x = \pm 62.72$ Å). Initially, the liquid-vapor interface moves upward due to thermal expansion. This is less apparent when ΔT is smaller. Then the curvature of the interface near the nanopillar surface increases gradually during evaporation, correspondingly the contact angle decreases. In our simulations, because a strong fluid-solid bonding strength parameter is used (i.e., perfectly wetting fluid is simulated), the interface is still pinned at the top of the nanopillars even when the nanofilm approaches the substrate surface. Additionally, it is also seen that the curvature of meniscus close to the nanopillars changes dramatically while the meniscus is almost flat in the centre region. This is more apparent for larger ΔT.

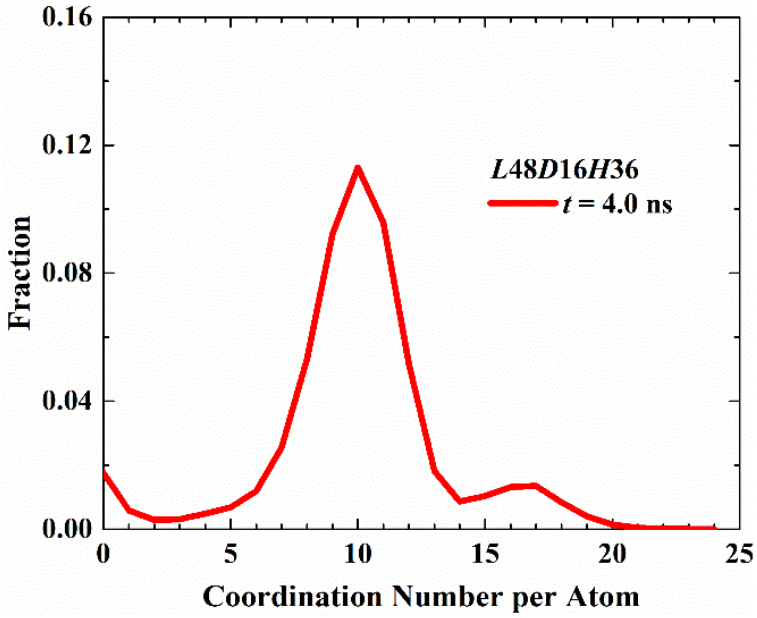

Figure 6.3: The normalized histogram of the coordination number per fluid molecule for *P*48*D*16*H*36 when t = 4.0 ns.

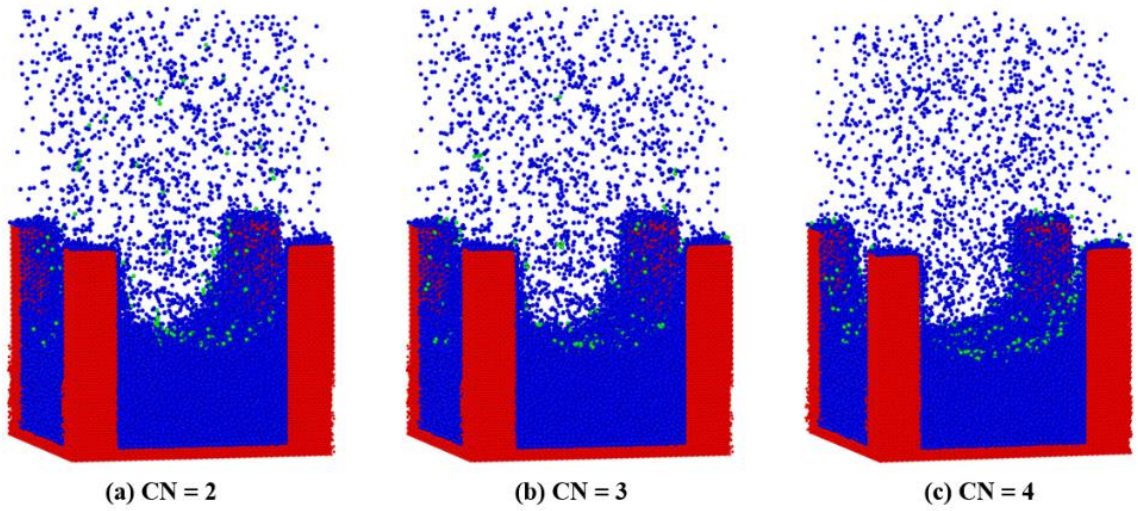

Figure 6.4: Atoms with different coordination number (CN) are marked in green in the snapshot for *L*48*D*16*H*36 when t = 4.0 ns. (a)CN = 2; (b)CN = 3; (c) CN=4.

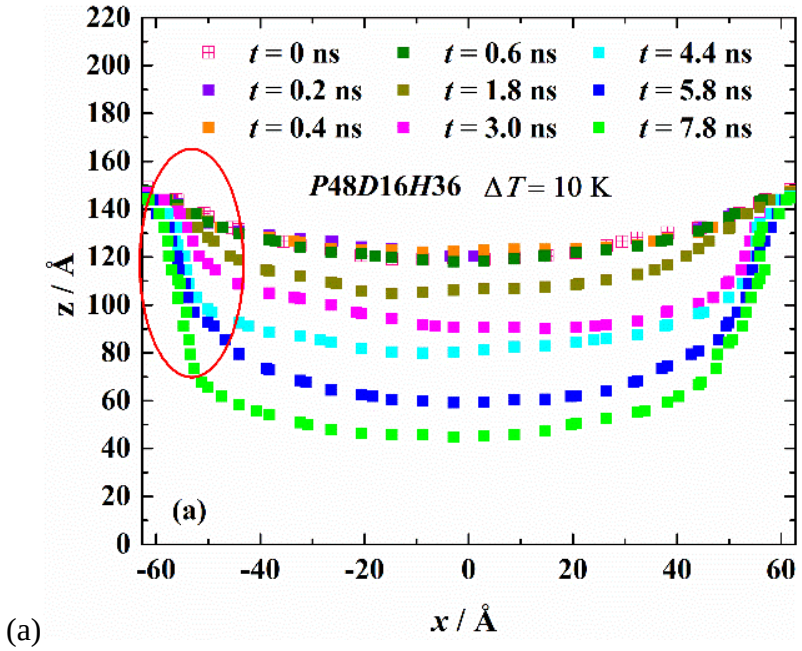

(a)

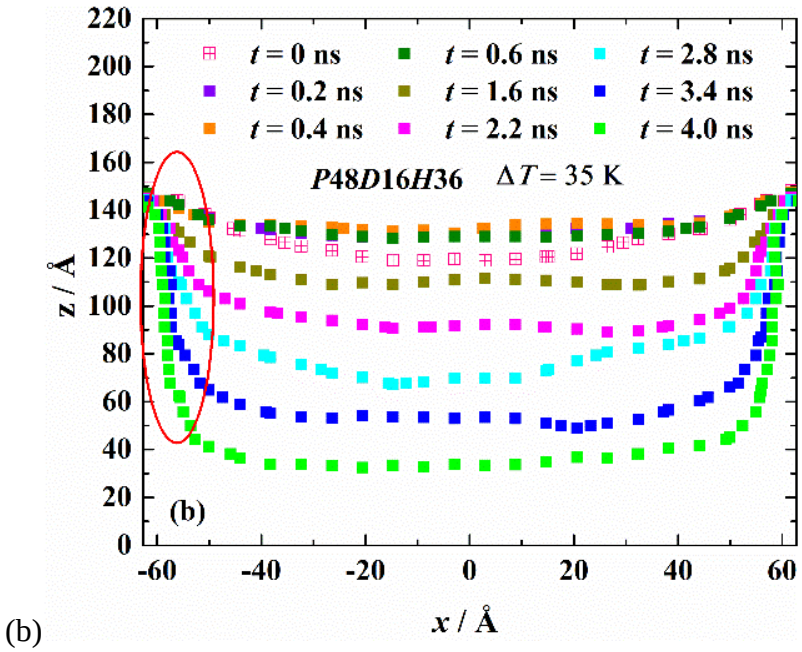

(b)

Figure 6.5: Evaporation meniscus (liquid-vapor interface) shapes for *P*48*D*16*H*36 at (a) ΔT = 10 K and (b) ΔT = 35 K.

6.2.3 Onset and Evolution of Nanobubbles

In some applications, pure evaporation in the absence of boiling is preferred due to its stable nature compared with the chaotic boiling process and the boiling limit. Thus, locating the

onset of boiling is necessary. We increase ΔT to 40 K and try observing the onset and evolution of nanobubbles under *P*48*D*16*H*36 case. Figure 6.6 shows the density contour of fluid at different time. To clearly monitor the onset and evolution of nanobubbles, the fluid density below 0.009 $Å^{-3}$ (the liquid-vapor interface density and see the Dynamics of Evaporation Meniscus section) is cut-off. As can be seen in Figure 6.6, nanobubbles first appears around the bottom of nanopillars. Then bubbles in the corner coalescence and expand towards the center of the cell. Due to strong solid-fluid wettability, nanobubbles do not originate from the solid surface and there is a non-evaporation ultrathin film covering in the solid surface, which is also observed in other studies [160],[161]. To further understand this, the potential energy contour of fluid is calculated (see Figure 6.7). From energy point of view [162],[163], low potential energy means large energy barrier for evaporation or boiling and only when liquid overcomes their potential barrier can the bubble nucleus form. As can be seen in Figure 6.7, fluid close to the solid surface owes much low potential energy, which strongly impedes the evaporation and boiling. This is why nanobubbles do not originate from the solid surface. Before the fluid is heated (t = 0 ns), the potential energy of fluid uniformly distributes in the bulk region. Once the solid temperature is increased, fluid absorbs thermal energy from the heating solid, and some of the thermal energy is converted to the potential energy, which leads to the increase in potential energy of fluid. The potential energy of fluid close to the solid surface first increases, then this increase propagates towards the center (see t = 0.2 ns and t = 0.4 ns in Figure 6.7). It can also be found that the potential energy of fluid around the nanopillars corner increases more quickly, which eventually leads to nanobubbles first appearing there when they overcome the energy barrier. The reason is because the fluid around the nanopillars corner can absorb more thermal energy not only from substrate but also from nanopillars compared with fluid in other regions. In summary, nanobubbles appear

when fluid overcomes its potential energy barrier, and they prefer to appear around nanopillars corner as the potential energy of fluid increases the most quickly there.

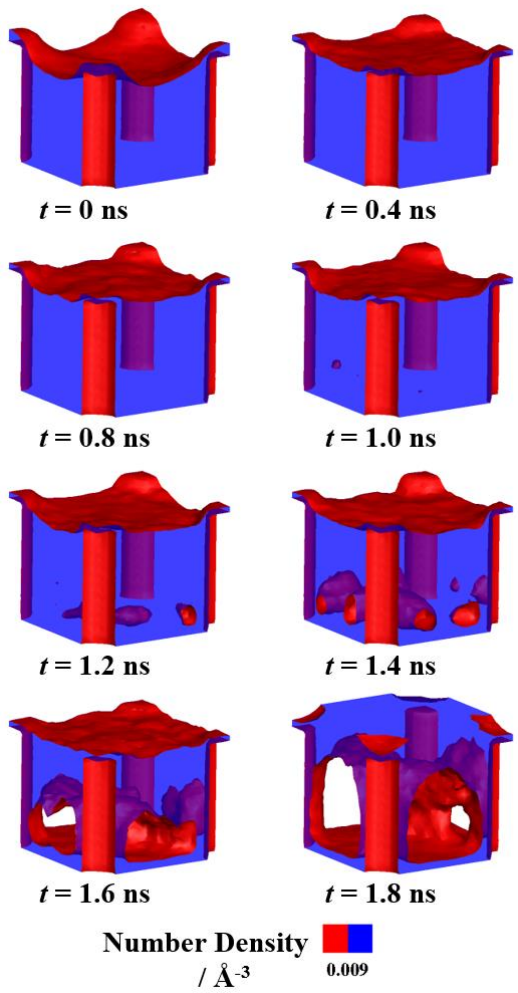

Figure 6.6: Snapshots of fluid density contour for *P*48*D*16*H*36 at ΔT = 40 K. Density below 0.009 Å^{-3} is cut-off.

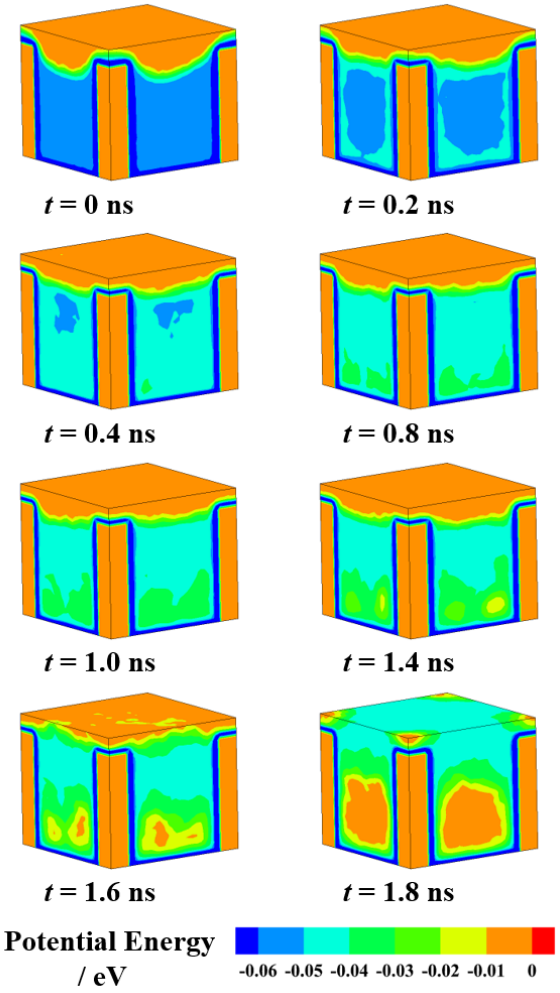

Figure 6.7: Snapshots of potential energy contour of fluid for *P*48*D*16*H*36 at ΔT = 40 K.

6.2.4 Nanostructure Design for Stable and Efficient Pure Evaporation

The effect of structure geometry on evaporation and boiling is systematically investigated in the present study. This helps tailor performance of wick-based evaporators. As mentioned before, to achieve stable heat transfer, evaporation without boiling is preferred. Figure 6.8 to Figure 6.10 present the fluid density contour and potential energy contour under different

cases. By varying P, D and H, respectively, we found that for fixed ΔT, decreasing P (see Figure 6.8) and increasing D (see Figure 6.9) and H (see Figure 6.10), individually, raise the possibility of boiling. From the potential energy contour, we found that after decreasing P (see Figure 6.8) and increasing D (see Figure 6.9) and H (see Figure 6.10), individually, the increase in the potential energy of fluid around nanopillars corner becomes faster and the energy is easily accumulated to overcome the energy barrier of forming nanobubble. Thus, nanobubbles appears in those cases.

Figure 6.11 to Figure 6.13 plot evaporation mass flux ($\dot{m}''$) as a function of nanofilm thickness (δ) on nanopillar surfaces with different geometrical parameters and that on smooth surface. To obtain $\dot{m}''$, the coordination number and position data of each fluid molecule are collected every 4×10^4 time steps. Molecules with CN $\geq$ 4 are identified as fluid molecules (see section 6.2.2). $\dot{m}''$ is calculated as the time rate of change of the number of liquid molecules in the unit cell using a central difference formula. Note that the evaporation area to calculate $\dot{m}''$ is adopted $P\times P$, the total cross area of the simulated unit cell. As can be seen in these figures, generally, $\dot{m}''$ increases as decreasing P and H and increasing D; $\dot{m}''$ first increases with the decrease in δ, which results from the decrease in the conduction thermal resistance of liquid with δ decreasing. But with P decreasing or D increasing, heating area increases so there quickly behaves steady $\dot{m}''$ (e.g., $P48D16H36$ in Figure 6.11 and $P64H36D32$ in Figure 6.12). Additionally, there exists the saturation of the increase in $\dot{m}''$ when increasing D ($D24$ and $D32$ in Figure 6.12). Combining the results about the effect of structure geometry on boiling, we need trade-offs to decide D, L and H when designing a wick-based evaporator for stable pure evaporation.

When the film thickness decreases to a threshold, $\dot{m}''$ for all cases starts dropping dramatically. According to previous research [164]-[166], it means that disjoining pressure

($P_d = B/\delta^3$, where B is the dispersion constant) starts showing effect, and it increases with decreasing δ. P_d was proposed for treating the effect of the solid-fluid force interaction in thin liquid film and it shows a strong suppression effect on evaporation. In our simulations, the film thickness where P_d starts showing effect is the same for both smooth and nanopillar surfaces and it is around 20 Å. To maintain efficient evaporation, δ should be forced larger than this threshold. Additionally, there also shows that the $\dot{m}''$ of the smooth surface surpasses those of nanopillar surfaces when δ is smaller than a certain value (indicated by grey arrows). This is because although adopting nanopillars in a smooth surface enhances evaporation due to the increase in heating area, the evaporation flux simultaneously is suppressed due to the decrease in the volume of supplied fluid and the existence of capillary pressure [165]. As δ decreases, the suppression effects on $\dot{m}''$ is gradually more significant than the enhancement effect. Thus, to enhance pure evaporation on nanopillar surface compared with that on smooth surface, the nanofilm thickness should be maintained beyond the value where the suppression effects on $\dot{m}''$ due to the decrease in the volume of supplied liquid and the existence of capillary pressure dominates during evaporation. This also explains that why in Figure 6.12, for fixed P and H, when D increases to 24a, the increase in $\dot{m}''$ saturates.

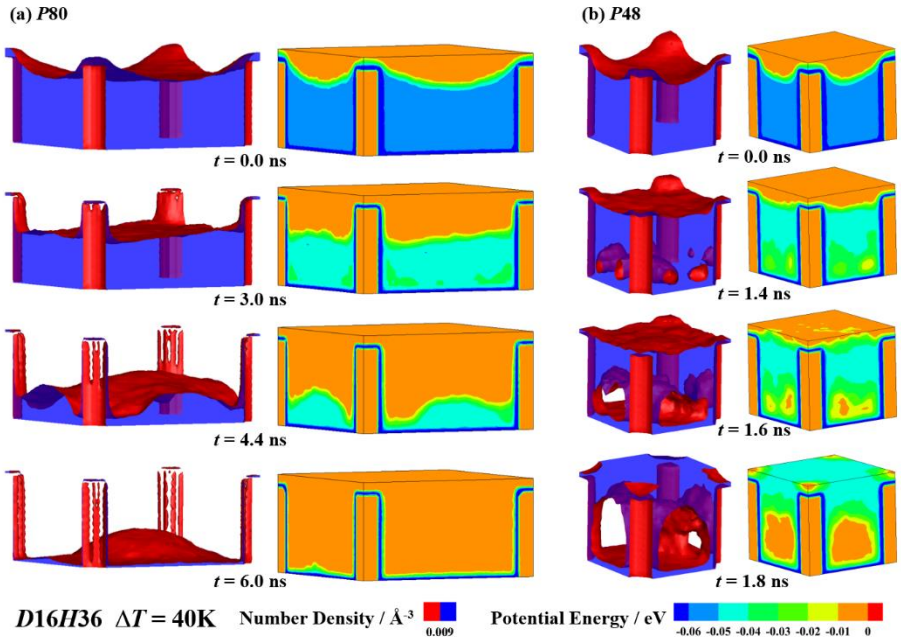

Figure 6.8: Snapshots of fluid density contour and potential energy contour for *D*16*H*36 with different pitch between nanopillars at ΔT = 40K (a) *P*80; (b) *P*48. Density below 0.009 $Å^{-3}$ is cut-off.

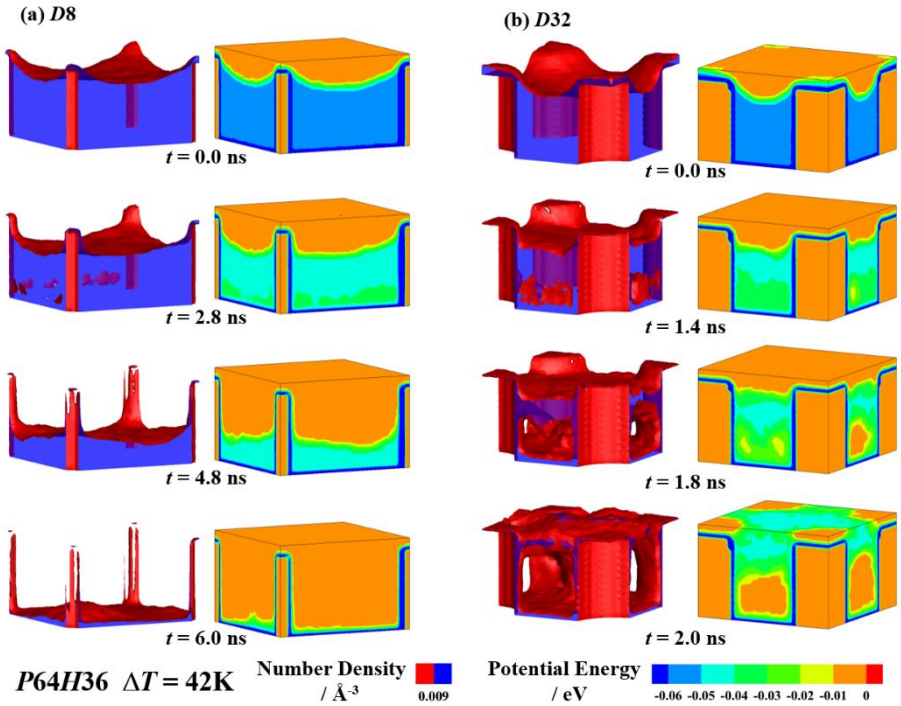

Figure 6.9: Snapshots of fluid density contour and potential energy contour for *P*64*H*36 with different diameter of nanopillars at ΔT = 42K (a) *D*8; (b) *D*32. Density below 0.009 $Å^{-3}$ is cut-off.

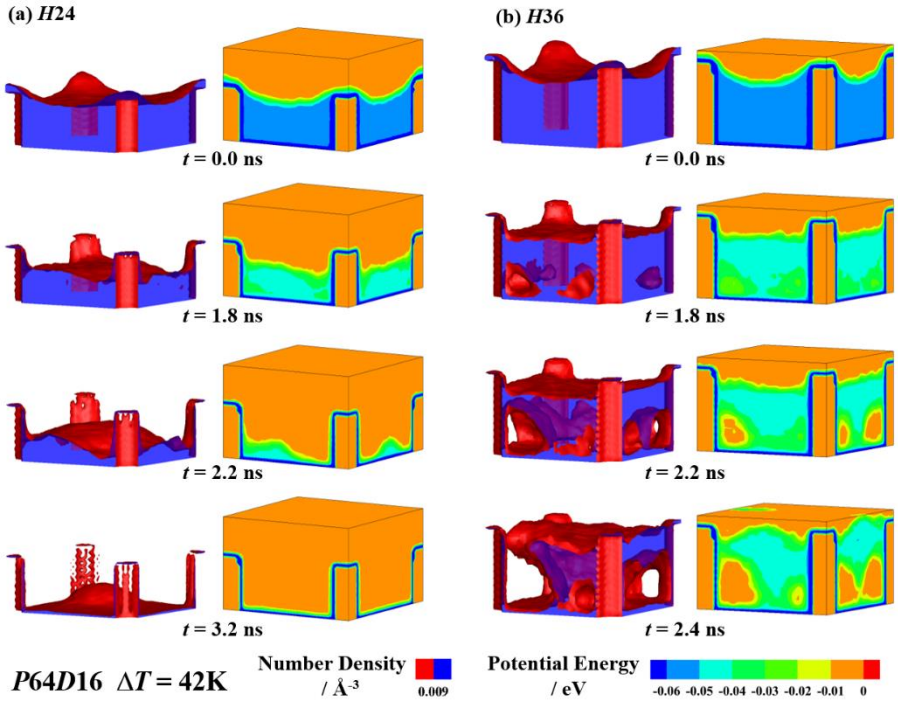

Figure 6.10: Snapshots of fluid density contour and potential energy contour for *P*64*D*16 with different height of nanopillars at ΔT = 42K (a) *H*24; (b) *H*36. Density below 0.009 $Å^{-3}$ is cut-off.

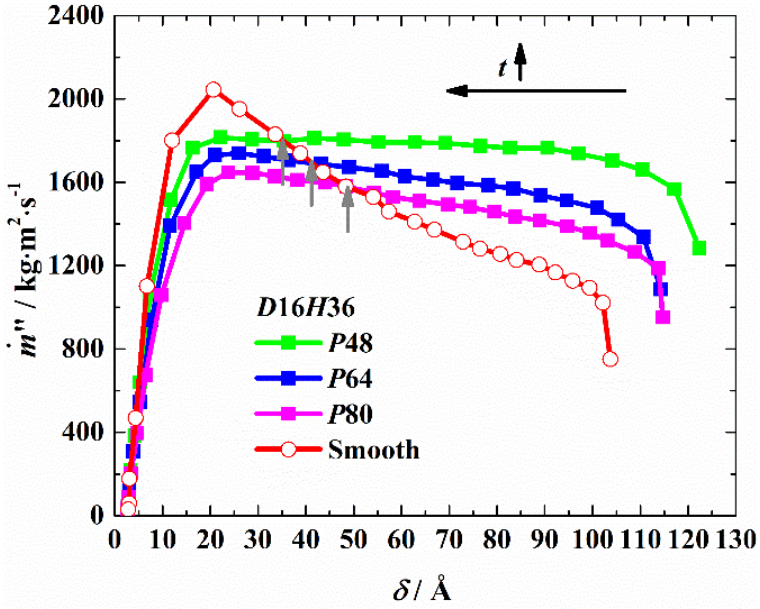

Figure 6.11: Evaporation mass flux ($\dot{m}''$) vs nanofilm thickness (δ) for fixed *D* and *H* cases. δ decreases as *t* (evaporation time) increases.

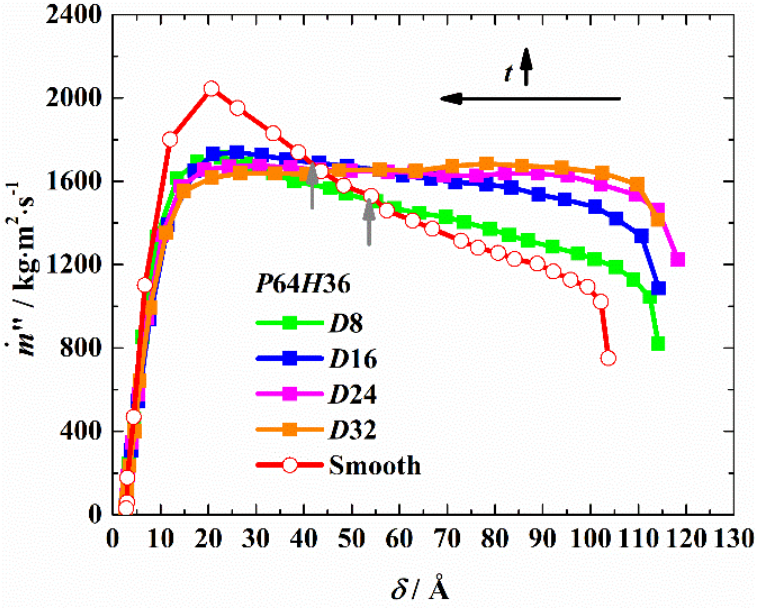

Figure 6.12: Evaporation mass flux ($\dot{m}''$) vs nanofilm thickness (δ) for fixed P and H cases. δ decreases as t (evaporation time) increases.

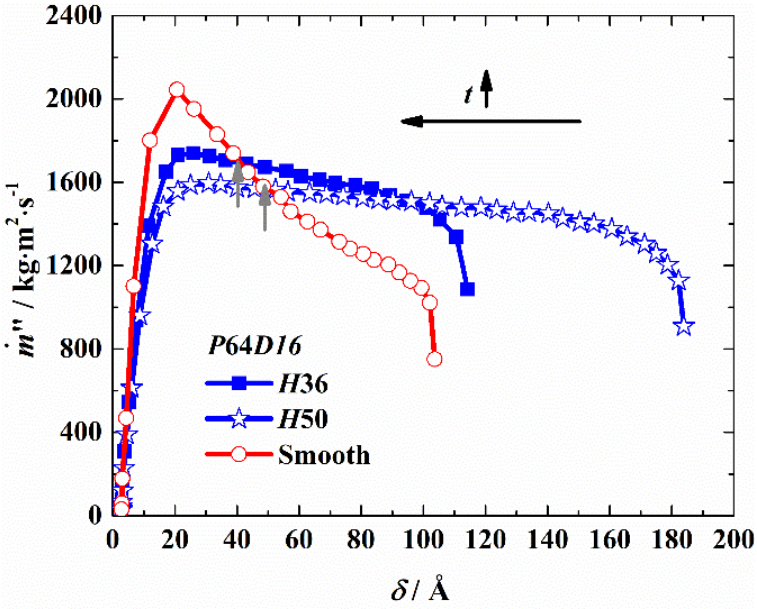

Figure 6.13: Evaporation mass flux ($\dot{m}''$) vs nanofilm thickness (δ) for fixed P and D cases. δ decreases as t (evaporation time) increases.

6.3 Conclusions

In this work, characteristics of evaporation and how to maintain and enhance nanofilm evaporation without boiling on nanopillar surface were investigated using MD method.

For the perfectly wetting fluid, the meniscus can be still pinned at the top of the nanopillars even when the nanofilm is quite close to the surface of substrate and the curvature of the meniscus near nanopillars varies dramatically during evaporation. On nanopillar surface, nanobubbles prefer to first develop around nanopillars corner due to the quick increase in the potential energy of fluid there, then coalesce and expand toward the unit center.

Based on our parametric study, the evaporation mass flux $\dot{m}''$ can be increased by decreasing P and increasing D but these also raise the risk of boiling. However, decreasing H can both benefit evaporation and suppress boiling. Therefore, we should have a trade-off between enhancing evaporation and achieving stable evaporation without boiling when selecting P, D and H.

During evaporation, to maintain efficient evaporation and avoid the suppression effect of disjoining pressure on evaporation, nanofilm thickness should be forced beyond a threshold where disjoining pressure starts showing effect. In this work, the threshold value is about 20 **Å**. To enhance the evaporation on nanopillar surface against smooth surface, the film thickness should be maintained larger than the value where the suppression effect on evaporation due to the decrease in the volume of supplied fluid and the existence of capillary pressure behaves more significant than the enhancement effect on evaporation due to the increase in the heating area.

7 Generation and Evolution of Nanobubbles on Heated Nanoparticles

Nanobubbles are generated around nanoparticles and interfacial properties play important roles in the nanoscale heat transfer. Previous studies, however, have seldomly considered the role of nanoparticle characteristics in the generation and evolution of nanobubbles. Additionally, heating-up characteristic of nanoparticles has yet seldom been focused on. In this chapter, the effects of two typical surface characteristics of nanoparticles (super-hydrophilic and super-hydrophobic), as well as the heating intensity, are especially focused on. The inception and dynamics of nanobubbles are investigated and the heating-up characteristics of nanoparticles is also analyzed. Our work helps further understand the generation and evolution of nanobubble and potentially offers a new insight for nanobubble manipulation.

7.1 Computational methods

The computational system, as shown in Figure 7.1, consists of a gold-like nanoparticle (GNP) and the argon-like fluid around it. The GNP is fixed at the center of the simulation box. It is obtained from a spherical cut of a face-centered cubic (FCC) lattice and the length of the unit cell, a, is 4.08 Å. Note that the radical dimension is measured from the center of the simulation box. The radius of the GNP, R_{GNP}, is $7a$. The heat sink refers to the region outside a spherical surface at a distance $26a$ (R_{sink}) from the center of the simulation box, where the fluid is thermostat at a constant temperature. All the simulations are conducted using LAMMPS (large-scale atomic/molecular massively parallel simulator) software package [141]. Periodic boundary conditions are applied in the x, y and z directions. The

embedded-atom method (EAM) potential is applied to the interactions among gold atoms. The total energy of an atom *i* is described by:

$$\varphi_i\left(r_{ij}\right)=F_\alpha\left(\sum_{j\neq i}\rho_\gamma\left(r_{ij}\right)\right)+\frac{1}{2}\sum_{j\neq i}\phi_{\alpha\gamma}\left(r_{ij}\right) \tag{7-1}$$

where F is the embedding energy, and it is the energy to embed atom i into the background electron density. α and γ are the element types of atoms i and j. ρ is the host electron density at atom i due to the remaining atoms of the system, ϕ is the pair potential interaction. For fluid-fluid interaction, the 12-6 L-J potential function is employed:

$$\varphi(r)=4\varepsilon\left[\left(\frac{\sigma}{r}\right)^{12}-\left(\frac{\sigma}{r}\right)^{6}\right] \tag{7-2}$$

where r is the intermolecular separation, ε and σ are the energy and length characteristic parameters, respectively. The potential function is truncated at the cut-off radius $r_c = 3.5\sigma$, beyond which molecular interactions are ignored. $\varepsilon_{\text{Ar-Ar}} = 0.01040$ eV and $\sigma_{\text{Ar-Ar}} = 3.405$ Å are used [167]. The interaction between the GNP atoms and fluid is also governed by Eq. (7-2) but with different energy and length parameters i.e., $\varepsilon_{\text{Ar-Au}} = \beta\varepsilon_{\text{Ar-Ar}}$ and $\sigma_{\text{Ar-Au}} = 0.91\sigma_{\text{Ar-Ar}}$, where β is the fluid-GNP bonding strength parameter indicating the surface free energy or equivalently the surface wettability. Normally, lower surface free energy corresponds weaker surface wettability.

All the simulations are performed in two stages with a time step of 2 fs. In the equilibrium stage, the system is equilibrated at a constant pressure $P = 5$ atm and a constant temperature $T = 101$ K for 2.8 ns using a Berendsen barostat and thermostat. In the heating stage, the GNP is heated with a constant heating intensity (Q). The fluid in the heat sink region is still maintained at 101 K by Berendsen thermostat while for the rest of the fluid, the thermostat is removed and only NVE ensemble is employed. In the heating stage, the Berendsen barostat is still used to keep the system pressure at 5 atm. The heating intensity Q varies from 0.5 to

3.0 eV·ps^{-1}. β = 0.2 and 2 are chosen to describe super-hydrophobic and super-hydrophilic GNPs, respectively.

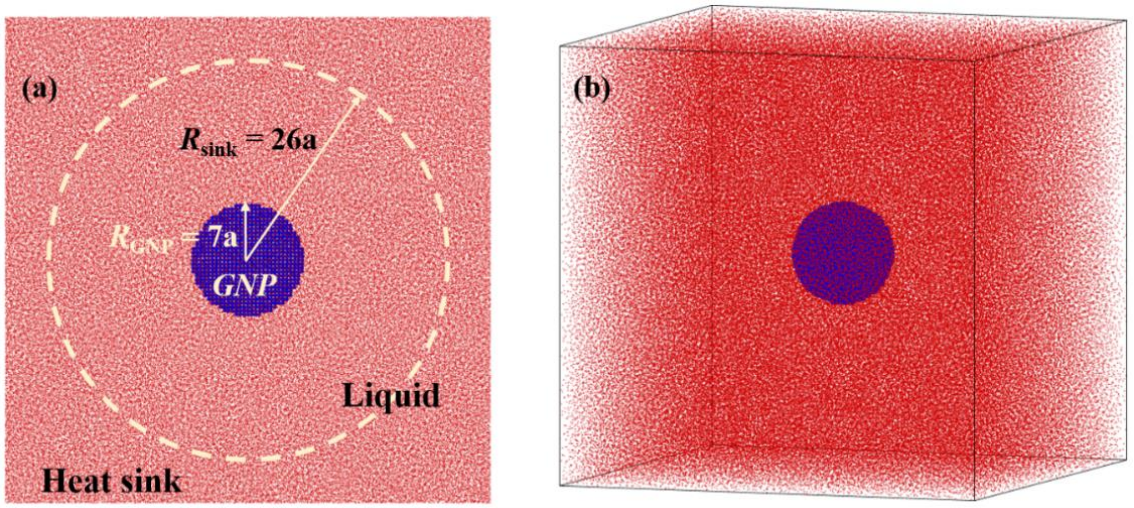

Figure 7.1: Schematic of computational system. (a) Cross-sectional view; (b) three-dimensional side view. A gold nanoparticle (GNP) with radius R_{GNP} of 7a is located at the center of the simulation box. The radical dimension is measured from the center of the simulation box. The GNP is colored in blue, and the fluid molecules are in red. The heat sink is the region outside a spherical surface with a radius R_{sink} of 26a, dotted line.

7.2 Results and discussion

7.2.1 Nanobubble dynamics

In the present work, the GNPs are continuously heated with a constant heating intensity, which may lead to the melting of the GNPs. Due to the large specific surface area, the melting point (T_m) of a nanoparticle is considerably depressed and distinct from bulk gold. The T_m of bulk gold is 1337 K, while early melting would occur for a GNP with lower dimension [168]-[170]. Following earlier MD studies [171],[172], the potential energy per atom and the corresponding temperature of GNPs (T_{GNP}) are recorded to characterize the T_m of the GNPs. It is found that the T_m of GNPs is independent of surface wettability and its

value is obtained to be ca. 1000 K for both GNPs with β = 0.2 and 2, respectively (see A.2 in the Appendix).

The radius of the nanobubble (R_b) is determined based on the spatial density profile of fluid and the location of vapor-liquid interface. In this work, the interface location is defined where the fluid density (ρ_i) is half of the bulk fluid density (ρ_f) [138]. We assume that the nanobubble spherically envelops the GNPs. When the fluid density appears below ρ_i in the fluid region, we consider that a nanobubble is formed. Based on the time evolution of fluid density profiles, the typical generation and evolution of nanobubbles for GNPs with different surface wettabilities are followed (see Figure 7.2), where the heating intensity Q = 1.4 eV·ps^{-1}. The green dash line represents the surface position of GNPs (R_{GNP} = 28.56 Å). Note that the nanobubble growth is recorded until the temperature of GNPs (T_{GNP}) reaches the melting point. According to the evolution of T_{GNP}, the periods of time reaching the melting point for GNPs with β = 2 and 0.2 are 7.5 ns and 2.7 ns, respectively, which will be discussed in detail later in section7.3.2. In order to analyze the evolution of R_b, the density profiles and snapshots of the simulation results at some typical times are depicted in Figure 7.3 for (a) β = 0.2 and (b) β = 2. Note that the cross-sectional views are adopted to clearly demonstrate the evolution of nanobubble. It is seen from Figure 7.3(a) that before the GNP is heated (t = 0 ns), there already exists an ultrathin low-density layer (< ρ_i) with a thickness of about 2 Å adjacent to the GNP surface resulting from weak attraction between the GNP and fluid. Therefore, R_b for β = 0.2 does not initiate from R_{GNP}. Additionally, it is seen that R_b for β = 0.2 starts to increase immediately after the GNP is heated, indicating that there is no delay for nanobubble generation. The R_b for β = 0.2 ultimately reaches 39 Å ($R_{b,max}$) when T_{GNP} increases to T_m. On the contrary, a delay in nanobubble generation is observed for β = 2 (see Figure 7.3(b)). After a delay time t_d (= 2.3 ns), a giant nanobubble abruptly appears and then grows gradually. Finally, R_b for β = 2 grows to 49 Å ($R_{b,max}$) when T_{GNP} increases to T_m,

which is larger than that for β = 0.2 ($R_{b,max}$ = 39 Å). From Figure 7.3(b), a large density value is seen around the GNP surface, where the GNP surface adsorbs a dense layer of fluid due to the strong attraction between the GNP and fluid. This contributes an effective heat transfer between the GNP and fluid and leads to a delay of nanobubble generation. When t = 2.3 ns, a vapor layer appears where the fluid density drops lower than ρ_i. Interestingly, this vapor layer is located at a distance of about 10 Å from the GNP surface instead of on the GNP surface. This explains why a giant nanobubble forms at the initial time in Figure 7.2 for β = 2. Based on the above analysis, we conclude that although $R_{b,max}$ for β = 0.2 is smaller than that for β = 2, the GNP with β = 0.2 could make nanobubble generate faster than that with β = 2 under the same heating intensity. For Q = 1.4 eV·ps^{-1}, there is already an apparent nanobubble for the GNP with β = 0.2 before the nanobubble appears around the GNP with β = 2.

Figure 7.4 shows the temperature profiles of the fluid and GNPs at some typical times for (a) β = 0.2 and (b) β = 2, respectively. Conspicuously, for both β = 2 and 0.2, the temperature gradients in the liquid increase with increasing T_{GNP} and become steeper as the nanobubbles grow. Compared with the case of β = 0.2, more heat is transferred to the fluid bulk and the fluid temperature is obviously much higher in the case of β = 2. Due to the strong surface wettability of β = 2, the temperature difference between the GNP and fluid adjacent to the GNP surface is small in the initial period of time and it gradually increases after the nanobubble forms. Differently, the temperature difference between the GNP and fluid adjacent to the GNP surface is significantly large for β = 0.2 from the very beginning and it increases dramatically as the GNP is heated. Therefore, we could conclude that the large temperature difference between the GNP and fluid adjacent to the GNP surface leads to immediate generation of nanobubble.

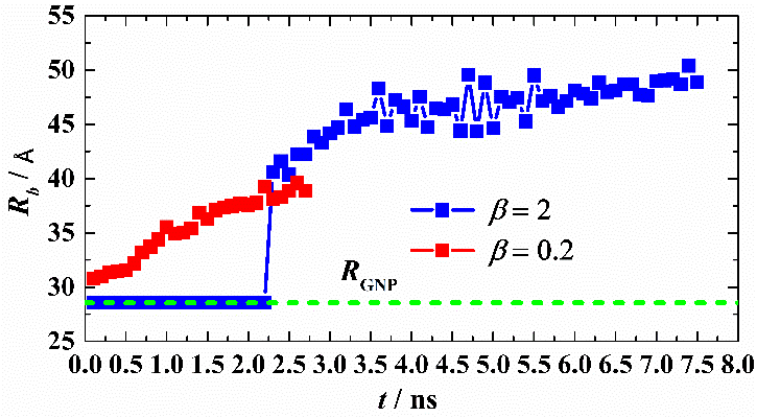

Figure 7.2: Time evolutions of nanobubble radius (R_b) for GNPs with β = 2 and 0.2 under Q = 1.4 eV·ps^{-1}. R_{GNP} represents the radius of the nanoparticles.

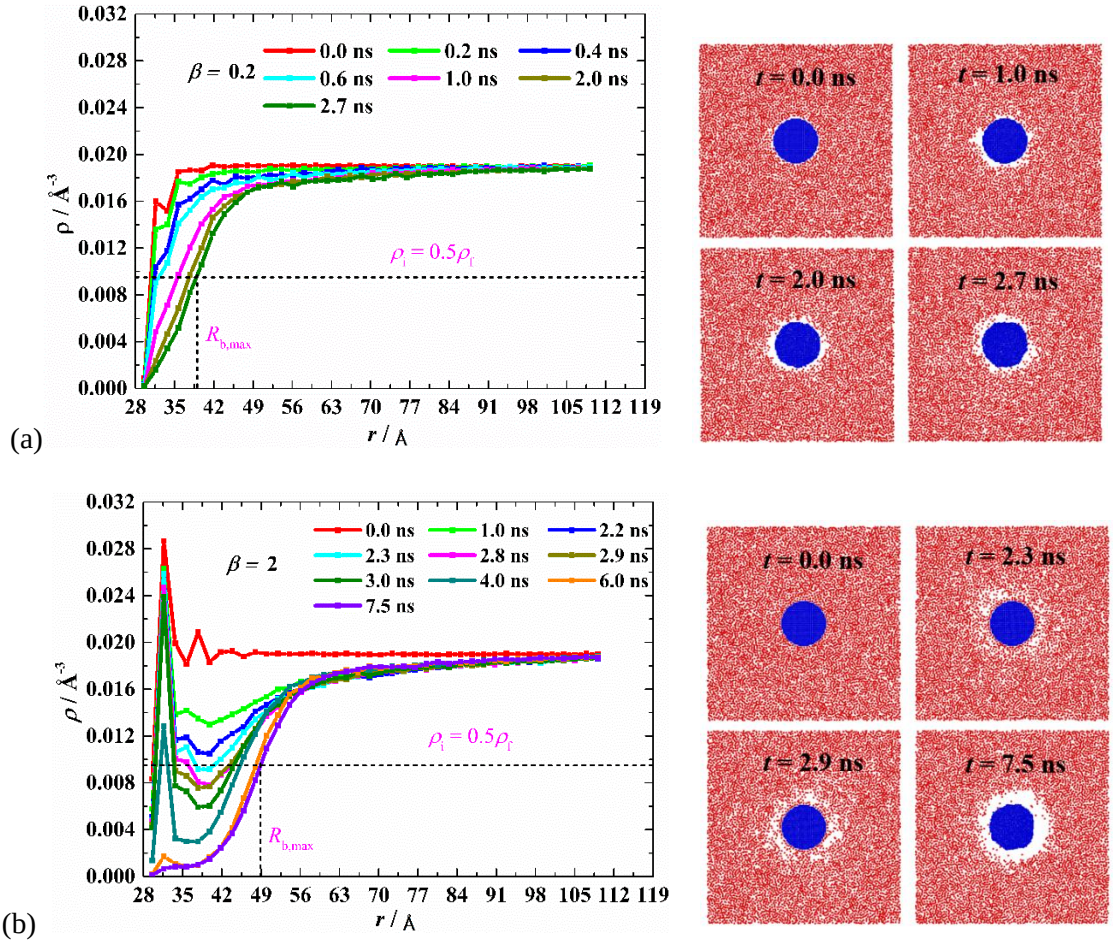

Figure 7.3: Transient radial density profiles and snapshots for GNPs under Q = 1.4 eV·ps^{-1}. (a) β = 0.2. (b) β = 2. ρ_i is the density of vapor-liquid interface and used to characterize nanobubble radius R_b.

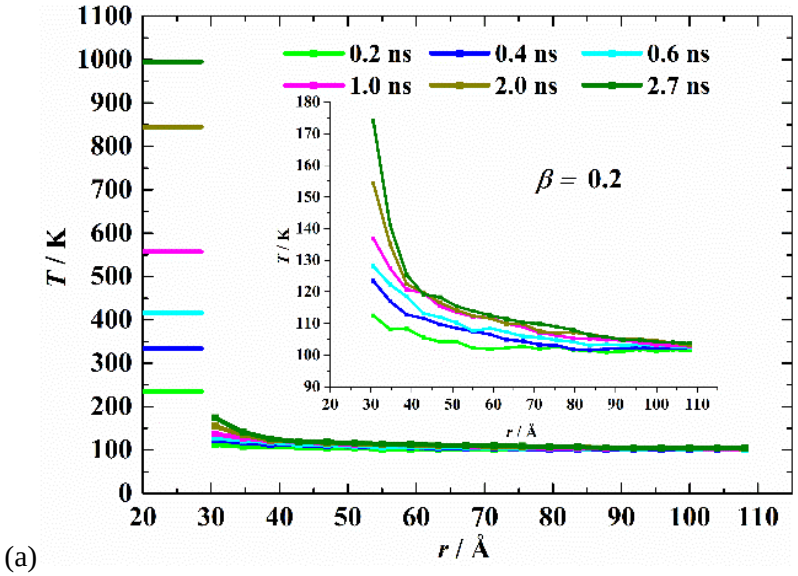

(a)

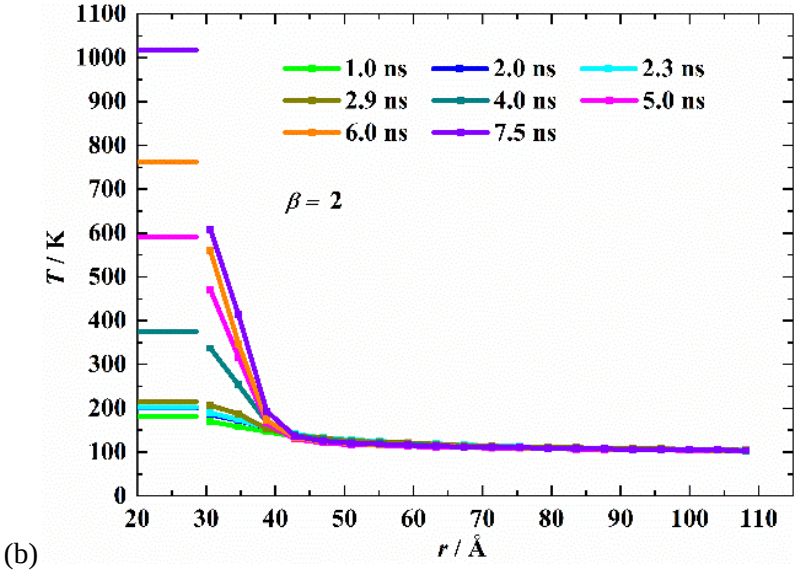

(b)

Figure 7.4: Transient radial temperature profiles of GNPs and fluid under Q = 1.4 eV·ps^{-1}. (a) β = 0.2 and (b) β = 2.

7.2.2 Heating-up characteristics of GNPs

It has been demonstrated that there is a significant suppression of SPR (surface plasmon resonance) in GNPs when they melt to liquid phase, which may disable the function of SPR [173],[174]. Additionally, for biomedical applications, where biosafety must be primarily considered and potential toxicity of photothermal production must be prevented, nanoparticles must be remained solid and intact [175]. Therefore, the heating-up

characteristics of GNPs is of importance and is also concerned in this work. Figure 7.5 displays the typical time evolutions of T_{GNP} after the GNPs with β = 2 and 0.2 are heated under Q = 1.4 eV·ps^{-1}. The T_m is marked by the green dash line. In Figure 7.5, based on the phase state of the GNPs, the heating procedure is divided into three stages. Stage I demonstrates the solid stage ($t < t_1$), during which the GNPs remain solid though T_{GNP} keeps increasing to T_m. For β = 2 and 0.2, t_1 are 7.5 ns and 2.7 ns, respectively. Stage II demonstrates the melting stage ($t_1 \leq t < t_2$), during which the GNPs completely melts into liquid. For β = 2 and 0.2, t_2 are 8.6 ns and 3.3 ns, respectively. Stage III demonstrates the liquid stage ($t \geq t_2$), during which the GNPs are physically molten. This stage is beyond the scope of the present work, thus T_{GNP} is merely recorded for a certain period of time.

For β = 2, two different increasing trends of T_{GNP} are observed in Stage I. We define the time at the turning point as t_0 (= 2.9 ns). When $t > t_0$, the temperature increasing rate is observed to become higher. Note that the increase in T_{GNP} is dependent on the difference between the heat input and output on the GNPs. In our simulations, the input heating intensity is constant, thus we conjecture that there is a thermally insulating vapor layer forming around the GNP from t_0, which leads to the decrease in heat dissipation from the GNP and the significant increase in T_{GNP}. However, it is worth noting that t_0 is larger than t_d (=2.3 ns) when nanobubble appears. To explain this phenomenon, the density profiles and snapshots at some typical times are depicted (see Figure 7.3(b)). At $t = t_d$ (2.3 ns), the nanobubble forms at a certain distance from the GNP surface but the fluid density in the near-surface region is still larger than ρ_i, thus the heat transfer between the GNP and surrounding fluid is not deteriorated and the increase of T_{GNP} still holds. When $t = t_0$ (2.9 ns), except the adsorbed fluid on the GNP surface, the fluid density in the entire near-surface region starts to become lower than ρ_i (see Figure 7.3(b)), which proves that there indeed forms a thermally insulating layer around the GNP that deteriorates the heat transfer from the GNP to the surrounding

fluid. Therefore, the slope of T_{GNP} changes from t_0 instead of t_d. Based on above analysis, it is found that although the nanobubble first forms at t_d, the fluid adjacent to the GNP surface still remains liquid until $t = t_0$. Therefore, according to the fluid state around GNPs, Stage I for $\beta = 2$ can be further divided into two sub-stages, namely Stage I^{s-l} (solid-liquid heat transfer stage, $t < t_0$) and Stage I^{s-v} (solid-vapor heat transfer stage, $t_0 \leq t < t_1$). In Stage I^{s-v}, T_{GNP} significantly increases and nanobubble keeps growing. From Figure 7.3(b), it is also seen that the adsorbed liquid layer on the GNP surface would vaporize and finally the surface turns dry. For $\beta = 0.2$, there shows only one temperature increasing trend for T_{GNP} in Stage I. Based on Figure 7.3(a) and above discussion, this Stage I is actually equivalent to Stage I^{s-v}. Different from $\beta = 2$, there is no adsorbed high-density layer on the GNP surface for $\beta = 0.2$ and instead low-density fluid layer in the near-surface region is observed (see Figure 7.3(a)). Moreover, the GNP with $\beta = 0.2$ has high fluid-solid interfacial thermal resistance. Thus, there behaves the characteristic of solid-vapor heat transfer instantly after the GNP is heated, where T_{GNP} apparently increases. Noticeably, because the case with $\beta = 0.2$ holds higher interfacial thermal resistance than that with $\beta = 2$, the increase of T_{GNP} for $\beta = 0.2$ is much faster than that for $\beta = 2$ in Stage I^{s-v}, where the nanobubble forms around the GNPs surface.

When nanobubble forms around GNPs, the heat transfer from GNPs significantly deteriorates, which leads to significant increase in T_{GNP}. Finally, T_{GNP} increases to T_m and GNPs starts to melt. For $\beta = 2$ and 0.2, the periods of time reaching the melting point t_1 equal to 7.5 ns and 2.7 ns, respectively. The melting of the whole GNPs would experience a period of time rather than an instant process at a defined temperature. Additionally, there appears a decrease in T_{GNP} during the melting process. The reason is that the solid-liquid transition leads to increase in the interatomic distance, which results in dramatic increase in its potential energy. However, the energy supplied from external system could not instantly

compensate for the increase of the GNPs potential energy. Therefore, part of kinetic energy converts into potential energy, which causes the decrease in T_{GNP} [176]. Shortly afterwards, T_{GNP} starts to increase again, and it is followed by Stage III after the melting stage, where GNPs continue to be heated in liquid state. Figure 7.6 demonstrates the snapshots for GNPs configuration at some typical times. To clearly visualize the change of GNPs configuration, some atoms are marked in red. It is seen that the GNPs first melt from the surface ($t = t_1$ = 7.5 ns for $\beta = 2$ and $t = t_1$ = 2.7 ns for $\beta = 0.2$) and then the melting process proceeds inwards. When $t \geq t_2$ (t_2 = 8.6 ns for $\beta = 2$ and t_2 = 3.3 ns for $\beta = 0.2$), the configuration of GNPs is seen completely disordered and behaves as liquid.

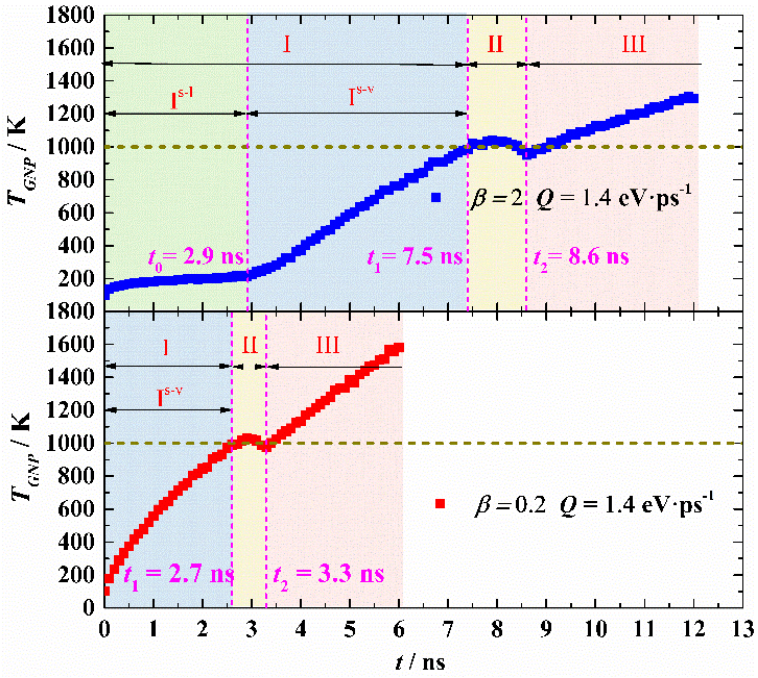

Figure 7.5: Time evolution of the GNPs temperature for $\beta = 2$ and 0.2 under $Q = 1.4$ eV·ps^{-1}.

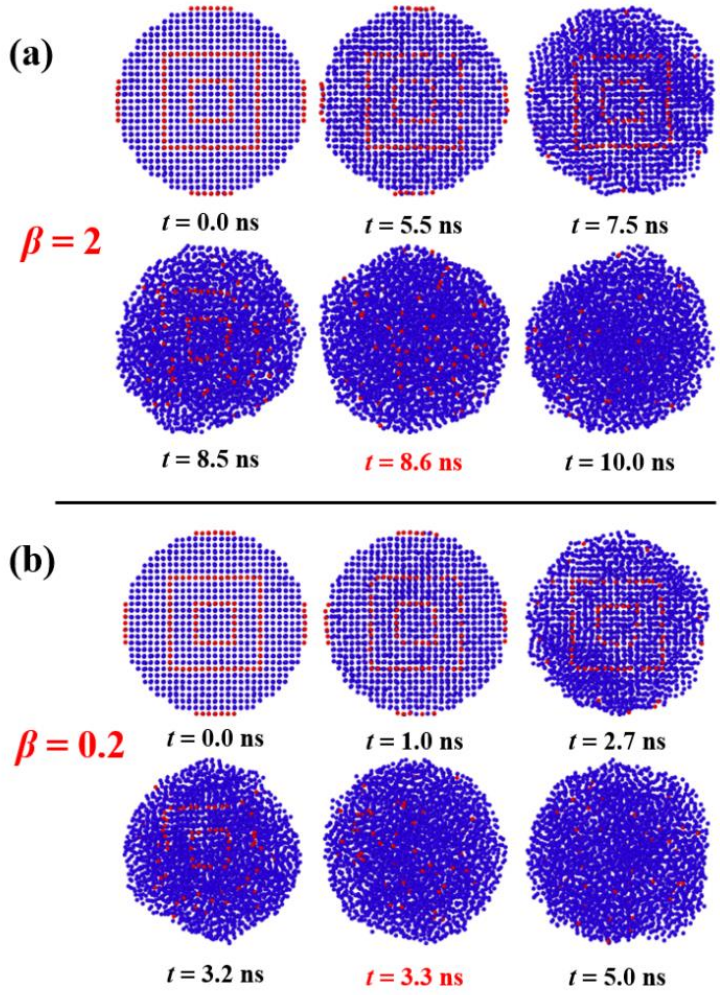

Figure 7.6: Snapshots of melting process of GNPs under Q = 1.4 eV·ps^{-1} with (a) β = 2 and (b) β = 0.2. Some atoms are marked in red for clearly observing.

7.2.3 Effect of heating intensity

Different Q from 1.0 to 3.0 eV·ps^{-1} are considered to investigate the effect of heating intensity. Based on the density profiles of the surrounding fluid, the time evolutions of R_b for different cases are depicted in Figure 7.7. For β = 0.2, it is obvious that nanobubble grows faster with higher Q and there is no postponement for nanobubble generation. For β = 2, the delay of nanobubble generation is observed for all cases, where a giant nanobubble first forms and then it grows slightly. With Q increasing, the delay for nanobubble generation, i.e., t_d, decreases. Noteworthily, $R_{b,max}$ is found to be dependent on β not Q. It can be more

apparently observed from the radial density profiles of the surrounding fluid at t_1 shown in Figure 7.8(a), where $R_{b,max}$ for β = 0.2 and 2 are 39 Å and 49 Å, respectively. The reason is three-folded. First, T_m is the intrinsic thermosphysical property that is independent of β and Q (see A.2 in Appendix) and also the temperature of heat sink is maintained constant in the present work. This equivalently gives the fixed temperature boundary conditions in the radial direction. Second, the temperature profiles are solely dependent on the thermal resistances, including the bulk and interfacial thermal resistances, in the radial direction once the temperature at the boundaries are fixed. Third, it is known, from our earlier studies [55],[58], that the solid-fluid interfacial thermal resistance is highly dependent on β (higher β leads to lower resistance). Therefore, the temperature profile and the density profile converge at T_m. This convergence is dependent on β not Q (see Figure 7.8(b)) although larger Q accelerates the convergence (see Figure 7.9).

Correspondingly, the time evolutions of T_{GNP} are depicted in Figure 7.9 with different Q. It is seen that when Q is low, T_{GNP} rapidly increases to a steady state and then remains constant, which indicates a heat balance between the input and output of the GNPs. Meanwhile, no nanobubble generation is observed. Thus, we conclude that there exists a threshold Q for nanobubble generation. It is seen that the threshold Q for β = 0.2 is lower than that for β = 2. Because when Q = 1.0 eV·ps^{-1}, for β = 0.2 T_{GNP} has not reached a steady state while for β = 2, T_{GNP} finally evolves to. For non-steady cases, T_{GNP} evolves through the same stages when β are identical. For β = 2 and 0.2, different characteristic times are summarized in Figure 7.10. All different characteristic times dramatically decrease with increasing Q for both β = 2 and 0.2, which means that all these processes bring forward with increasing Q, namely faster nanobubble generation and GNPs melting. For β = 2, the difference between t_d and t_1 decreases with increasing Q and they become equal when Q reaches a certain value, which means nanobubble generates more explosively with higher Q. For a given Q, although the

GNP with β = 0.2 generates nanobubble faster (t_d = 0 ns) and starts melting earlier (smaller t_1) than the GNP with β = 2, these differences decrease with increasing Q.

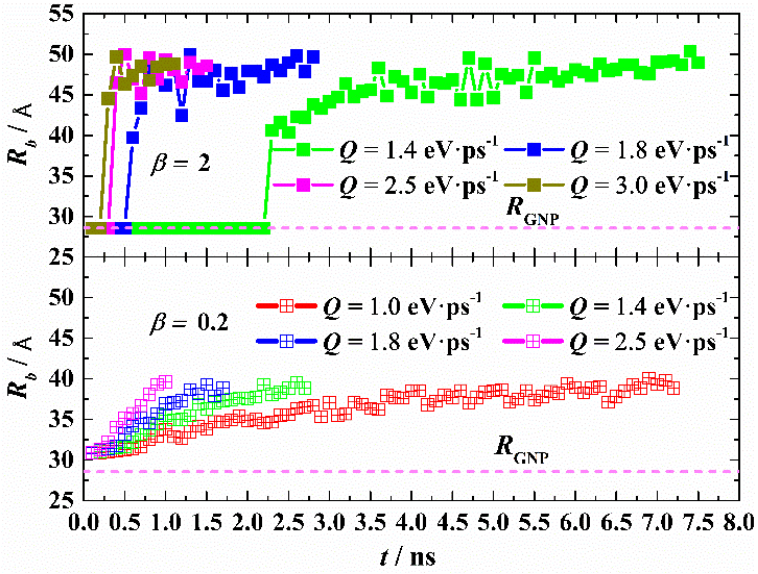

Figure 7.7: Time evolution of nanobubble radius R_b for GNPs with β = 2 and 0.2 under different Q.

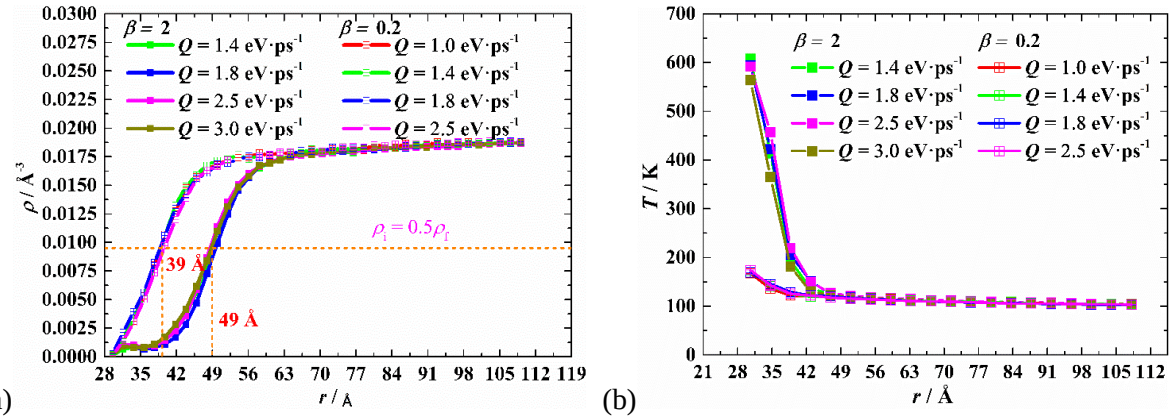

Figure 7.8: Radial (a) density profiles and (b) temperature profiles of fluid for GNPs with β = 2 and 0.2 under different Q at t_1 that the temperature of the GNPs reaches the melting point.

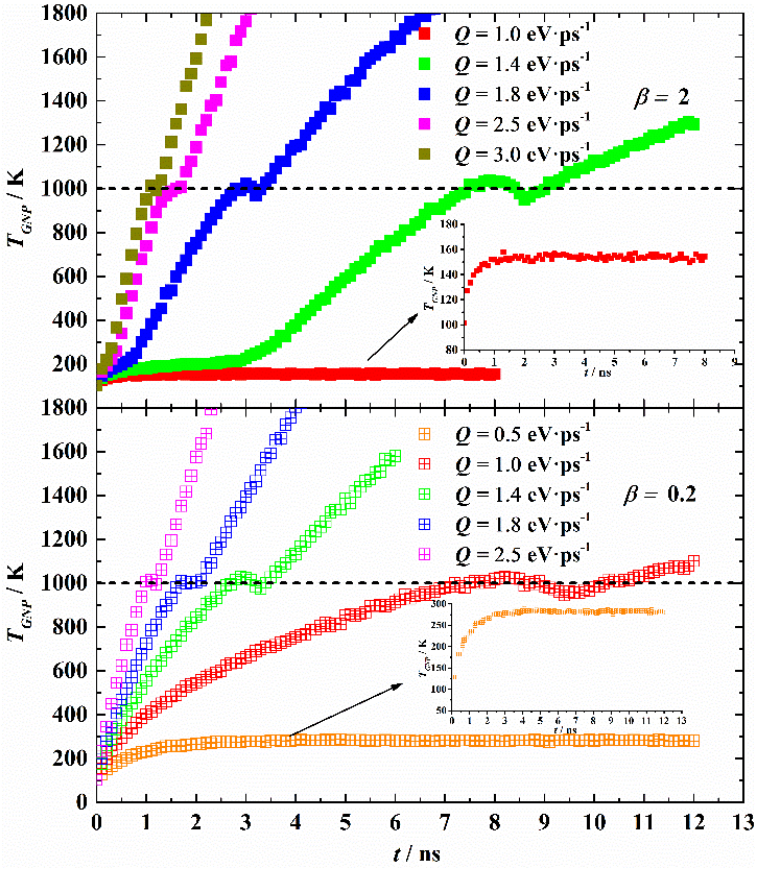

Figure 7.9: Time evolution of the temperature of GNPs with β = 2 and 0.2 under different Q.

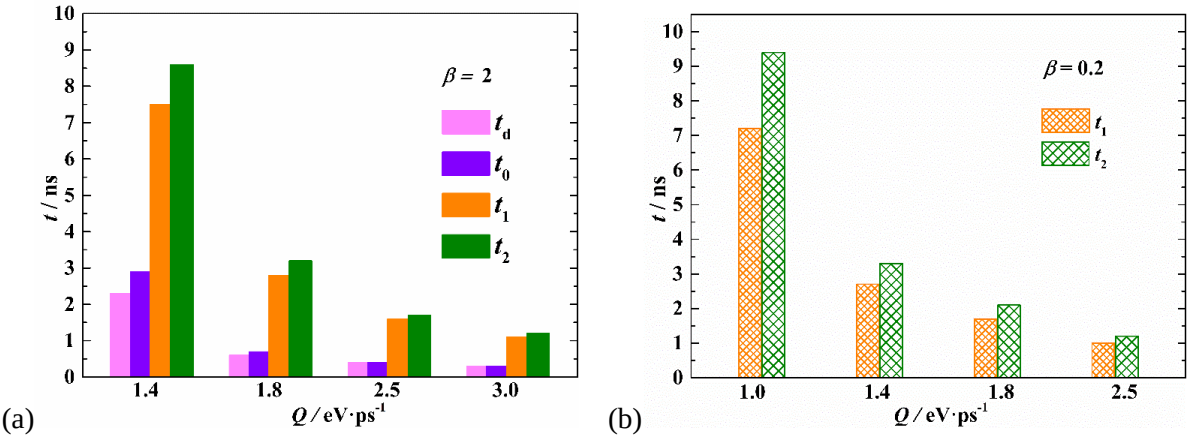

(a) (b)

Figure 7.10: Different characteristic times for (a) β = 2 and (b) β = 0.2 under different Q. t_d is the delay time that nanobubble generates after GNPs are heated. t_0 is the start time of the solid-vapor heat transfer stage. t_1 is the time that the temperature of GNPs reaches the melting temperature T_m. t_2 is the time that GNPs completely turn to liquid state.

7.3 Conclusion

In this work, the dependences of surface wettability and heating intensity on the generation and evolution of nanobubble around two types of GNPs have been investigated. The nanobubble generation is observed to delay on the super-hydrophilic GNP (β = 2) but not to delay on the super-hydrophobic GNP (β = 0.2). Correspondingly, nanobubble generates faster on the super-hydrophobic GNP than on the super-hydrophilic GNP. The nanobubble generation is promoted by larger temperature difference between the GNP and surrounding fluid. The nanobubble deteriorates the heat transfer between the GNP and surrounding fluid and leads to dramatic increase in T_{GNP}. Therefore, if nanobubble does not detach fast, GNPs would melt. For the super-hydrophobic GNP, nanobubble first forms at a distance from the GNP surface instead of on the GNP surface, thus explosive generation of nanobubble (large R_b) is observed. For the super-hydrophilic GNP, there already exists an ultrathin low-density layer before the GNP is heated due to weak attraction between the GNP and surrounding fluid, which enhances the fast generation of nanobubble. For a given β, with increasing Q, the generation and evolution of nanobubble behave faster. Meanwhile, GNPs also start to melt more quickly. Additionally, $R_{b,max}$ is found to be dependent on β not Q and the mechanism is revealed based on thermal resistance analysis at the melting point. Moreover, a threshold of Q exists for nanobubble generation and the value for the super-hydrophobic GNP is lower than that for the super-hydrophilic GNP. Based on the present work, the super-hydrophobic GNP is found favorable for fast and energy-saving nanobubble generation.

8 Summaries and Outlook

8.1 Summaries

In this thesis, different liquid-vapor phase-change processes are systematically investigated using molecular dynamics (MD) method. The work in this thesis enriches the fundamental understanding of these processes and shed light on the enhance and control of these processes.

In the journey of study surface condensation process, we first reveal the formation and transition mechanism of different condensation modes. We have observed five different formation mechanisms for surface condensation mode. When surface wettability (β) and solid-fluid temperature difference (ΔT) are very low, the energy barrier ΔG^* is so high that clusters cannot survive and develop to droplet or film thus non-condensation (NC) mode is appeared. For dropwise condensation (DWC) and filmwise condensation (FWC) modes, both of them can evolve from two different pathways: DWC could evolve from either nucleation or film rupture; FWC could develop from either nucleation or the adsorption-induced thin film. We reveal that according to classic nucleation theory, the transition between NC and DWC depends on ΔG^*: lower ΔG^*, e.g., high β and ΔT cases, benefits the survival of surface clusters and the occurrence of condensation. For the transition between DWC and FWC, it is determined by the competition between the tendency of contraction and rupture of the uneven condensate and the tendency of continually growth of the uneven condensate. When the former trend dominates, DWC occurs, otherwise FWC appears.

We then consider the effect of tangentially external force field (f_e) on the nano-confined surface condensation. We qualitatively demonstrate that as f_e increases or/and β decreases, both the velocity slip and temperature jumping near the surface become significant. Due to the existence of f_e, the droplets coalescence is promoted, and the condensed droplets show asymmetrical. In the meantime, the onset of surface condensation is postponed or even inhibited with f_e increasing. We have extended the general understanding about the interfacial thermal resistance (R_{th}). Based on the heat transfer analysis, we find that f_e, as a bulk factor, indirectly affects the R_{th} by direct influence on the surface condensation resulting from the generation of dissipated heat. We have quantitatively carried out the energy balance analysis for all simulation cases and pointed out that for non-condensation cases, the heat transferred from fluid to solid mainly comes from the dissipated heats, but for condensation cases, that mainly arises from the change in the internal energy (U). The work done by external force (W) mainly converts into dissipated heats in all cases and only in the no-condensation case, a small part of W converts into E_k (macroscopic kinetic energy). We also reveal that in the nano-confined channel, the dissipated heat due to the existence of f_e shows significant effect as the internal heat source on the condensation. It suppresses the further decrease in U and consequently the condensation is postponed or even suppressed.

We finally investigate the growth and self-jumping of nanodroplets on nanostructured surfaces. Our work proves that it is effective to achieve condensed droplet self-jumping driven by the Laplace-pressure for nano-size droplet. We detailly demonstrate the growth and self-jumping process of nanodroplet: an individual droplet first appears on the hydrophilic pinning site and grows in the nanogroove; gradually the droplet top emerges from the nanogroove and freely grows with pinned contact line at the groove edges but its bottom is still confined in the nanogroove, which leads to a curvature difference between the droplet top and bottom and a Laplace pressure difference is set up within the droplet; when

the pressure difference is larger than the pinning force from the hydrophilic pinning site, the droplet detaches from the groove valley and finally self-jumps from the nanostructured surface. In this process, we observed a condensed droplet with radius of 7.5 nm self-jumping from the nanostructured surface with jumping velocity of 0.0643 $Å \cdot ps^{-1}$. We also find that although the pinning site with larger β and size can benefit the droplet growth, it blocks the droplet self-jumping owning to the increase in the total pinning force. We finally reveal that the confined portion of the detachment droplet highly influences the droplet-jumping and the larger it is, the more possible the occurrence of droplet self-jumping.

In the journey of study liquid-to-vapor process, we first focus on the stale and efficient nanofilm evaporation on nanopillar surfaces. We have determined the capillary pressure in a unit cell of nanopillars by MD simulations and it is in good agreement with that derived from a force balance method. We find that for simulated perfectly wetting fluid, the meniscus is pinned at the top of the nanopillars during evaporation. The curvature of the meniscus close to the nanopillars varies dramatically. Nanobubbles appear when liquid overcomes the potential energy barrier. They first evolve from the corner of nanopillars due to the quick increase in the potential energy there then coalesce and expand toward the unit centre. According to the parametric study, we obtain that the evaporation can be enhanced by decreasing the pitch between two pillars (*P*), increasing the diameter of the pillar (*D*) and decreasing the height of the pillar (*H*), while the former two methods will raise the risk of boiling. Thus, a trade-off between enhancing evaporation and achieving stable evaporation is needed when determining *P*, *D*, and *H*. We report that the thickness of nanofilm has significant effect on maintaining efficient evaporation. The nanofilm thickness should be maintained larger than a threshold to avoid the suppression on evaporation from disjoining pressure. To achieve more efficient evaporation on nanopillar surface than that on smooth surface, the nanofilm thickness should be forced beyond the value where suppression effect

on evaporation due to the decrease of the volume of supplied fluid and the existence of capillary pressure starts dominating.

Separately we simulated the generation and evolution of nanobubbles on heated nanoparticles. We find that nanobubble can instantly generate around the superhydrophobic nanoparticle but the formation of nanobubble around the superhydrophilic nanoparticle shows a delay and it shows an explosive behavior. We find that the fast generation of the nanobubble around superhydrophobic nanoparticle is promoted by an ultrathin low-density layer around the nanoparticle before the nanoparticle is heated. The explosive generation of the nanobubble around superhydrophilic nanoparticle is because the nanobubble initially appears at a distance from the nanoparticle surface rather than on the nanoparticle surface. We reveal that the maximum radius of nanobubble depends on surface wettability β and is independent on heating intensity (Q). We also demonstrate the heating-up characteristics of nanoparticles and find that generation of nanobubble impedes the heat transfer between nanoparticle and fluid, which leads to the melting of nanoparticles. Additionally, we find that there is a threshold of Q for the generation nanobubble and the value for the superhydrophilic nanoparticle is larger than that for the superhydrophobic nanoparticle.

8.2 Outlook

Both condensation and boiling processes may experience the dynamic nucleation, growth, coalescence/merge, and departure of droplets and bubbles. The dynamic processes significantly influence the characteristics of phase-change heat transfer and span various length scales from nanoscale to macroscale in most practical applications. Although there are some modeling techniques available to understand the processes, they are only suitable to investigate certain stage. For example, molecular dynamics simulation is a good choice for the nucleation process or dynamic process of nanodroplet or nanobubble; LBM (Lattice

Boltzmann method) can reach the microscale phenomenon; CFD (computational fluid dynamics) method is suitable for investigation in macroscale. Thus, a multiscale numerical method which can cover the whole dynamic processes consisting of different length scales is highly demanded and, in this advanced method, different numerical methods can be coupled by information exchange at the interfaces between different regions. Additionally, the fundamental understanding of phase-change kinetics and liquid-vapor interface needs continuous efforts. The detection about the liquid-vapor interface needs to be improved and the improvement is beneficial to understand the bubble nucleation and evolve. The theoretical model about the evaporative mass flux needs to be corrected based on MD simulations and experimental results.

List of publications

Journal publications

[1] **Pu J. H.;** Sheng Q.; Sun J.; Wang W.; Wang H. S., Dependence of Nano-confined Surface Condensation on Tangentially External Force Field [J]. *Journal of Molecular Liquids*, 2019, 283: 440-450.

[2] **Pu J. H.;** Sun J.; Sheng Q.; Wang W.; Wang H. S., Dependences of Formation and Transition of the Surface Condensation Mode on Wettability and Temperature Difference [J]. *Langmuir*, 2019, 36: 456-464.

[3] **Pu J. H.;** Sun J.; Wang W.; Wang H. S., Generation and Evolution of Nanobubbles on Heated Nanoparticles: A Molecular Dynamics Study [J]. *Langmuir*, 2020, 36: 2375-82.

[4] **Pu J. H.;** Wang S. K.; Sun J.; Wang W.; Wang H. S., Stable and Efficient Nanofilm Pure Evaporation on Nanopillar Surfaces [J]. *Langmuir*, 2020, 37: 3731-3739.

[5] **Pu, J. H.;** Wang, S. K.; Sun, J.; Wang, W.; Wang, H. S., Growth and self-jumping of single condensed droplet on nanostructured surfaces. *Journal of Molecular Liquids*, 116902.

[6] Jivani S., Liu J. H.; **Pu J. H.;** Wang H. S., Marangoni Condensation of Steam-ethanol Mixture on a Horizontal Smooth Tube [J]. *Experimental Thermal and Fluid Science*, 2021, 128: 110434.

Conference papers

[1] **Pu J. H.;** Sheng Q.; Sun J.; Wang W.; Wang H. S., Molecular Dynamics Simulation of Effect of Temperature Difference on Surface Condensation [C]. Proceedings of the 16th UK Heat Transfer Conference (UKHTC2019), September 8-10, Nottingham, UK, 2019.

[2] **Pu J. H.;** Sun J.; Wang W.; Wang H. S., Generation and Evolution of Nanobubbles on Heated Nanoparticles [C]. Sino-Japan-UK Frontiers in Phase Change Heat Transfer and Its Applications in Energy, July 27-29, Xian, China, 2020.

Appendix

A.1 Equilibrium MD simulation

To calculated saturated liquid density (ρ_{sat}) and liquid-vapor surface tension (γ_{lv}), a liquid slab is placed in the middle of a simulation box (see Figure A.1). The box contains 40097 atoms and its size measures $l_x \times l_y \times l_z$ =23.52×5.88×5.88 nm^3. Periodic boundary conditions are applied in all three directions. The system is first equilibrated by NVT ensemble for 6 ns. Then we use 36 ns for data collection and averaging at each temperature. The results for saturated liquid density are shown in Figure A.2. To determine γ_{lv}, the simulation box is divided into 100 planar bins in the *x*-direction, and the value of the pressure tensor in each bin is monitored. Then γ_{lv} is obtained by

$$\gamma_{lv} = \frac{1}{2}\int_{-l_x/2}^{l_x/2}\left[P_N(x) - P_T(x)\right]dx, \tag{A-1}$$

where P_N is the pressure normal to the interface and P_T is tangential pressure. The factor of 1/2 is used due to two liquid-vapor interfaces existing in the simulation box. γ_{lv} at different temperature is presented in Figure A.3.

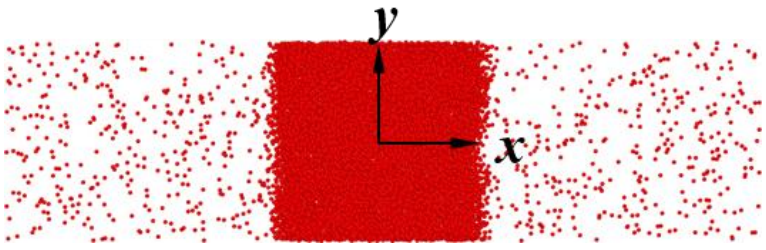

Figure A.1: Equilibrium MD system for determining saturated fluid density and liquid-vapor surface tension. The size of simulation box measures $l_x \times l_y \times l_z$ =23.52×5.88×5.88 nm^3.

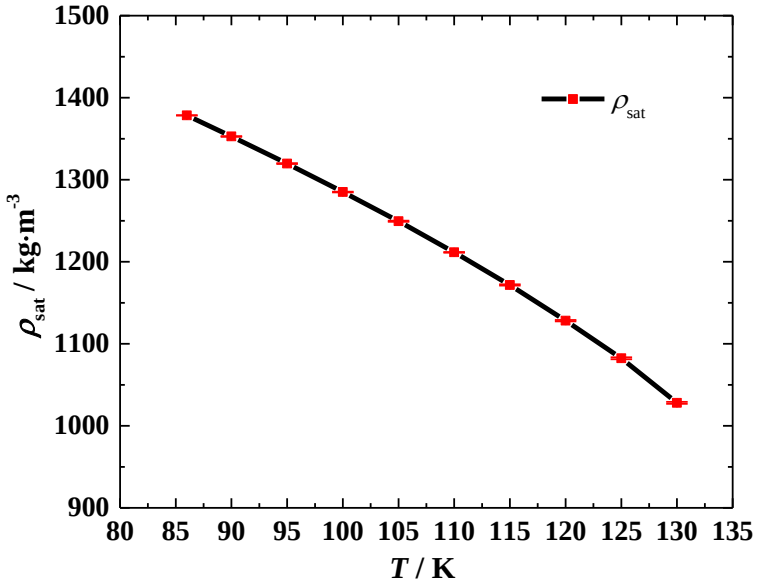

Figure A.2: Saturated fluid density as a function of temperature.

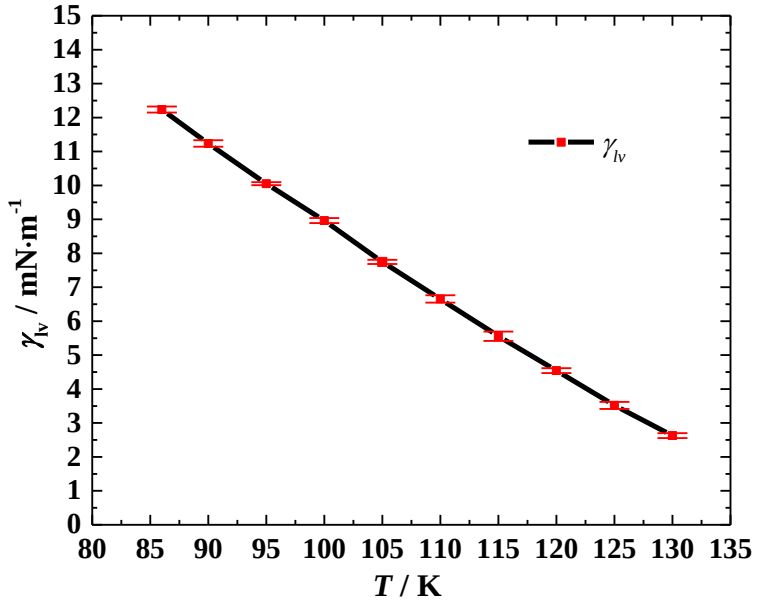

Figure A.3: Liquid-vapor surface tension as a function of temperature.

A.2 Melting temperature T_m of GNPs

Same as the previous MD studies [171],[172], the potential energy per atom and the corresponding temperature of GNPs (T_{GNP}) are recorded to characterize the melting point T_m

of GNPs (see Figure A.4). The T_m can be identified by the rapid change of the slope in the potential energy curve. It is seen that the T_m of GNPs is the intrinsic thermosphysical property and independent of surface wettability β and heating intensity Q. The same T_m of ca. 1000 K could be obtained for the GNPs with β = 0.2 and 2 under different Q values.

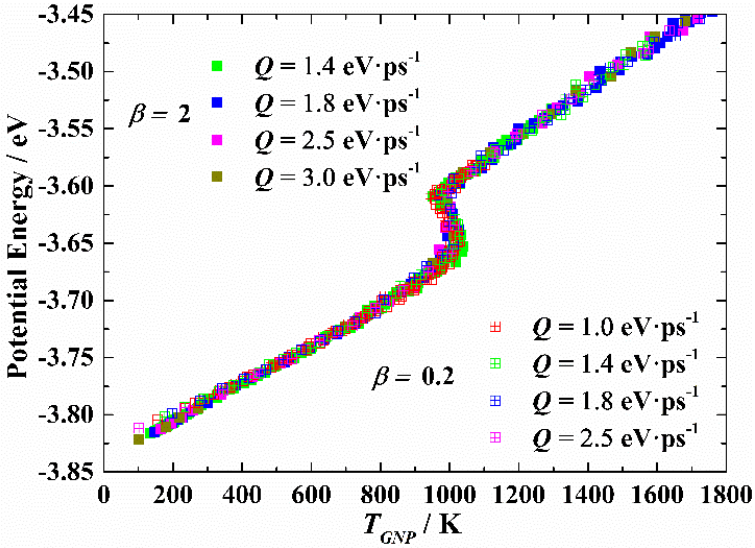

Figure A.4: Potential energy against the temperature of GNPs with β = 2 and 0.2 under different Q values; melting point T_m was found to be ca. 1000 K.

References

[1] Miljkovic, N.; Wang, E. N., Condensation heat transfer on superhydrophobic surfaces. MRS Bulletin 2013, 38 (5), 397-406.

[2] Khan, S. A.; Tahir, F.; Baloch, A. A. B.; Koc, M., Review of Micro–Nanoscale Surface Coatings Application for Sustaining Dropwise Condensation. Coatings 2019, 9 (2), 117.

[3] Liang, G.; Mudawar, I., Review of pool boiling enhancement by surface modification. International Journal of Heat and Mass Transfer 2019, 128, 892-933.

[4] Lewis, N. S., Toward cost-effective solar energy use. Science 2007, 315(5813), 798-801.

[5] Chen, C.; Kuang, Y.; Hu, L., Challenges and opportunities for solar evaporation. Joule 2019, 3 (3), 683-718.

[6] Wen, R.; Ma, X.; Lee, Y.-C.; Yang, R., Liquid-vapor phase-change heat transfer on functionalized nanowired surfaces and beyond. Joule 2018, 2 (11), 2307-2347.

[7] Singh, N. S.; Zhang, J.; Stafford, J.; Anthony, C.; Gao, N., Implementing superhydrophobic surfaces within various condensation environments: a review. Advanced Materials Interfaces 2021, 8 (2), 2001442.

[8] Briggs, A.; Wen, X.-L.; Rose, J. W., Accurate heat transfer measurements for condensation on horizontal, integral-fin tubes. Journal of Heat Transfer 1992, 114 (3), 719-726.

[9] Ali, H.; Kamran, M.; Ali, H.; Imran, S., Condensation heat transfer enhancement using steam-ethanol mixtures on horizontal finned tube. International Journal of Thermal Sciences 2019, 140, 87-95.

[10] Sajjan, S. K.; Kumar, R.; Gupta, A., Experimental investigation of vapor condensation of R-600a over horizontal three-dimensional integral-fin tubes. International Journal of Thermal Sciences 2020, 153, 106378.

[11] Ji, W.-T.; Li, Z.-Y.; Qu, Z.-G.; Guo, J.-F.; Zhang, D.-C.; He, Y.-L.; Tao, W.-Q., Film condensing heat transfer of R134a on single horizontal tube coated with open cell copper foam. Applied Thermal Engineering 2015, 76, 335-343.

[12] Ho, J.; Leong, K., A critical review of filmwise natural and forced convection condensation on enhanced surfaces. Applied Thermal Engineering 2020, 116437.

[13] Schmidt, E.; Schurig, W.; Sellschopp, W., Versuche über die kondensation von wasserdampf in film-und tropfenform. Technische Mechanik und Thermodynamik 1930, 1 (2), 53-63.

[14] Rose, J. W., Dropwise condensation theory and experiment: A review. Proceedings of the Institution of Mechanical Engineers, Part A: Journal of Power and Energy 2005, 216 (2), 115-128.

[15] Hu, H. W.; Tang, G. H.; Niu, D. Experimental investigation of condensation heat transfer on hybrid wettability finned tube with large amount of noncondensable gas, International Journal of Heat and Mass Transfer 2015, 85, 513-523.

[16] Zhang, B. J.; Kuok, C.; Kim, K. J.; Hwang, T.; Yoon, H. Dropwise steam condensation on various hydrophobic surfaces: Polyphenylene sulfide (PPS), polytetrafluoroethylene (PTFE), and self-assembled micro/nanosilver (SAMS). International Journal of Heat and Mass Transfer 2015, 89, 353–358.

[17] Mondal, B.; Eain, M. M. G.; Xu, Q.; Egan, V. M.; Punch, J.; Lyons, A. M. Design and fabrication of a hybrid superhydrophobic–hydrophilic surface that exhibits stable dropwise condensation. ACS Applied Mmaterials & Interfaces 2015, 7(42), 23575–23588.

[18] Hu, H. W.; Tang, G. H.; Niu, D. Experimental investigation of convective condensation heat transfer on tube bundles with different surface wettability at large amount of noncondensable gas. Applied Thermal Engineering 2016, 100, 699-707.

[19] Shen, L. Y.; Tang, G. H.; Li, Q.; Shi, Y. Hybrid Wettability-Induced Heat Transfer Enhancement for Condensation with NonCondensable Gas. Langmuir, 2019, 35, 9430-9440.

[20] Guo, L.; Tang, G. H.; Dropwise condensation on bioinspired hydrophilic slippery surface, RSC Advances 2018, 8(69), 39341.

[21] Miljkovic, N.; Enright, R.; Nam, Y.; Lopez, K.; Dou, N.; Sack, J.; Wang E. N. Jumping-droplet-enhanced condensation on scalable superhydrophobic nanostructured surfaces. Nano Letters 2012, 13(1), 179-187.

[22] Hou, Y.; Yu, M.; Chen, X.; Wang, Z.; Yao, S. Recurrent filmwise and dropwise condensation on a beetle mimetic surface. ACS Nano 2014, 9(1), 71-81.

[23] Enright, R.; Miljkovic, N.; Alvarado, J. L.; Kim, K.; Rose, J. W. Dropwise condensation on micro-and nanostructured surfaces. Nanoscale and Microscale Thermophysical Engineering 2014, 18(3), 223-250.

[24] Wen, R.; Xu, S.; Zhao, D.; Yang, L.; Ma, X.; Liu, W.; Lee, Y.; Yang, R. Sustaining enhanced condensation on hierarchical mesh-covered surfaces. National Science Review 2018, 5(6), 878-887.

[25] Gao, S; Liu, W.; Liu, Z. Tuning nanostructured surfaces with hybrid wettability areas to enhance condensation. Nanoscale 2019, 11(2), 459-466.

[26] Orejon, D.; Askounis, A.; Takata, Y.; Attinger, D., Dropwise condensation on multiscale bioinspired metallic surfaces with nanofeatures. ACS Applied Materials & Interfaces 2019, 11 (27), 24735-24750.

[27] Sett, S.; Sokalski, P.; Boyina, K.; Li, L.; Rabbi, K. F.; Auby, H.; Foulkes, T.; Mahvi, A.; Barac, G.; Bolton, L. W., Stable dropwise condensation of ethanol and hexane on rationally

designed ultrascalable nanostructured lubricant-infused surfaces. Nano Letters 2019, 19 (8), 5287-5296.

[28] O'neill, G. A.; Westwater, J., Dropwise condensation of steam on electroplated silver surfaces. International Journal of Heat and Mass Transfer 1984, 27 (9), 1539-1549.

[29] Shim, J.; Seo, D.; Oh, S.; Lee, J.; Nam, Y., Condensation Heat-Transfer Performance of Thermally Stable Superhydrophobic Cerium-Oxide Surfaces. ACS Applied Materials & Interfaces 2018, 10 (37), 31765-31776.

[30] Qi, Z.; Dongchang, Z.; Jifang, L., Surface materials with dropwise condensation made by ion implantation technology. International Journal of Heat and Mass Transfer 1991, 34 (11), 2833-2835.

[31] Xie, J.; Xu, J.; Li, X.; Liu, H., Dropwise condensation on superhydrophobic nanostructure surface, Part I: Long-term operation and nanostructure failure. International Journal of Heat and Mass Transfer 2019, 129, 86-95.

[32] Wen, R.; Xu, S.; Zhao, D.; Lee, Y.-C.; Ma, X.; Yang, R., Hierarchical superhydrophobic surfaces with micropatterned nanowire arrays for high-efficiency jumping droplet condensation. ACS Aapplied Materials & Interfaces 2017, 9 (51), 44911-44921.

[33] Wen, R.; Li, Q.; Wu, J.; Wu, G.; Wang, W.; Chen, Y.; Ma, X.; Zhao, D.; Yang, R., Hydrophobic copper nanowires for enhancing condensation heat transfer. Nano Energy 2017, 33, 177-183.

[34] Narhe, R.; Beysens, D., Growth dynamics of water drops on a square-pattern rough hydrophobic surface. Langmuir 2007, 23 (12), 6486-6489.

[35]Enright, R.; Miljkovic, N.; Al-Obeidi, A.; Thompson, C. V.; Wang, E. N., Condensation on superhydrophobic surfaces: the role of local energy barriers and structure length scale. Langmuir 2012, 28 (40), 14424-14432.

[36] Rykaczewski, K.; Chinn, J.; Walker, M. L.; Scott, J. H. J.; Chinn, A.; Jones, W., Dynamics of nanoparticle self-assembly into superhydrophobic liquid marbles during water condensation. ACS Nano 2011, 5 (12), 9746-9754.

[37] Narhe, R. a.; Beysens, D., Water condensation on a super-hydrophobic spike surface. EPL (Europhysics Letters) 2006, 75 (1), 98.

[38] Lau, K. K.; Bico, J.; Teo, K. B.; Chhowalla, M.; Amaratunga, G. A.; Milne, W. I.; McKinley, G. H.; Gleason, K. K., Superhydrophobic carbon nanotube forests. Nano Letters 2003, 3 (12), 1701-1705.

[39] Hou, Y.; Yu, M.; Chen, X.; Wang, Z.; Yao, S., Recurrent filmwise and dropwise condensation on a beetle mimetic surface. ACS Nano 2015, 9 (1), 71-81.

[40] Chen, C.-H.; Cai, Q.; Tsai, C.; Chen, C.-L.; Xiong, G.; Yu, Y.; Ren, Z., Dropwise condensation on superhydrophobic surfaces with two-tier roughness. Applied Physics Letters 2007, 90 (17), 173108.

[41] Kim, B. H.; Beskok, A.; Cagin, T., Viscous heating in nanoscale shear driven liquid flows. Microfluidics and nanofluidics 2010, 9 (1), 31-40.

[42] Li, Z., Surface effects on friction-induced fluid heating in nanochannel flows. Physical Review E 2009, 79 (2), 026312.

[43] Sun, J.; Wang, W.; Wang, H. S., Dependence of nanoconfined liquid behavior on boundary and bulk factors. Physical Review E 2013, 87 (2), 023020.

[44] Sun, J.; Wang, W.; Wang, H. S., Dependence between velocity slip and temperature jump in shear flows. The Journal of chemical physics 2013, 138 (23), 234703.

[45] Kholmurodov, K.; Yasuoka, K.; Zeng, X. C., Molecular dynamics simulation of supersaturated vapor nucleation in slit pore. II. Thermostatted atomic-wall model. The Journal of Chemical Physics 2001, 114 (21), 9578-9584.

[46] Suh, D.; Yasuoka, K.; Zeng, X. C., Molecular dynamics simulation of heterogeneous nucleation on nanotubes. RSC Advances 2015, 5 (51), 40953-40963.

[47] Xu, W.; Lan, Z.; Peng, B.; Wen, R.; Ma, X., Effect of surface free energies on the heterogeneous nucleation of water droplet: A molecular dynamics simulation approach. The Journal of Chemical Physics 2015, 142 (5), 054701.

[48] Niu, D.; Tang, G., The effect of surface wettability on water vapor condensation in nanoscale. Scientific Reports 2016, 6 (1), 1-6.

[49] Kraska, T., Molecular-dynamics simulation of argon nucleation from supersaturated vapor in the NVE ensemble. The Journal of Chemical Physics 2006, 124 (5), 054507.

[50] Wedekind, J.; Reguera, D.; Strey, R., Finite-size effects in simulations of nucleation. The Journal of chemical physics 2006, 125 (21), 214505.

[51] Tanaka, K. K.; Kawano, A.; Tanaka, H., Molecular dynamics simulations of the nucleation of water: Determining the sticking probability and formation energy of a cluster. The Journal of Chemical Physics 2014, 140 (11), 114302.

[52] Niu, D.; Tang, G., Molecular dynamics simulation of droplet nucleation and growth on a rough surface: revealing the microscopic mechanism of the flooding mode. RSC Advances 2018, 8 (43), 24517-24524.

[53] Angélil, R.; Diemand, J.; Tanaka, K. K.; Tanaka, H., Properties of liquid clusters in large-scale molecular dynamics nucleation simulations. The Journal of Chemical Physics 2014, 140 (7), 074303.

[54] Sun, J.; Wang, H. S., Self-shedding and sweeping of condensate on composite nano-surface under external force field: enhancement mechanism for dropwise and filmwise condensation modes. Scientific reports 2017, 7 (1), 1-8.

[55] Pu, J. H.; Sheng, Q.; Sun, J.; Wang, W.; Wang, H. S., Dependence of nano-confined surface condensation on tangentially external force field. Journal of Molecular Liquids 2019, 283, 440-450.

[56] Wang, Q.; Xie, H.; Hu, Z.; Liu, C., The impact of the electric field on surface condensation of water vapor: Insight from molecular dynamics simulation. Nanomaterials 2019, 9(1), 64.

[57] Sheng, Q.; Sun, J.; Wang, Q.; Wang, W.; Wang, H. S., On the onset of surface condensation: formation and transition mechanisms of condensation mode. Scientific Reports 2016, 6 (1), 1-9.

[58] Sun, J.; Wang, H. S., On the early and developed stages of surface condensation: competition mechanism between interfacial and condensate bulk thermal resistances. Scientific Reports 2016, 6 (1), 1-12.

[59] Yasuoka, K.; Gao, G.; Zeng, X. C., Molecular dynamics simulation of supersaturated vapor nucleation in slit pore. The Journal of Chemical Physics 2000, 112 (9), 4279-4285.

[60] Xu, W.; Lan, Z.; Peng, B.; Wen, R.; Ma, X., Effect of surface free energies on the heterogeneous nucleation of water droplet: A molecular dynamics simulation approach. The Journal of Chemical Physics 2015, 142 (5), 054701.

[61] Boreyko, J. B.; Chen, C. H., Restoring superhydrophobicity of lotus leaves with vibration-induced dewetting. Physical Review Letters 2009, 103 (17), 174502.

[62] Cheng, Z.; Lai, H.; Zhang, N.; Sun, K.; Jiang, L., Magnetically induced reversible transition between Cassie and Wenzel states of superparamagnetic microdroplets on highly hydrophobic silicon surface. The Journal of Physical Chemistry C 2012, 116 (35), 18796-18802.

[63] Wang, Q.; Yao, X.; Liu, H.; Quere, D.; Jiang, L., Self-removal of condensed water on the legs of water striders. Proceedings of the National Academy of Sciences 2015, 112 (30), 9247-52.

[64] Singh, N. S.; Zhang, J.; Stafford, J.; Anthony, C.; Gao, N., Implementing superhydrophobic surfaces within various condensation environments: a review. Advanced Materials Interfaces 2021, 8(2), 2001442.

[65] Anand, S.; Paxson, A. T.; Dhiman, R.; Smith, J. D.; Varanasi, K. K., Enhanced condensation on lubricant-impregnated nanotextured surfaces. ACS Nano 2012, 6(11), 10122-10129.

[66] Smith, J. D.; Dhiman, R.; Anand, S.; Reza-Garduno, E.; Cohen, R. E.; McKinley, G. H.; Varanasi, K. K., Droplet mobility on lubricant-impregnated surfaces. Soft Matter 2013, 9(6), 1772-1780.

[67] Guo, L.; Tang, G. H.; Kumar, S., Dynamic wettability on the lubricant-impregnated surface: from nucleation to growth and coalescence. ACS Applied Materials & Interfaces 2020, 12 (23), 26555-26565.

[68] Ho, J. Y.; Rabbi, K. F.; Sett, S.; Wong, T. N.; Miljkovic, N., Dropwise condensation of low surface tension fluids on lubricant-infused surfaces: Droplet size distribution and heat transfer. International Journal of Heat and Mass Transfer 2021, 172, 121149.

[69] Boreyko, J. B.; Chen, C. H., Self-propelled dropwise condensate on superhydrophobic surfaces. Physical Review Letters 2009, 103 (18), 184501.

[70] Miljkovic, N.; Enright, R.; Nam, Y.; Lopez, K.; Dou, N.; Sack, J.; Wang, E. N., Jumping-droplet-enhanced condensation on scalable superhydrophobic nanostructured surfaces. Nano Lett 2013, 13 (1), 179-87.

[71] Lv, C.; Hao, P.; Yao, Z.; Niu, F., Departure of condensation droplets on superhydrophobic surfaces. Langmuir 2015, 31 (8), 2414-20.

[72] Liang, Z.; Keblinski, P., Coalescence-induced jumping of nanoscale droplets on super-hydrophobic surfaces. Applied Physics Letters 2015, 107 (14), 143105.

[73] Sheng, Q.; Sun, J.; Wang, W.; Wang, H. S.; Bailey, C. G., How solid surface free energy determines coalescence-induced nanodroplet jumping: A molecular dynamics investigation. Journal of Applied Physics 2017, 122 (24), 245301.

[74] Gao, S.; Liao, Q.; Liu, W.; Liu, Z., Coalescence-induced jumping of nanodroplets on textured surfaces. The Journal of Physical Chemistry Letters 2018, 9(1), 13-18.

[75] Yan, X.; Zhang, L.; Sett, S.; Feng, L.; Zhao, C.; Huang, Z.; Vahabi, H.; Kota, A. K.; Chen, F.; Miljkovic, N., Droplet jumping: effects of droplet size, surface structure, pinning, and liquid properties. ACS Nano 2019, 13 (2), 1309-1323.

[76] Mukherjee, R.; Berrier, A. S.; Murphy, K. R.; Vieitez, J. R.; Boreyko, J. B., How surface orientation affects jumping-droplet condensation. Joule 2019, 3 (5), 1360-1376.

[77] Perumanath, S.; Borg, M. K.; Sprittles, J. E.; Enright, R., Molecular physics of jumping nanodroplets. Nanoscale 2020, 12 (40), 20631-20637.

[78] Shi, Y.; Tang, G. H.; Shen, L. Y., Study of coalescence-induced droplet jumping during phase-change process in the presence of noncondensable gas. International Journal of Heat and Mass Transfer 2020, 152, 119506.

[79] Zhu, Y.; Tso, C. Y.; Ho, T. C.; Leung, M. K. H.; Yao, S., Coalescence-induced jumping droplets on nanostructured biphilic surfaces with contact electrification effects. ACS Applied Materials & Interfaces 2021, 13 (9), 11470-11479.

[80] Enright, R.; Miljkovic, N.; Sprittles, J.; Nolan, K.; Mitchell, R.; Wang, E. N., How coalescing droplets jump. ACS Nano 2014, 8(10), 10352-10362.

[81] Liu, F.; Ghigliotti, G.; Feng, J. J.; Chen, C.-H., Numerical simulations of self-propelled jumping upon drop coalescence on non-wetting surfaces. Journal of Fluid Mechanics 2014, 752, 39-65.

[82] Lv, C.; Hao, P.; Zhang, X.; He, F., Dewetting transitions of dropwise condensation on nanotexture-enhanced superhydrophobic surfaces. ACS Nano 2015, 9(12), 12311-12319.

[83] Aili, A.; Li, H.; Alhosani, M. H.; Zhang, T., Unidirectional fast growth and forced jumping of stretched droplets on nanostructured microporous surfaces. ACS Applied Materials & Interfaces 2016, 8 (33), 21776-86.

[84] Sharma, C. S.; Combe, J.; Giger, M.; Emmerich, T.; Poulikakos, D., Growth rates and spontaneous navigation of condensate droplets through randomly structured textures. ACS Nano 2017, 11 (2), 1673-1682.

[85] Peng, Q.; Yan, X.; Li, J.; Li, L.; Cha, H.; Ding, Y.; Dang, C.; Jia, L.; Miljkovic, N., Breaking droplet jumping energy conversion limits with superhydrophobic microgrooves. Langmuir 2020, 36 (32), 9510-9522.

[86] Winter, R. L.; McCarthy, M., Dewetting from amphiphilic minichannel surfaces during condensation. ACS Applied Materials & Interfaces 2020, 12 (6), 7815-7825.

[87] Yan, X.; Qin, Y.; Chen, F.; Zhao, G.; Sett, S.; Hoque, M. J.; Rabbi, K. F.; Zhang, X.; Wang, Z.; Li, L.; Chen, F.; Feng, J.; Miljkovic, N., Laplace pressure driven single-droplet jumping on structured surfaces. ACS Nano 2020, 14 (10), 12796-12809.

[88] Plawsky, J.; Fedorov, A.; Garimella, S.; Ma, H.; Maroo, S.; Chen, L.; Nam, Y., Nano-and microstructures for thin-film evaporation—A review. Nanoscale and Microscale Thermophysical Engineering 2014, 18 (3), 251-269.

[89] Edalatpour, M.; Liu, L.; Jacobi, A.; Eid, K.; Sommers, A., Managing water on heat transfer surfaces: A critical review of techniques to modify surface wettability for applications with condensation or evaporation. Applied Energy 2018, 222, 967-992.

[90] Zhu, L.; Gao, M.; Peh, C. K. N.; Ho, G. W., Recent progress in solar-driven interfacial water evaporation: Advanced designs and applications. Nano Energy 2019, 57, 507-518.

[91] Pang, Y.; Zhang, J.; Ma, R.; Qu, Z.; Lee, E.; Luo, T., Solar–thermal water evaporation: a review. ACS Energy Letters 2020, 5 (2), 437-456.

[92] Pu, J. H.; Sun, J.; Wang, W.; Wang, H. S., Generation and evolution of nanobubbles on heated nanoparticles: a molecular dynamics study. Langmuir 2020, 36(9), 2375-2382.

[93] Vaartstra, G.; Zhang, L.; Lu, Z.; Díaz-Marín, C. D.; Grossman, J. C.; Wang, E. N., Capillary-fed, thin film evaporation devices. Journal of Applied Physics 2020, 128 (13), 130901.

[94] Cao, Q.; Cui, Z.; Shao, W., Optimization method for grooved surface structures regarding the evaporation heat transfer of ultrathin liquid films at the nanoscale. Langmuir 2020, 36(11), 2802-2815.

[95] Li, C.; Lan, C.; Guo, M.; Wang, N.; Ma, Y., Wicking-driven evaporation self-assembly of carbon nanotubes on fabrics: generating controlled orientational structures. Langmuir 2020, 36(46), 13963-13970.

[96] Li, R.; Wang, J.; Xia, G., New model for liquid evaporation and vapor transport in nanopores covering the entire Knudsen regime and arbitrary pore length. Langmuir 2021, 37 (6), 2227-2235.

[97] Somasundaram, S.; Zhu, Y.; Lu, Z.; Adera, S.; Bin, H.; Mengyao, W.; Tan, C. S.; Wang, E. N., Thermal design optimization of evaporator micropillar wicks. International Journal of Thermal Sciences 2018, 134, 179-187.

[98] Tang, H.; Tang, Y.; Wan, Z.; Li, J.; Yuan, W.; Lu, L.; Li, Y.; Tang, K., Review of applications and developments of ultra-thin micro heat pipes for electronic cooling. Applied Energy 2018, 223, 383-400.

[99] Zhou, X.; Zhao, F.; Guo, Y.; Zhang, Y.; Yu, G., A hydrogel-based antifouling solar evaporator for highly efficient water desalination. Energy & Environmental Science 2018, 11 (8), 1985-1992.

[100] Zhu, Y.; Antao, D. S.; Lu, Z.; Somasundaram, S.; Zhang, T.; Wang, E. N., Prediction and characterization of dry-out heat flux in micropillar wick structures. Langmuir 2016, 32(7), 1920-1927.

[101] Ranjan, R.; Patel, A.; Garimella, S. V.; Murthy, J. Y., Wicking and thermal characteristics of micropillared structures for use in passive heat spreaders. International Journal of Heat and Mass Transfer 2012, 55 (4), 586-596.

[102] Ravi, S.; Horner, D.; Moghaddam, S., Monoporous micropillar wick structures, I-Mass transport characteristics. Applied thermal engineering 2014, 73 (1), 1371-1377.

[103] Horner, D.; Ravi, S.; Moghaddam, S., Monoporous micropillar wick structures, II-optimization & theoretical limits. Applied thermal engineering 2014, 73 (1), 1378-1386.

[104] Adera, S.; Antao, D.; Raj, R.; Wang, E. N., Design of micropillar wicks for thin-film evaporation. International Journal of Heat and Mass Transfer 2016, 101, 280-294.

[105] Farokhnia, N.; Irajizad, P.; Sajadi, S. M.; Ghasemi, H., Rational micro/nanostructuring for thin-film evaporation. The Journal of Physical Chemistry C 2016, 120(16), 8742-8750.

[106] Ravi, S.; Dharmarajan, R.; Moghaddam, S., Physics of fluid transport in hybrid biporous capillary wicking microstructures. Langmuir 2016, 32(33), 8289-8297.

[107] Antao, D. S.; Adera, S.; Zhu, Y.; Farias, E.; Raj, R.; Wang, E. N., Dynamic evolution of the evaporating liquid-vapor interface in micropillar arrays. Langmuir 2016, 32(2), 519-526.

[108] Lu, Z.; Preston, D. J.; Antao, D. S.; Zhu, Y.; Wang, E. N., Coexistence of pinning and moving on a contact line. Langmuir 2017, 33(36), 8970-8975.

[109] Cho, S.; Tummala, R.; Joshi, Y., Capillary performance of micropillar arrays in different arrangements. Nanoscale and Microscale Thermophysical Engineering 2018, 22(2), 97-113.

[110] Wei, M.; He, B.; Liang, Q.; Somasundaram, S.; Tan, C. S.; Wang, E. N., Optimization and thermal characterization of uniform silicon micropillar based evaporators. International Journal of Heat and Mass Transfer 2018, 127, 51-60.

[111] Zhang, L.; Zhu, Y.; Lu, Z.; Zhao, L.; Bagnall, K. R.; Rao, S. R.; Wang, E. N., Characterization of thin film evaporation in micropillar wicks using micro-Raman spectroscopy. Applied Physics Letters 2018, 113(16), 163701.

[112] Wang, R. S.; Jakhar, K.; Antao, D. S., Unified Modeling Framework for Thin-Film Evaporation from Micropillar Arrays Capturing Local Interfacial Effects. Langmuir 2019, 35 (40), 12927-12935.

[113] Cai, Q. J.; Bhunia, A., High heat flux phase change on porous carbon nanotube structures. International Journal of Heat and Mass Transfer 2012, 55 (21-22), 5544-5551.

[114] Coso, D.; Srinivasan, V.; Lu, M. C.; Chang, J. Y.; Majumdar, A., Enhanced heat transfer in biporous wicks in the thin liquid film evaporation and boiling regimes. Journal of Heat Transfer, 2012, 134 (10), 11.

[115] Cai, S. Q.; Bhunia, A., Characterization of phase change heat and mass transfers in monoporous silicon wick structures. Journal of Heat Transfer 2014, 136 (7), 072001.

[116] Dykman, L.; Khlebtsov, N. Gold nanoparticles in biomedical applications: recent advances and perspectives. Chemical Society Reviews 2012, 41(6), 2256-2282.

[117] Yang, H., Nanoparticle-mediated brain-specific drug delivery, imaging, and diagnosis. Pharmaceutical research 2010, 27 (9), 1759-1771.

[118] Lapotko, D., Plasmonic nanoparticle-generated photothermal bubbles and their biomedical applications. Nanomedicine 2009, 4(7), 813-845.

[119] Jaque, D.; Maestro, L. M.; Rosal, D. B.; Benayas, A.; Plaza, L. J.; Rodriguez, M. E.; Sole, G. J., Nanoparticles for photothermal therapies. Nanoscale 2014, 6(16), 9494-9530.

[120] Shao, J.; Xuan. M.; Dai, L.; Si, T.; Li, J.; He, Q., Near-infrared-activated nanocalorifiers in microcapsules: vapor bubble generation for in vivo enhanced cancer therapy. Angewandte Chemie International Edition 2015, 54(43), 12782-12787.

[121] Du, M.; Tang, G. H.; Wang, T. M., Exergy analysis of a hybrid PV/T system based on plasmonic nanofluids and fit silica aerogel glazing. Solar Energy 2019, 183, 501-511.

[122] Boriskina, S. V.; Ghasemi, H.; Chen, G., Plasmonic materials for energy: From physics to applications. Materials Today 2013, 16 (10), 375-386.

[123] Neumann, O.; Urban, A. S.; Day, J.; Lal, S.; Nordlander, P.; Halas, N. J., Solar vapor generation enabled by nanoparticles. ACS Nano 2013, 7 (1), 42-49.

[124] Du, M.; Tang, G. H., Optical property of nanofluids with particle agglomeration. Solar Energy 2015, 122, 864-872.

[125] Chen, C. J.; Kuang, Y. D.; Hu, L. B., Challenges and opportunities for solar evaporation. Joule 2019, 3 (3), 683-718.

[126] Du, M.; Tang, G. H., Plasmonic nanofluids based on gold nanorods/nanoellipsoids/nanosheets for solar energy harvesting. Solar Energy 2016, 137, 393-400.

[127] Baffou, G.; Quidant, R., Nanoplasmonics for chemistry. Chemical Society Reviews 2014, 43 (11), 3898-3907.

[128] Brongersma, M. L.; Halas, N. J.; Nordlander, P., Plasmon-induced hot carrier science and technology. Nature Nanotechnology 2015, 10 (1), 25-34.

[129] Lukianova-Hleb, E. Y.; Hanna, E. Y.; Hafner, J. H.; Lapotko, D. O., Tunable plasmonic nanobubbles for cell theranostics. Nanotechnology 2010, 21 (8), 10.

[130] Siems, A.; Weber, S. A. L.; Boneberg, J.; Plech, A., Thermodynamics of nanosecond nanobubble formation at laser-excited metal nanoparticles. New Journal of Physics 2011, 13(4), 043018.

[131] Fang, Z. Y.; Zhen, Y. R.; Neumann, O.; Polman, A.; de Abajo, F. J. G.; Nordlander, P.; Halas, N. J., Evolution of light-induced vapor generation at a liquid-immersed metallic nanoparticle. Nano Letters 2013, 13 (4), 1736-1742.

[132] Wang, Y.; Zaytsev, M. E.; The, H. L.; Eijkel, J. C. T.; Zandvliet, H. J. W.; Zhang, X.; Lohse, D. Vapor and gas-bubble growth dynamics around laser-irradiated, water-immersed plasmonic nanoparticles. ACS Nano 2017, 11(2), 2045-2051.

[133] Wang, Y. L.; Zaytsev, M. E.; Lajoinie, G.; The, T. H.; Eijkel, J. C. T.; van den Berg, A.; Versluis, M.; Weckhuysen, B. M.; Zhang, X. H.; Zandvliet, H. J. W.; Lohse, D., Giant and explosive plasmonic bubbles by delayed nucleation. Proceedings of the National Academy of Sciences of the United States of America 2018, 115 (30), 7676-7681.

[134] Lukianova-Hleb, E.; Hu, Y.; Latterini, L.; Tarpani, L.; Lee, S.; Drezek, R. A.; Hafner, J. H.; Lapotko, D. O., Plasmonic nanobubbles as transient vapor nanobubbles generated around plasmonic nanoparticles. ACS Nano 2010, 4 (4), 2109-2123.

[135] Li, X. L.; Wang, Y. L.; Zaytsev, M. E.; Lajoinie, G.; The, H. L.; Bomer, J. G.; Eijkel, J. C. T.; Zandvliet, H. J. W.; Zhang, X. H.; Lohse, D., Plasmonic bubble nucleation and growth in water: effect of dissolved air. Journal of Physical Chemistry C 2019, 123 (38), 23586-23593.

[136] Merabia, S.; Keblinski, P.; Joly, L.; Lewis, L. J.; Barrat, J. L., Critical heat flux around strongly heated nanoparticles. Physical Review E 2009, 79 (2), 021404.

[137] Sasikumar, K.; Liang, Z.; Cahill, D. G.; Keblinski, P., Curvature induced phase stability of an intensely heated liquid. Journal of Chemical Physics 2014, 140 (23), 234506.

[138] Sasikumar, K.; Keblinski, P., Molecular dynamics investigation of nanoscale cavitation dynamics. Journal of Chemical Physics 2014, 141 (23), 234508.

[139] Maheshwari, S.; van der Hoef, M.; Prosperetti, A.; Lohse, D., Dynamics of formation of a vapor nanobubble around a heated nanoparticle. Journal of Physical Chemistry C 2018, 122 (36), 20571-20580.

[140] Alder, B. J.; Wainwright, T. E., Phase transition for a hard sphere system. The Journal of chemical physics 1957, 27 (5), 1208-1209.

[141] Plimpton, S.; Fast parallel algorithms for short-range molecular dynamics. Journal of computational physics 1995, 117(1), 1-19.

[142] Xu, D.; Li, D., Molecular Dynamics Simulation Method. Encyclopedia of Microfluidics and Nanofluidics 2008, 1391-1398.

[143] Rapaport, D. C., The art of molecular dynamics simulation. Cambridge University Press, 2004.

[144] Binder, K., Monte Carlo and molecular dynamics simulations in polymer science. Oxford University Press, 1995.

[145] Jones, J. E., On the determination of molecular fields.—II. From the equation of state of a gas. Proceedings of the Royal Society of London. Series A, Containing Papers of a Mathematical and Physical Character 1924, 106 (738), 463-477.

[146] Daw, M. S.; Baskes, M. I., Semiempirical, quantum mechanical calculation of hydrogen embrittlement in metals. Physical Review Letters 1983, 50 (17), 1285.

[147] Berendsen, H. J.; Postma, J. v.; van Gunsteren, W. F.; DiNola, A.; Haak, J. R., Molecular dynamics with coupling to an external bath. The Journal of Chemical Physics 1984, 81 (8), 3684-3690.

[148] Sam, A.; Kannam, S. K.; Hartkamp, R.; Sathian, S. P., Water flow in carbon nanotubes: The effect of tube flexibility and thermostat. The Journal of Chemical Physics 2017, 146 (23), 234701.

[149] Hess B., Stochastic concepts in molecular simulation, PhD thesis, University of Groningen, 2002.

[150] Jaeger F., Molecular modelling and simulation of fluid flow under confinement at the nanoscale, Imperial College of London, 2018.

[151] Stillinger Jr., F. H. Rigorous basis of the Frenkel-Band theory of association equilibrium. The Journal of Chemical Physics 1963, 38(7), 1486-1494.

[152] Yasuoka, K.; Matsumoto, M., Molecular dynamics of homogeneous nucleation in the vapor phase. I. Lennard-Jones fluid. The Journal of Chemical Physics 1998, 109(19), 8451-8462.

[153] Rozas, R.; Kraska, T., Molecular dynamics simulation of heterogeneous nucleation and growth of argon at polyethylene films. The Journal of Physical Chemistry C 2007, 111(43), 15784-15791.

[154] Wang, H., From contact line structures to wetting dynamics. Langmuir 2019, 35(32), 10233-10245.

[155] Shi, B.; Dhir, V. K., Molecular dynamics simulation of the contact angle of liquids on solid surfaces. The Journal of Chemical Physics 2009, 130(3), 034705.

[156] Tang, G.; Niu, D.; Guo, L.; Xu, J., Failure and recovery of droplet nucleation and growth on damaged nanostructures: A Molecular Dynamics study. Langmuir 2020, 36 (45), 13716-13724.

[157] Pu, J. H.; Sun, J.; Sheng, Q.; Wang, W.; Wang, H. S., Dependences of formation and transition of the surface condensation mode on wettability and temperature difference. Langmuir 2020, 36 (1), 456-464.

[158] Antao, D. S.; Adera, S.; Zhu, Y. Y.; Farias, E.; Raj, R.; Wang, E. N., Dynamic evolution of the evaporating liquid vapor interface in micropillar arrays. Langmuir 2016, 32 (2), 519-526.

[159] Stukowski, A., Visualization and analysis of atomistic simulation data with OVITO-the Open Visualization Tool. Modelling and Simulation in Materials Science and Engineering 2010, 18 (1), 015012.

[160] Akkus, Y.; Koklu, A.; Beskok, A., Atomic scale interfacial transport at an extended evaporating meniscus. Langmuir 2019, 35(13), 4491-4497.

[161] Chen, Y.; Li, J.; Yu, B.; Sun, D.; Zou, Y.; Han, D., Nanoscale study of bubble nucleation on a cavity substrate using molecular dynamics simulation. Langmuir 2018, 34(47), 14234-14248.

[162] Chen, Y. J.; Chen, X. J.; Yu, B.; Zou, Y.; Tao, W. Q., Molecular dynamics study of bubble nucleation on an ideally smooth substrate. Langmuir 2020, 36(45), 13725-13734.

[163] Chen, Y. J.; Yu, B.; Zou, Y.; Chen, B. N.; Tao, W. Q., Molecular dynamics studies of bubble nucleation on a grooved substrate. International Journal of Heat and Mass Transfer 2020, 158, 119850.

[164] Yu, J. P.; Wang, H., A molecular dynamics investigation on evaporation of thin liquid films. International Journal of Heat and Mass Transfer 2012, 55 (4), 1218-1225.

[165] Wang, X. M.; Li, Y.; Malen, J. A.; McGaughey, A. J. H., Assessing the impact of disjoining pressure on thin-film evaporation with atomistic simulation and kinetic theory. Applied Physics Letters 2020, 116 (21), 213701.

[166] Wang, H.; Garimella, S. V.; Murthy, J. Y., Characteristics of an evaporating thin film in a microchannel. International Journal of Heat and Mass Transfer 2007, 50 (19-20), 3933-3942.

[167] Allen, M. P.; Tildesley, D. J., Computer simulation of liquids. Oxford University Press, 2017.

[168] Plech, A.; Kotaidis, V.; Gresillon, S.; Dahmen, C.; von Plessen, G., Laser-induced heating and melting of gold nanoparticles studied by time-resolved x-ray scattering. Physical Review B 2004, 70 (19), 195423.

[169] Buffat, P.; Borel, J. P. Size effect on the melting temperature of gold particles. Physical Review A 1976, 13(6), 2287.

[170] Lee, J.; Lee, J.; Tanaka, T.; Mori, H., In situ atomic-scale observation of melting point suppression in nanometer-sized gold particles. Nanotechnology 2009, 20 (47), 475706.

[171] Kart, H. H.; Yildirim, H.; Kart, S. O.; Cagin, T., Physical properties of Cu nanoparticles: A molecular dynamics study. Materials Chemistry and Physics 2014, 147 (1-2), 204-212.

[172] Zhang, J. C.; Wang, X. Y.; Zhu, Y. Y.; Shi, T. L.; Tang, Z. R.; Li, M.; Liao, G. L., Molecular dynamics simulation of the melting behavior of copper nanorod. Computational Materials Science 2018, 143, 248-254.

[173] Gerasimov, V. S.; Ershov, A. E.; Gavrilyuk, A. P.; Karpov, S. V.; Agren, H.; Polyutov, S. P., Suppression of surface plasmon resonance in Au nanoparticles upon transition to the liquid state. Optics Express 2016, 24 (23), 26851-26856.

[174] Gerasimov, V. S.; Ershov, A. E.; Karpov, S. V.; Gavrilyuk, A. P.; Zakomirnyi, V. I.; Rasskazov, I. L.; Aring;gren, H.; Polyutov, S. P., Thermal effects in systems of colloidal plasmonic nanoparticles in high-intensity pulsed laser fields Invited. Opt. Mater. Express 2017, 7 (2), 555-568.

[175] Wang, S. Q.; Fu, L.; Zhang, Y.; Wang, J.; Zhang, Z. X., Quantitative evaluation and optimization of photothermal bubble generation around overheated nanoparticles excited by pulsed lasers. Journal of Physical Chemistry C 2018, 122 (42), 24421-24435.

[176] Cui, J. L.; Yang, L. J.; Wang, Y., Molecular dynamics simulation study of the melting of silver nanoparticles. Integrated Ferroelectrics 2013, 145 (1), 1-9.